Active Colloids and Polymer Translocation

Jack Andrew Cohen
St Cross College

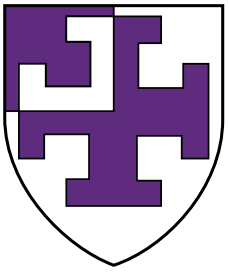

Doctor of Philosophy in Theoretical Physics

Hilary 2013

Active Colloids and Polymer Translocation

Jack Andrew Cohen, St Cross College

Doctor of Philosophy in Theoretical Physics

Hillary 2013

Abstract

This thesis considers two areas of research in non-equilibrium soft matter at the mesoscale.

In the first part we introduce active colloids in the context of active matter and focus on the particular case of phoretic colloids. The general theory of phoresis is presented along with an expression for the phoretic velocity of a colloid and its rotational diffusion in two and three dimensions. We introduce a model for thermally active colloids that absorb light and emit heat and propel through thermophoresis. Using this model we develop the equations of motion for their collective dynamics and consider excluded volume through a lattice gas formalism. Solutions to the thermoattractive collective dynamics are studied in one dimension analytically and numerically. A few numerical results are presented for the collective dynamics in two dimensions. We simulate an unconfined system of thermally active colloids under directed illumination with simple projection based geometric optics. This system self-organises into a comet-like swarm and exhibits a wide range of non-equilibrium phenomena.

In the second part we review the background of polymer translocation, including key experiments, theoretical progress and simulation studies. We present, discuss and use a common model to investigate the potential of patterned nanopores for stochastic sensing and identification of polynucleotides and other heteropolymers. Three pore patterns are characterised in terms of the response of a homopolymer with varying attractive affinity. This is extended to simple periodic block co-polymer heterostructures and a model device is proposed and demonstrated with two stochastic sensing algorithms. We find that multiple sequential measurements of the translocation time is sufficient for identification with high accuracy. Motivated by fluctuating biological channels and the prospect of frequency based selectivity we investigate the response of a homopolymer through a pore that has a time dependent geometry. We show that a time dependent mobility can capture many features of the frequency response.

Acknowledgements

Ramin Golestanian has played an integral role in the development of this work. I feel privileged to have had the pleasure of working with and learning from him for many years and hope we can continue to play a part together in the emerging and exciting field of active matter. Much of the work in polymer translocation developed from the enthusiasm and interest of Abhishek Chaudhuri and I value him as a collaborator and a good friend. I am very grateful to Edward Daw who gave me the kind of early stage encouragement that can shape someones outlook and helped me to pursue my interests. Finally, I would like to thank Elizabeth Read not only for proof reading much of my writing but for being a continual source of support and happiness.

None of this work would have been possible without the funding received from the EPSRC, and for this I am very grateful. The Rudolf Peierls Centre for Theoretical Physics and St Cross college have provided funding for travel and I would like to thank them for this and for accommodating me during my studies.

Contents

Part I

Active Colloids

Chapter 1

Introduction

1.1 Active matter and collective dynamics

Active matter consists of *active particles* that convert energy into work [1]. These active particles can be biological entities, such as molecular motors, bacteria, cells, fish, birds or people, or they could be artificial, such as vibrated grains, robots, simulated agents or *active colloids*.

Regardless of the form they take these active particles use stored or surrounding free energy to perform work on their surroundings, usually resulting in self-propulsion. When a collection of active particles arises its combined action can produce stress on the environment. In the case of fluid dwellers, this can produce turbulent flow patterns driven at short length scales with unusual non-equilibrium statistics [2]. In many cases highly correlated collective dynamic motion emerges, as is commonly observed in the form of flocks, herds and swarms. With the notable exception of vibrated granular matter [3], there are very few examples for the collective dynamics of artificial systems. Active colloids are an attractive candidate for artificial collective dynamics due to their convenient mesoscopic

size and the wide range of colloid synthesis techniques available to tune their interactions with each other and the fluid.

A set of common traits existing over many scales naturally suggests to physicists a 'universal' description and perhaps a generic set of laws. On first sight this seems highly unconventional as it breaks from the traditional domain of physics into all of living matter. However, many theoretical techniques from condensed matter, such as the construction of field equations from symmetry arguments and the statistical mechanics of many body systems, are proving highly successful [1, 4, 5]. Indeed, many theorems formed from equilibrium condensed matter no longer apply and drawing analogies to equilibrium matter highlights the unusual features, such as true long range order [6] and strange sound or information propagation [7]. It is clear that the study of active matter has much to offer condensed matter theory, which in turn, has much to offer biology through a systematic understanding and categorisation of the features of these systems.

With the motivation for the study of active matter briefly outlined, we will now focus on the specific case of active colloids by looking at some of the self-propulsion mechanisms and interesting collective behaviours. We will then move on to the theory of phoresis and self-phoresis, which provides a propulsion mechanism for active colloids, and present some results that will be used in the following chapters.

1.2 Active colloids

In general, *colloids* are particles of one medium dispersed in another medium that range from micrometre to nanometre in size. Here we will exclusively consider solid colloids

dispersed in liquid. The surface area to volume ratio becomes large on reduction to these scales and as a result surface chemistry plays an increasingly important role. The colloids become active when they consume energy from the environment through surface catalysis of a solute or the solution, or through the absorption of electromagnetic fields. It is well known that colloids can move in response to gradients in concentration, electric and temperature fields in a process known as *phoresis*, with *diffusio*phoresis, *electro*phoresis and *thermo*phoresis observed for the previously mentioned fields. By tailoring the surface activity these fields can be produced natively, generating self-propulsion through self-phoresis. The theory of phoresis will be described in more detail in the following chapter, for this introduction it is sufficient to understand that it can act as a driving force for motion.

Controlled propulsion at this scale presents several difficulties that arise from the intrinsic physics. The viscous drag force far outweighs the inertial force at the microscale, as characterised by a low Reynolds number. Any swimming strategy that involves body deformations cannot use the force of inertia and instead must pull or push the swimmer through the fluid in a non-reciprocal way to achieve net translation as described by the scallop theorem [8].

Maintaining a supply of energy at the level of an individual object is a challenge for synthetic active matter. Biological organisms use the chemical energy stored in ATP to power sophisticated molecular motors, such as the ATP synthase used to drive the corkscrew-like flagella in E. *coli* [9]. Rather than borrow this complex machinery active colloids use phoresis powered by chemical or electromagnetic energy to induce fluid flow at the colloid surface, escaping the need for moving parts or body deformation.

Although the fluid appears highly viscous, the movement of a body is incessant due to Brownian motion driven by thermal energy. This becomes increasingly troublesome for controlled motion of small bodies as the diffusion coefficient scales as $\propto 1/r$ where r is the radius of the particle.

Having the ability of controlled motion on this scale could allow for self-assembly driven by non-equilibrium interactions, chemical sensors or processors that can disperse quickly in a medium, targeted delivery of chemical compounds and perhaps even dynamic micro-machinery.

1.2.1 Self-propulsion

Several mechanisms have been demonstrated in order to achieve propulsion using surface catalysis. The first demonstration by Whitesides *et al.* (2002) used centimetre-sized discs sitting at the surface of a fluid of hydrogen peroxide (H_2O_2) with a platinum (Pt) coated 'rudder' that generated oxygen bubbles though the reaction $2H_2O_2 \rightarrow O_2 + 2H_2O$ [10].

This was taken to the microscale by Paxton *et al.* (2004) with half gold and half platinum ($\mathrm{Au}-\mathrm{Pt}$) rods of $1\,\mu$m length propelling at $10\,\mu\mathrm{ms}^{-1}$ [11] . In this case the motion of the rod arises not from bubble production, but from self-electrophoretic interfacial transport of the fluid driven by a redox reaction and a current through the rod [12, 13].

Soon after, it was independently proposed by Golestanian *et al.* (2005) that colloidal particles could self-propel due to an asymmetric distribution of reaction products in another interfacial transport effect known as self-diffusiophoresis [14, 15]. This was later demonstrated by Howse *et al.* (2007) with $\sim 1.6\,\mu$m sized polystyrene spheres half coated in

platinum (PS−Pt), dubbed Janus particles [16], propelling at speeds of $\sim 3\,\mu\text{ms}^{-1}$. These catalytic colloids are non-conductive in contrast to bi-metallic propellers such as the rod mentioned above. The Janus particles were also seen to self assemble into doublets and, depending on the relative angle between the orientations, would show rotational as well as translational motion [17].

The self-propellers mentioned previously achieved their motion through chemical activity at the surface. Another type of active colloid propels through thermal activity at the surface due to the asymmetric absorption of light. The absorbed electromagnetic energy generates an asymmetric temperature field around the colloid giving rise to interfacial flow through thermophoresis. Sano *et al.* (2010) demonstrated that Silica colloids half coated in Gold (Si−Au) illuminated by a defocused laser show motion to regions of colder (hotter) temperature with positive (negative) Soret coefficient [18]. The temperature distribution and subsequently the velocity of the colloid is proportional to the laser power with $1\,\mu$m colloids propelling at $\sim 1\,\mu\text{ms}^{-1}$ at a laser power of 10 mW. A negative Soret coefficient is observed on addition of the surfactant Triton X-100, which absorb on the colloid surface and modify the interfacial properties. Chicos and Yang *et al.* (2013) have shown that the motion of these thermally active colloids can be directed by using real-time particle tracking and illuminating the colloid only when facing in a target direction [19].

1.2.2 Collective behaviour

A collection of many phoretic colloids interact with each other through long range chemical or thermal phoretic fields and short range steric repulsion or surface potentials. Their

motion is directed along gradients of these fields generated by the collective surface activity. This type of interaction is in some ways analogous to the behaviour of microscopic organisms towards pheromones or away from toxins, known as chemotaxis. It has therefore been proposed that active colloids can act as an artificial chemotactic system. Understanding this dynamic aggregation phenomena could lead to cooperative synthetic systems functioning on the microscale and show 'swarming' behaviour outside of living matter.

Sen *et al.* (2009) reported schooling behaviour of silver chloride (AgCl) particles under UV illumination in water [20]. These colloids are reported to move at speeds of up to $100\,\mu\mathrm{ms}^{-1}$ driven by a photochemical surface reaction that plates the colloid in silver and generates diffusiophoresis through the product solutes. The asymmetry required for propulsion is attributed to surface imperfections or non-uniform illumination. As with all other experiments presented in this section, the colloids are left to sediment onto a slide or chamber but remain separated from the surface by a few micrometres due to electrostatic repulsion. Under illumination the particles were found to arrange into multiple high density clusters but with a finite spacing between the colloids due to zeta potential repulsion.

Sen *et al.* (2010) discovered a wide range of collective behaviour by replacing water in the previous system with H_2O_2 and adding a second population of Silicon (Si) tracer particles [21]. Two chemical reactions at the surface of the AgCl colloid would now compete to give rise to oscillatory motion, one photochemical reaction plating the colloid and another reaction with H_2O_2 reversing this. The solutes produced in the oscillating reaction cause the Si tracers to switch between negative and positive diffusiophoresis towards the AgCl

particles. Propagation of reaction fronts and interesting explosion events were observed in dense suspensions. This is an interesting example of coupling spatial and temporal chemical reactions with dynamic motion.

In contrast to the AgCl particles that degrade under exposure, Wang *et al.* (2011) showed 'swarming' of gold (Au) microparticles on the addition of hydrazine to a H_2O_2 solution. These micron sized colloids moved at speeds of $16\,\mu\mathrm{ms}^{-1}$ and formed tightly packed clusters. These clusters were reported to continuously draw in more colloids to form larger schools.

Palacci *et al.* (2010) studied motility and pattern formation [22]. Later, Palacci *et al.* (2010) characterised the steady state density profile of sedimenting active colloids using an effective temperature [23]. They presented a dynamically clustering system of micron sized gold and platinum (Au-Pt) conductive Janus colloids in H_2O_2. Unlike the findings of Wang *et al.* (2011) these clusters formed a dynamic finite size, with colloids joining and leaving a tightly packed hexagonal crystal structure. The average size of these clusters was shown to depend linearly on the phoretic activity of the colloids.

Palacci and Sacanna *et al.* (2013) investigated these so called 'living crystals' further with an ingeniously formed bimaterial colloid composed of an active hematite cube embedded within a polymer sphere in a multicomponent solution containing, in part, H_2O_2 and surfactants [24]. The hematite patch catalyses the exothermic decomposition of H_2O_2 generating thermal and chemical fields leading to phoretic motion, however this movement was only observed near the slide surface. Reversible formation of dynamic crystals of finite average size was demonstrated on repeated exposure to blue light with characteristic non-equilibrium giant number fluctuations observed for the clusters. Hematite has a weak

magnetic dipole and so the colloids could be controlled with external magnetic fields. As phoretic colloids are non-advecting they do not adhere to the zero divergence condition on the velocity field. This was nicely demonstrated by the convergence of Si tracer particles onto a fixed hematite cube from all directions.

Chapter 2

Phoresis

2.1 Introduction

Small particles suspended in a fluid can be set into motion by a spatially varying concentration, electric potential or temperature field, $\Phi(\mathbf{r})$, surrounding the particle. This is known as phoresis with diffusiophoresis, electrophoresis and thermophoresis observed for the previously mentioned fields.

In general, this motion is due to interactions between the field, fluid and colloid, which generates flow at the surface. This can be best explained by conceptually introducing an interfacial region between the fluid and the colloid surface set by the length scale of the surface interactions. This interface serves to decouple the small-scale surface physics and the larger-scale hydrodynamics relative to the colloid size and is know as the boundary layer approximation.

The flow generated within this region can be captured by an effective slip velocity, $\mathbf{v}_s$, at the outer boundary between the interface and fluid, R_+. The fluid is governed by Stokes

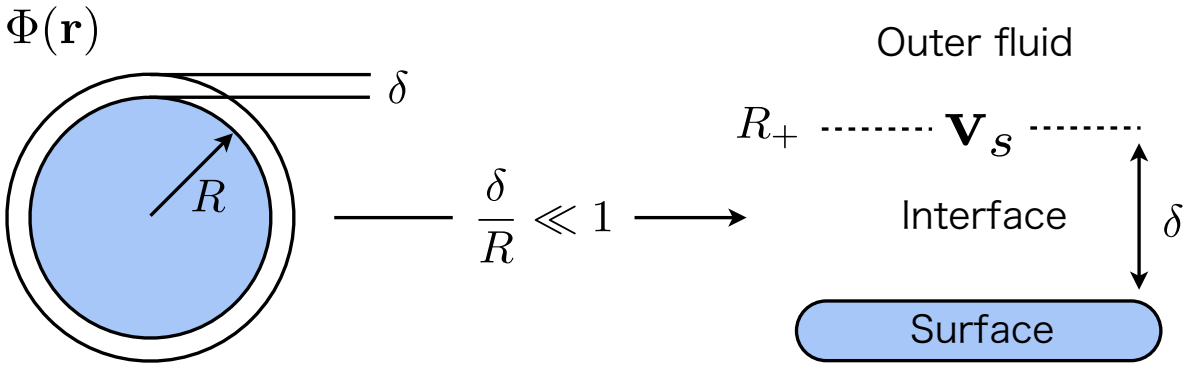

FIGURE 2.1: A schematic diagram of the phoretic interface. A phoretic field $\Phi(\mathbf{r})$ surrounds a particle of radius R. The surface interactions have a characteristic scale δ which is much smaller than R. The interactions of the field, fluid and surface considered within this interface generate a slip velocity $\mathbf{v}_s$ at the outer boundary R_+. This velocity is used as a boundary condition for the hydrodynamics of the outer fluid.

equations outside the interface with a boundary condition set by the slip velocity at the interface, see Figure 2.1.

An important aspect of phoresis is that the external field applies no net force or torque to the combined colloid and interfacial region. This important force-free condition results in rapidly decaying $1/r^3$ hydrodynamic flow around the colloid and permits us to neglect the hydrodynamic interactions between particles in dilute suspensions [25].

2.2 Theory

2.2.1 General

We will consider the general theory of phoresis for hard spherical particles irrespective of the specific surface phenomena. We assume a form for the slip velocity that is proportional to the gradient of the field, $\mathbf{v}_s \propto \nabla\Phi$. Using spherical coordinates (r, θ, ϕ), with the origin

at the colloid centre, the surface slip velocity at $r = R_+$ is

$$\mathbf{v}_s(\theta, \phi) = \mu_p(\theta, \phi)\nabla_s\Phi(\theta, \phi) \tag{2.1}$$

where μ_p is the phoretic mobility. This form is valid for many phoretic effects that can be considered within the boundary layer approximation and the assumptions outlined above [25]. The mobilities scale inversely with solvent viscosity and for electrophoresis it is dependent on the surface zeta potential, for diffusiophoresis on the thermal energy and the first moment of the interaction potential, for thermophoresis the mobility scales inversely with temperature and is related to the free enthalpy, however, the molecular origins of thermophoresis are still largely unknown and it is thought to be due to a combination of interfacial effects [26, 27]. The phoretic mobility can be position dependent [15] but in what follows we will assume this to be constant, $\mu_p(\theta, \phi) = \mu_p$. In the above we have used the surface gradient $\nabla_s = (\mathbb{1} - \hat{\mathbf{r}} \otimes \hat{\mathbf{r}}) \cdot \nabla$, which in spherical coordinates is

$$\nabla_s = \frac{1}{r}\frac{\partial}{\partial\theta}\hat{\theta} + \frac{1}{r\sin\theta}\frac{\partial}{\partial\phi}\hat{\phi} \tag{2.2}$$

The flow outside of the interfacial layer is governed by the Stokes equations

$$\nabla p = \eta\nabla^2\mathbf{v}, \quad \nabla \cdot \mathbf{v} = 0 \tag{2.3}$$

with boundary conditions $\mathbf{v}(\theta, \phi) = \mathbf{U} + \boldsymbol{\Omega} \times \mathbf{r} + \mathbf{v}_s(\theta, \phi)$ on the interface at R_+, where $\mathbf{U}$ and $\boldsymbol{\Omega}$ are the net translational velocity and angular velocity of the colloid, and $\mathbf{v}(r \to \infty) \to 0$ at the outer boundary. Due to the force- and torque-free conditions we have the

extra constraints

$$\iint_{R_+} \hat{\mathbf{n}} \cdot \sigma \, dA = 0 \quad , \quad \iint_{R_+} \mathbf{r} \times (\sigma \cdot \hat{\mathbf{n}}) \, dA = 0 \tag{2.4}$$

where σ is the fluid stress tensor.

It can be shown that the net velocity and torque are related to the surface average of the slip velocity [28]

$$\mathbf{U} = -\langle \mathbf{v}_s \rangle \tag{2.5}$$

$$\mathbf{\Omega} = \frac{3}{2a} \langle \mathbf{v}_s \times \hat{\mathbf{n}} \rangle \tag{2.6}$$

where the angled brackets indicate

$$\langle ... \rangle = \frac{1}{A} \iint (...) \, dA \tag{2.7}$$

$$= \frac{1}{4\pi} \int_0^{2\pi} d\phi \int_0^{\pi} \sin\theta d\theta \, (...) \tag{2.8}$$

Equations (2.1) and (2.5) show that in order to calculate the phoretic motion of the colloid all that needs to be known is the spatially varying field, $\Phi(\theta, \phi)$, at the interface. The presence of the colloid can affect the surrounding phoretic fields and may need to be taken into account when calculating Φ.

2.2.2 Phoretic velocity

The phoretic fields could be generated locally by the colloid due to catalytic surface activity. This can produce autonomous motion provided there is sufficient asymmetry

such that the surface average of the slip velocity is non-zero. This is a particularly interesting feature of phoresis, which makes it an attractive candidate for the study of artificial active matter.

The basic theory of phoresis has been extended to general surface dissipative phenomena within the framework of non-equilibrium thermodynamics [29]. Other studies have considered aspects such as efficiency [30] and the role of confinement [31] for diffusiophoretic swimmers and the effect of salt on electrocatalytic [32] and charged thermophoretic [33] self-propellers.

It is useful to perform a spherical harmonic expansion of the phoretic field at the surface, $\Phi(\theta, \phi)$, in order to obtain the phoretic colloid velocity as a function of the expansion coefficients. We will proceed by outlining the details of this calculation, making use of the final result in the following chapters.

We expand the phoretic field at the surface as [34]

$$\Phi(\theta, \phi) = \sum_{l,m} S_{l,m} Y_{l,m}(\theta, \phi) \tag{2.9}$$

where we use the shorthand $\sum_{l,m} = \sum_{l=0}^{\infty} \sum_{m=-l}^{l}$ for the summation and the normalised form of the spherical harmonics

$$Y_{l,m}(\theta, \phi) = \sqrt{\frac{2l+1}{4\pi} \frac{(l-m)!}{(l+m)!}} P_{l,m}(\theta, \phi) e^{im\phi} \tag{2.10}$$

so that

$$\iint Y_{l,m} Y^*_{l',m'} d\Omega = \delta_{l,l'} \delta_{m,m'} \tag{2.11}$$

and $P_{l,m}(\theta, \phi)$ are the associated Legendre polynomials of degree l and order m.

We wish to calculate the phoretic velocity of the colloid

$$\mathbf{U} = -\frac{\mu_p}{4\pi} \iint \nabla_s \Phi(\theta, \phi)\, d\Omega \tag{2.12}$$

where $d\Omega = \sin\theta d\theta d\phi$ is the solid angle and the implied integration ranges are $0 < \theta < \pi$ and $0 < \phi < 2\pi$. The crux of this calculation amounts to evaluating the integral

$$\iint \nabla_s Y_{l,m}(\theta, \phi)\, d\Omega \tag{2.13}$$

which comes from the expansion of Φ. Using the shorthand $Y_{l,m} = Y_{l,m}(\theta, \phi)$ and the expression for the surface gradient the integrand becomes

$$\frac{1}{R}\left[\frac{\partial Y_{l,m}}{\partial \theta}\ \hat{\theta} + \frac{1}{\sin\theta}\frac{\partial Y_{l,m}}{\partial \phi}\ \hat{\phi}\right] \tag{2.14}$$

As we wish to know the velocity in Cartesian coordinates, for convenient use in simulations, we use the expressions for the spherical unit vectors

$$\hat{\theta} = \cos\theta\cos\phi\hat{\mathbf{x}} + \cos\theta\sin\phi\hat{\mathbf{y}} - \sin\theta\hat{\mathbf{z}} \tag{2.15}$$

$$\hat{\phi} = -\sin\phi\hat{\mathbf{x}} + \cos\phi\hat{\mathbf{y}} \tag{2.16}$$

to give

$$\begin{aligned} & \left(\frac{1}{R}\left[\cos\theta\cos\phi\frac{\partial Y_{l,m}}{\partial\theta} - \frac{\sin\phi}{\sin\theta}\frac{\partial Y_{l,m}}{\partial\phi}\right]\right)\hat{\mathbf{x}} \\ + & \left(\frac{1}{R}\left[\cos\theta\sin\phi\frac{\partial Y_{l,m}}{\partial\theta} + \frac{\cos\phi}{\sin\theta}\frac{\partial Y_{l,m}}{\partial\phi}\right]\right)\hat{\mathbf{y}} \\ - & \left(\frac{1}{R}\left[\sin\theta\frac{\partial Y_{l,m}}{\partial\theta}\right]\right)\hat{\mathbf{z}} \end{aligned} \tag{2.17}$$

The integrand in this form contains derivatives of the spherical harmonics $Y_{l,m}$, which yield cumbersome recurrence expressions if evaluated. Instead, we can use integration by parts to remove the derivatives on $Y_{l,m}$. After making use of some trigonometric identities we find

$$\iint \nabla_s Y_{l,m}(\theta,\phi)\,d\Omega = \frac{1}{R}\left[2\iint \sin\theta\cos\phi\,Y_{l,m}\,d\Omega\right]\hat{\mathbf{x}} \tag{2.18}$$

$$+ \frac{1}{R}\left[2\iint \sin\theta\sin\phi\,Y_{l,m}\,d\Omega\right]\hat{\mathbf{y}} \tag{2.19}$$

$$+ \frac{1}{R}\left[2\iint \cos\theta\,Y_{l,m}\,d\Omega\right]\hat{\mathbf{z}} \tag{2.20}$$

We can rewrite the trigonometric products in terms of the first few spherical harmonics by using de Moivre's formula to expand the functions in ϕ as

$$\cos\phi = \frac{e^{i\phi}+e^{-i\phi}}{2}, \quad \sin\phi = \frac{e^{i\phi}-e^{-i\phi}}{2i} \tag{2.21}$$

and

$$Y_{1,0} = \sqrt{\frac{3}{4\pi}}\cos\theta \tag{2.22}$$

$$Y_{1,1} = -\sqrt{\frac{3}{8\pi}}\sin\theta e^{i\phi}, \quad Y_{1,-1} = \sqrt{\frac{3}{8\pi}}\sin\theta e^{i\phi} \tag{2.23}$$

With $Y_{l,m} = (-1)^m Y^*_{l,m}$ we can evaluate the resulting integral of spherical harmonic products using the normalisation in (2.11). We find the following expression for the integral

$$\iint \nabla_s Y_{l,m}(\theta,\phi)\, d\Omega = \frac{2}{R}\left[\sqrt{\frac{8\pi}{3}}\delta_{l,1}\left(\delta_{m,-1}-\delta_{m,1}\right)\right]\hat{\mathbf{x}} \tag{2.24}$$

$$+ \frac{2}{R}\left[\frac{1}{i}\sqrt{\frac{8\pi}{3}}\delta_{l,1}\left(\delta_{m,-1}+\delta_{m,1}\right)\right]\hat{\mathbf{y}} \tag{2.25}$$

$$+ \frac{2}{R}\left[\sqrt{\frac{4\pi}{3}}\delta_{l,1}\delta_{m,0}\right]\hat{\mathbf{z}} \tag{2.26}$$

This can now be used to calculate the colloid velocity. When doing so, the delta functions select the relevant expansion coefficients through the summation over l and m to give the final result

$$\mathbf{U} = \frac{\mu_p}{R}\frac{1}{\sqrt{3\pi}}\left[\sqrt{2}(\mathrm{Re}\left\{S_{1,1}\right\}\hat{\mathbf{x}} - \mathrm{Im}\left\{S_{1,1}\right\}\hat{\mathbf{y}}) - S_{1,0}\hat{\mathbf{z}}\right] \tag{2.27}$$

2.3 Self-phoresis

Self-propelled colloids are of great interest as they can serve as the active particles described in the introduction. This can be achieved through the phoretic mechanism if the phoretic field Φ is generated locally to the particle. The particular case of self-thermophoresis will be developed in the following chapter.

2.3.1 Orientational diffusion

Assuming a steady, locally generated phoretic field, any spherical asymmetry will select a propulsion direction $\hat{\mathbf{n}}$ with velocity v_0. As this orientation experiences rotational diffusion we can write the overdamped Langevin equations for the particle position $\mathbf{r}$ and director $\hat{\mathbf{n}}$

$$\frac{d\mathbf{r}(\mathbf{t})}{dt} = v_o\hat{\mathbf{n}}(t) + \sqrt{2D_0}\boldsymbol{\xi}(t) \tag{2.28}$$

$$\frac{d\hat{\mathbf{n}}(t)}{dt} = \sqrt{2D_r}\boldsymbol{\eta}(t) \times \hat{\mathbf{n}} \tag{2.29}$$

Both noise terms are zero mean and delta correlated in time and have no correlation between components or coupling between rotation and translation

$$\langle \xi_i(t) \rangle = 0, \qquad \langle \xi_i(t)\xi_j(t') \rangle = \delta_{i,j}\delta(t-t') \tag{2.30}$$

$$\langle \eta_i(t) \rangle = 0, \qquad \langle \eta_i(t)\eta_j(t') \rangle = \delta_{i,j}\delta(t-t') \tag{2.31}$$

Spherical particles with radius a and diameter σ have translational, D_0, and rotational, D_r, diffusion coefficients given by

$$D_0 = k_bT/(6\pi\eta a), \quad D_r = k_bT/(8\pi\eta a^3), \quad D/D_r = \frac{4a^2}{3} = \frac{\sigma^2}{3} \tag{2.32}$$

We can find the diffusive properties of the particle by calculating the mean squared displacement (MSD) $\Delta L^2 = \langle (\mathbf{r}(t) - \mathbf{r}(0))^2 \rangle$ where $\mathbf{r}(t) - \mathbf{r}(0) = \int_0^t v_o\hat{\mathbf{n}}(t')dt' + \int_0^t \xi(t')dt'$

such that

$$\begin{aligned}\Delta L^2 &= v_0^2 \int_0^t dt' \int_0^t dt'' \langle \hat{\mathbf{n}}(t') \cdot \hat{\mathbf{n}}(t'') \rangle \\ &+ 2\sqrt{2D_0} \int_0^t dt' \int_0^t dt'' \langle \hat{\mathbf{n}}(t') \cdot \xi(t'') \rangle + 2D_0 \int_0^t dt' \int_0^t dt'' \langle \xi(t') \cdot \xi(t'') \rangle\end{aligned} \tag{2.33}$$

Neglecting hydrodynamic interaction, the orientation correlation in the first term can be shown to decay exponentially with decay time $\tau_r = 1/D_r$ as $\langle \hat{\mathbf{n}}(t) \cdot \hat{\mathbf{n}}(t') \rangle = (d/N) \exp(-(N-1)|t-t'|/\tau_r)$ (see pg. 298 of Ref. [35] for details of this calculation) where the orientation vector exists in N dimensional space for a projection of the MSD to d dimensional space, the middle term drops out as the noise terms are uncorrelated and the last term is easily evaluated with the delta function in time removing one integral and the dot product picking up the dimensionality d to give

$$\Delta L^2 = 2dD_0 t + \frac{2dv_0^2\tau_r}{N(N-1)^2} \left[(N-1)t + \tau_r \left(e^{-(N-1)t/\tau_r} - 1 \right) \right] \tag{2.34}$$

At times longer than the rotation time $t \gg \tau_r$ this reduces to

$$\Delta L^2 = \left[2dD_0 + \frac{2dv_0^2\tau_r}{N(N-1)} \right] t \tag{2.35}$$

giving an effective diffusion coefficient $\Delta L^2 = 2dD_{\text{eff}}t$ of

$$D_{\text{eff}} = D_0 + \frac{v_0^2\tau_r}{N(N-1)} \tag{2.36}$$

A comparison of the MSD for different projections and dimensions can be see in Figure 2.2. The projection is relevant for colloids diffusing in three dimensional spaced but imaged on

a two dimensional plane, such in standard microscopy. In this case the relevant expression for analysis of the trajectory would be $N = 3$, $d = 2$. Diffusion of discs in two-dimensions is given by $N = 2$, $d = 2$ and spheres in three-dimensional space $N = 3$, $d = 3$.

These Langevin equations can be solved numerically using σ and σ^2/D_0 for units of length and time with the update formulae

$$\mathbf{r}^{(n+1)} = \mathbf{r}^{(n)} + \mathrm{Pe}\,\hat{\mathbf{n}}^{(n)}\Delta t + \sqrt{2\Delta t}\boldsymbol{\xi}^{(n)} \tag{2.37}$$

$$\hat{\mathbf{n}}^{(n+1/2)} = \hat{\mathbf{n}}^{(n)} + \sqrt{6\Delta t}\,\boldsymbol{\eta}^{(n)} \times \hat{\mathbf{n}}^{(n)} \tag{2.38}$$

$$\hat{\mathbf{n}}^{(n+1)} = \frac{\hat{\mathbf{n}}^{(n+1/2)}}{|\hat{\mathbf{n}}^{(n+1/2)}|} \tag{2.39}$$

The random vectors $\boldsymbol{\xi}^{(n)}$ and $\boldsymbol{\eta}^{(n)}$ have their components drawn from a zero mean and unit deviation normal distribution at each step and the orientation update has a normalisation sub step.

In two dimensions we can either specify the orientational noise to only have the z component non zero $\boldsymbol{\eta} = (0, 0, \eta_x)$ or, equivalently, we can write a Langevin and its corresponding update equation for the orientation angle $\theta(t)$

$$\frac{d\theta(t)}{dt} = \eta_z(t) \tag{2.40}$$

$$\theta^{(n+1)} = \theta^{(n)} + \sqrt{6\Delta t}\,\eta_z^{(n)} \tag{2.41}$$

The two-dimensional director $\hat{\mathbf{n}}^{(n)} = (\cos\theta^{(n)}, \sin\theta^{(n)})$ is guaranteed to be normalised at all times.

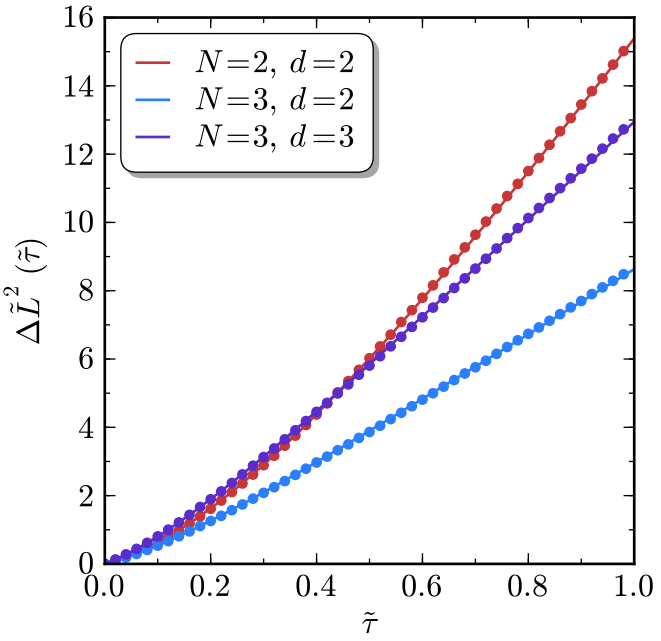

FIGURE 2.2: A comparison of the MSD as a function of the time lag, τ, of a self-propelled particle undergoing rotational diffusion in two and three dimensional space, $N = 2$ and 3, projected to two and three dimensions, $d = 2$ and 3 as given by (2.34) expressed in non-dimensional quantities $L = \sigma\tilde{L}$, $\tau = (\sigma^2/D)\tilde{\tau}$ where σ is the colloid diameter.

In three dimensions the normalisation sub step can be removed by modifying the update equation to take the form [19, 36]

$$\hat{\mathbf{n}}^{(n+1)} = \sqrt{6\Delta t}\left(\eta \times \hat{\mathbf{n}}^{(n)}\right) - 6\Delta t\hat{\mathbf{n}}^{(n)} \tag{2.42}$$

The accuracy of normalisation depends on the fineness of the time step.

Chapter 3

Thermally active colloids

3.1 Introduction

Thermally active colloids receive energy through the absorption of light and can self-propel by thermophoresis through the generation of local asymmetric temperature fields. These asymmetric temperature fields can arise by asymmetric surface patterning or anisotropic illumination. We will consider two cases: a colloid half coated with an optically absorbing material under isotropic illumination and a uniformly absorbing colloid with directed illumination.

The thermophoretic drift velocity of a colloid $\mathbf{v} = -D_T \nabla T$ can show either *thermorepulsive* motion to colder temperatures for positive thermophoretic mobility, $D_T > 0$, or *thermoattractive* motion to hotter temperatures for $D_T < 0$ [26]. The thermoattractive case becomes particularly interesting for collections of thermally active colloids as not only do the particles act as heat sources, they are also heat seeking. This source and seek combination leads to aggregation, which has a biological analogy in chemotaxis, the aggregation of bacteria through sensing chemical gradients. Thermally active colloids

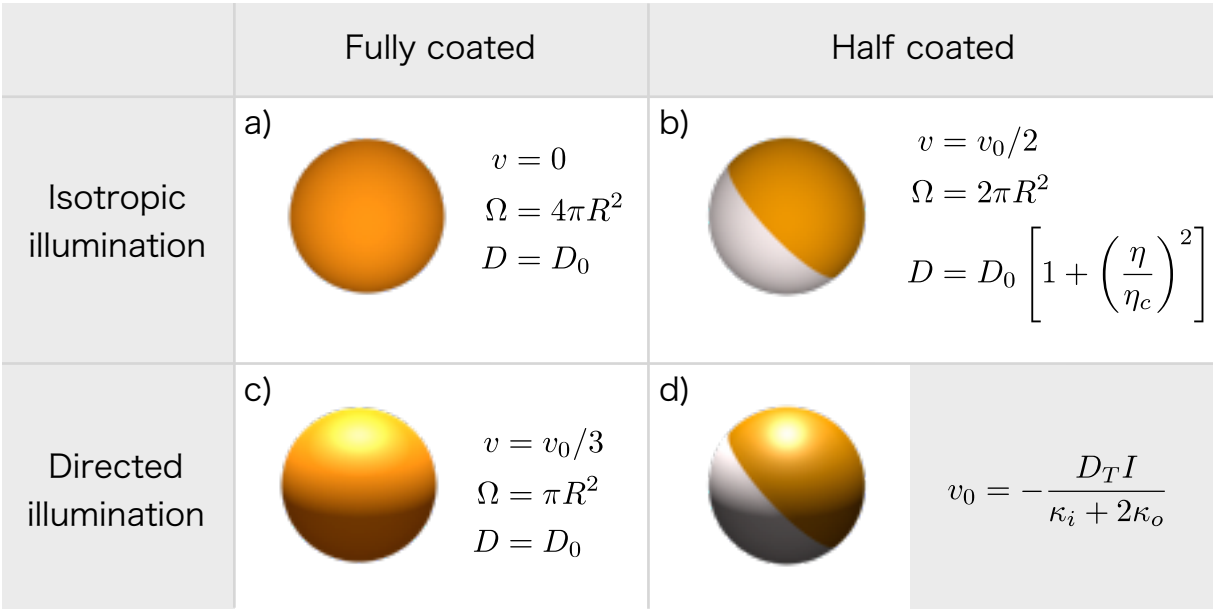

FIGURE 3.1: The nature of the propulsive and diffusive motion of the colloid depends upon the illumination and coating. Of the four possible cases with fully or half coated colloids under isotropic or directed illumination we consider a), b) and c). The self-propulsion velocity v, absorption area Ω and diffusion coefficient D are summarised in terms of the characteristic velocity v_0 (bottom right), where D_T is there thermophoretic mobility and κ_i and κ_o are the thermally conductivities inside and outside the colloid, D_0 is the self diffusion coefficient and η is the thermophoretic coupling strength described in the text.

can therefore have two components to their motion: self propulsion from locally asymmetric temperature distributions, and collective propulsion due to the temperature field generated by the assembly of heat sources.

In order to couple the temperature field generated from absorption of laser light to the phoretic velocity of the colloid as given in (2.27) we must satisfy the thin boundary layer approximation as described in the last chapter. The temperature field around a neutral sphere decays as $1/r$ and so within a simple single component fluid the boundary layer approximation cannot be made. However, this is a very idealised system and in practice subtle interactions between the colloid and solvent or other interfacial effects can be modulated by the temperature field giving rise to a boundary layer and interfacial flow [26]. One could also consider complex fluids such as solvent-polymer mixtures [18], or

charged colloids electrolyte solutions [27, 33] where a finite interaction range is present. The investigation of colloid Soret coefficients remains a theoretically and experimentally challenging pursuit, but despite the difficulties in its microscopic origin a wide range of positive and negative Soret coefficients have been observed experimentally and the theory of thermophoretic colloidal transport sits comfortably within the theory irreversible thermodynamics [29] on the proviso that temperature gradients remain small. This suggests that the boundary layer approximation is valid in many practical situations.

There is a close relationship between temperature and concentration fields as both follow a diffusion equation. Thermally active colloids are therefore closely related to their chemically active counterparts that propel through diffusiophoresis. The major contrast is the separation of time scales, with heat diffusion occurring three orders of magnitude faster than the particle diffusion of catalytic products. It is also important to consider the differing boundary conditions between the two and how they receive the 'fuel' for propulsion. Despite this, there should be many similarities between thermally and chemically powered colloids and the study of one should benefit the other.

The propagation, scattering and absorption of light through a suspension of particles, steric interaction during aggregation and near field hydrodynamics are features of a physical system of thermally active colloids that make it both interesting and challenging. Our aim in the remainder of Part I is to start with a basic model of thermally active colloids and successively introduce features to the theory in order to capture some of these effects.

In this chapter we will introduce our thermally active colloid model and formulate its collective dynamics with and without excluded volume interaction.

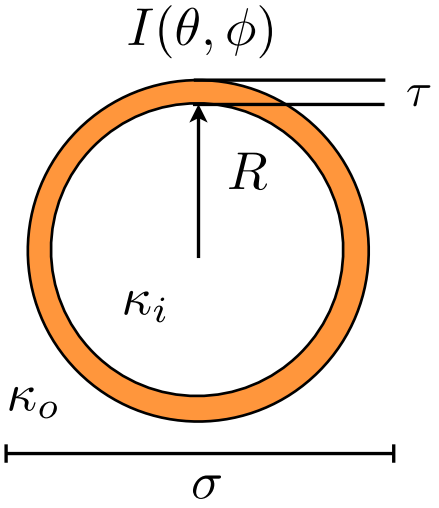

FIGURE 3.2: Schematic diagram for the colloid with radius R and diameter σ coated by an absorbing layer of thickness τ. The coating thickness, τ, should not be confused with the interfacial layer thickness, δ , introduced in the last chapter. We take the limit that the absorbing shell is infinitesimally thin, $\tau/R \ll 1$. This is a good approximation for nanometre coatings on micron sized colloids. The colloid absorbs light through a surface intensity distribution $I(\theta, \phi)$ with spherical angles θ and ϕ, and has thermally conductivities κ_i and κ_o inside and outside the colloid.

3.2 Colloid model

3.2.1 Introduction

The absorption and scattering of light by small particles is, in itself, a large area of research [37]. The optical properties depend on the relative size of the particle, R, to the wavelength of light, λ. For the limit where $R \ll \lambda$ the particle can be considered as a dipole and Rayleigh scattering approximations can be made. For the case $R \gg \lambda$ we enter the domain of geometric optics and ray tracing can be used. For a spherical particle illuminated by a plane wave the Mie theory provides a solution for all classical length scales. Considering multiple scattering quickly becomes computationally very expensive.

As our primary interest is in the collective dynamics of many particles we will use a simple model of optics near the ray tracing approximation to simplify the pursuit.

We assume the colloid to be coated with an infinitesimally thin layer of thickness τ that absorbs monochromatic light with an efficiency, ϵ, that is so high that multiple scattering is negligible. We use the locally received light intensity, $I(\theta, \phi)$, as a heat flux boundary condition in the steady state solutions of the heat equations for the interior and exterior domains to find the temperature on the surface as a spherical harmonic expansion, see Figure 3.2. In a later chapter we will consider the obstruction of light by surrounding colloids and evaluate the incident light distribution, $I(\theta, \phi)$, for each particle. In preparation for this we will relate the surface temperature and intensity expansion coefficients. To conclude the model we will evaluate the self-propulsion velocity for a half coated isotropically illuminated colloid and a fully coated colloid under direct illumination providing an expression for the self-propulsion velocity for cases b) and c) in Figure 3.1.

3.2.2 Temperature fields

In steady state the temperature field inside the colloid, $T_i(r, \theta, \phi)$, with thermal conductivity κ_i and outside the colloid, $T_o(r, \theta, \phi)$, with thermally conductivity κ_o satisfies

$$\kappa_i \nabla^2 T_i = 0, \ \kappa_o \nabla^2 T_o = 0 \tag{3.1}$$

The temperature is continuous across the boundary

$$T_i|_{r=R} = T_o|_{r=R} \tag{3.2}$$

with an additional flux due to the light intensity

$$-\kappa_i \nabla T_i|_{r=R} \cdot \hat{\mathbf{r}} = -\kappa_o \nabla T_o|_{r=R} \cdot \hat{\mathbf{r}} - I(\theta, \phi) \tag{3.3}$$

where we will expand $I(\theta, \phi)$ as

$$I(\theta, \phi) = \sum_{lm} I_{lm} Y_{lm}(\theta, \phi) \tag{3.4}$$

The general solutions for the inner and outer regions are [34]

$$T_i(r, \theta, \phi) = \sum_{l,m} A_{lm} r^l Y_{l,m}(\theta, \phi) \tag{3.5}$$

$$T_o(r, \theta, \phi) = \sum_{l,m} \frac{B_{lm}}{r^{l+1}} Y_{l,m}(\theta, \phi) \tag{3.6}$$

The boundary conditions give

$$B_{l,m} = A_{l,m} R^{2l+1} \tag{3.7}$$

$$-\kappa_i \left[l R^{l-1} A_{l,m} \right] = \kappa_o \left[(l+1) \frac{B_{l,m}}{R^{l+2}} \right] + I_{l,m} \tag{3.8}$$

Solving for $B_{l,m}$ we find

$$B_{l,m} = \frac{R^{l+2}}{l\kappa_i + (l+1)\kappa_o} I_{l,m} \tag{3.9}$$

Expanding the temperature at the surface

$$T(\theta, \phi) = \sum_{l,m} S_{l,m} Y_{l,m}(\theta, \phi) \tag{3.10}$$

we find the surface temperature coefficients

$$S_{l,m} = \frac{RI_{l,m}}{l\kappa_i + (l+1)\kappa_o} \tag{3.11}$$

With this expression we can find the phoretic velocity in terms of the incident intensity

$$\mathbf{U} = -\frac{\mu_p}{\sqrt{3\pi}}\frac{1}{\kappa_i + 2\kappa_o}\left[\sqrt{2}(-\mathrm{Re}\left\{I_{1,1}\right\}\hat{\mathbf{x}} + \mathrm{Im}\left\{I_{1,1}\right\}\hat{\mathbf{y}}) - I_{1,0}\hat{\mathbf{z}}\right] \tag{3.12}$$

3.2.3 Thermophoretic velocity

The intensity expansion coefficients are found by

$$I_{l,m} = \iint I(\theta,\phi)Y^*_{l,m}(\theta,\phi)\,d\Omega \tag{3.13}$$

Considering a directed light source illuminating a uniformly coated colloid with intensity I_∞ the projected surface intensity will be given by $I(\theta) = I_\infty \cos\theta$. The x, y components of colloid velocity will be zero due to symmetry in ϕ and the z component requires the expansion coefficient $I_{1,0}$

$$I_{1,0} = \int_0^{\pi/2}\int_0^{2\pi} I_\infty \cos\theta\, Y^*_{1,0}\, \sin\theta d\phi d\theta \tag{3.14}$$

$$= \sqrt{\frac{\pi}{3}} \tag{3.15}$$

This gives a propulsion velocity of

$$\mathbf{U} = -\frac{D_T}{3}\frac{I_\infty}{\kappa_i + 2\kappa_o}\hat{\mathbf{z}} \tag{3.16}$$

For isotropic illumination we have instead

$$I_{1,0} = \int_0^{\pi/2}\int_0^{2\pi} I_\infty Y_{1,0}^* \sin\theta d\phi d\theta \tag{3.17}$$

$$= \frac{\sqrt{3\pi}}{2} \tag{3.18}$$

and we find a propulsion velocity of

$$\mathbf{U} = -\frac{D_T}{2}\frac{I_\infty}{\kappa_i + 2\kappa_o}\hat{\mathbf{z}} \tag{3.19}$$

3.3 Collective dynamics

We begin our discussion of the collective dynamics with an isotropically illuminated thermally active colloid without excluded volume. We will give the equations of motion for the density field and temperature field and write down the associated Langevin equations. The half coated colloid under isotropic illumination will follow the same equation as the uniformly coated colloid, except for differing diffusion and temperature source coefficients. We will then consider excluded volume using a lattice gas formalism to provide a modified density field equation.

3.3.1 Field equations

The equation of motion for the colloid number density of N particles follows the conservation equation

$$\frac{\partial \rho(\mathbf{r}, \mathbf{t})}{\partial t} = -\nabla \cdot \mathbf{J} \tag{3.20}$$

with normalisation

$$\iiint \rho(\mathbf{r}, t)\, d^3 r \;\; = \;\; N \tag{3.21}$$

The probability flux contains diffusive, J_d, and advective, J_a, terms

$$J_d = -\mathcal{D}\nabla\rho(\mathbf{r},t) \tag{3.22}$$

$$J_a = \mathbf{v}_T(\mathbf{r},t)\rho(\mathbf{r},t) \tag{3.23}$$

where $\mathcal{D}$ is the collective diffusion coefficient and may be different from the self diffusion coefficient, D_0, and the particles experience a drift velocity

$$\mathbf{v}_T = -D_T\nabla T(\mathbf{r},t) \tag{3.24}$$

due to the collectively generated temperature field

$$\rho_m c_p \frac{\partial T(\mathbf{r},t)}{\partial t} = \kappa_o \nabla^2 T(\mathbf{r},t) + \gamma\rho(\mathbf{r},t) \tag{3.25}$$

where ρ_m, c_p and κ_o are the mass density, specific heat capacity and thermal conductivity of the fluid. The coefficient $\gamma = \Omega\epsilon I$ couples the colloid density field to the temperature field as a source term and depends upon the surface area of the coating, Ω, and the absorbed intensity ϵI. The thermophoretic mobility D_T could be in general be a collective coefficient that is separate from the interfacial thermophoretic mobility, but we keep the same symbol here for simplicity of notation.

Using units σ, σ^2/D_0 and S_T^{-1} for length, time and temperature respectively, where σ is the colloid diameter and $S_T = D_T/D_0$ is the Soret coefficient, these equations can be

written in the dimensionless form

$$\frac{\partial\tilde{\rho}}{\partial\tilde{t}} = -\tilde{\nabla}\cdot\left[-\tilde{\mathcal{D}}\tilde{\nabla}\tilde{\rho} - (\hat{S}_T\tilde{\nabla}\tilde{T})\tilde{\rho}\right] \tag{3.26}$$

$$\chi\frac{\partial\tilde{T}}{\partial\tilde{t}} = \tilde{\nabla}^2\tilde{T} + \tilde{\gamma}\tilde{\rho} \tag{3.27}$$

$\hat{S}_T = S_T/|S_T|$ sets whether the colloids are thermally attractive ($\hat{S}_T = -1$) or repulsive ($\hat{S}_T = 1$), $\chi = D_0/\alpha$ captures the relative time scales where $\alpha = \kappa/(\rho_m c_p)$ is the thermal diffusivity and the coupling coefficient becomes $\tilde{\gamma} = \pi\tilde{\Omega}\eta$ where $\tilde{\Omega} = \Omega/\pi\sigma^2$ is the dimensionless rescaled surface area and $\eta = \epsilon I|S_T|\sigma/\kappa$ is the thermally active colloid parameter representing the coupling strength and will be used many times in the following discussion. For a uniformly coated sphere $\tilde{\Omega} = 1$ and $\tilde{\mathcal{D}} = 1$. When we consider the case of a half coated sphere, $\tilde{\Omega} = 1/2$, the collective diffusion coefficient becomes η dependent, $\tilde{\mathcal{D}}(\eta)$, as will be shown in a later section.

The timescale parameter χ for a micrometre sized colloid in water at room temperature is around $\chi \sim 10^{-6}$ and so, to good approximation, we can solve the steady state temperature equation

$$\tilde{\nabla}^2 T = -\tilde{\gamma}\tilde{\rho} \tag{3.28}$$

For chemically active colloids $\chi \sim 10^{-3}$ and time dependence may become more relevant. For this reason and general theoretical interest we will consider the effect of χ in some calculations.

3.3.2 Langevin equations

The overdamped Langevin equation for the isotropically illuminated uniformly coated colloid is

$$\frac{\partial \mathbf{r}_i}{\partial t} = \mathbf{v}_{T,i} + \sqrt{2D_0}\boldsymbol{\xi}_i \tag{3.29}$$

with $\langle \xi_{i,\alpha(t)} \rangle = 0$ and $\langle \xi_{i,\alpha}(t)\xi_{j,\beta}(t') \rangle = \delta_{i,j}\delta_{\alpha,\beta}\delta(t-t')$ providing thermal noise consistent with the fluctuation dissipation theorem, where i and j represent particle indices and α and β represent coordinate indices. Particles experience a drift velocity

$$\mathbf{v}_{T,i} = -D_T \nabla_{\mathbf{r}_i} T(\mathbf{r}_i) \tag{3.30}$$

due to the collective temperature field. In steady state the temperature field is given by the sum of all contributions

$$T(\mathbf{r}) = \sum_{i=1}^{N} T_0(|\mathbf{r} - \mathbf{r}_i|) \tag{3.31}$$

Solving the steady state temperature equation for a point source gives the temperature

$$\tilde{T}_0(\tilde{r}) = \frac{\tilde{\Omega}\eta}{4}\frac{1}{\tilde{r}} \tag{3.32}$$

Rotational diffusion can be included as in Section 2.3.1.

3.4 Excluded volume

We will use a lattice gas approach in order to include the effect of excluded volume into the field equations. We will first approach this from the perspective of the free energy of mixing to find that we cannot construct the resulting particle flux as we have to way to specify the mobility, $\Gamma(\rho)$. To overcome this we take the continuum limit of the master equation for a lattice exclusion process. This provides both a modified advective flux term and, by comparing the results, an expression for the mobility.

3.4.1 Free energy of mixing

Although the free energy of mixing doesn't explicitly included excluded volume, it reproduces the tenancy to spread high concentrations of an un-mixed component and can serve as a useful starting point.

We consider a lattice of N sites that can either be vacant or occupied. Given $N_\circ$ vacant sites and $N_\bullet$ occupied sites with $N = N_\circ + N_\bullet$ there are $\Omega = N!/(N_\circ! N_\bullet!)$ possible configurations of the lattice. The entropy of such a state is given by $S = k_b \ln \Omega$ which can be approximated by Stirling's formula as

$$S = -k_b N \left[\left(1 - \frac{N_\bullet}{N}\right) \ln \left(1 - \frac{N_\bullet}{N}\right) + \left(\frac{N_\bullet}{N}\right) \ln \left(\frac{N_\bullet}{N}\right) \right] \tag{3.33}$$

We can rewrite this in a different form by considering a system volume of V with particles of characteristic volume V_0 such that $N = V/V_0$. The fraction of occupied sites $\phi = N_\bullet/N$

can be written as $\phi = \rho V_0$ where $\rho = N_\bullet/V$ is the particle number density.

$$\frac{S}{V} = -\frac{k_b}{v_0}\left[(1-\rho V_0)\ln(1-\rho V_0) + \rho V_0 \ln(\rho V_0)\right] \tag{3.34}$$

We can identify S/V as the entropy density, s, and make the number density space dependent, $\rho \to \rho(\mathbf{r})$, by considering the system volume V as a sub system in a larger volume V', such that the new total entropy will be the integral over the entropy density $S = \iiint s(\mathbf{x}) d^3r$ as

$$S = -\frac{k_b}{V_0}\iiint \left[(1-\rho(\mathbf{x})V_0)\ln(1-\rho(\mathbf{x})V_0) + \rho(\mathbf{x})V_0 \ln(\rho(\mathbf{x})V_0)\right] d^3\mathbf{r} \tag{3.35}$$

We now can express the free energy as a functional of $\rho(\mathbf{r})$

$$\mathcal{F}[\rho(\mathbf{r})] = U - S[\rho(\mathbf{r})]T \tag{3.36}$$

and obtain a dynamic flux through minimisation of this free energy with respect to density

$$\mathbf{J} = -\Gamma(\rho(\mathbf{r}))\nabla\left[\frac{\delta\mathcal{F}[\rho(\mathbf{r})]}{\delta\rho(\mathbf{r})}\right] \tag{3.37}$$

Here we have introduced the transport coefficient Γ, also known as the Onsager coefficient [38], which is specified by the kinetics of the system and can depend on the density. Using the Euler-Langrange equations to perform the variation of the free energy we find

$$\frac{\delta\mathcal{F}[\rho]}{\delta\rho} = -k_b T \ln\left(\frac{\rho V_0}{1-\rho V_0}\right) \tag{3.38}$$

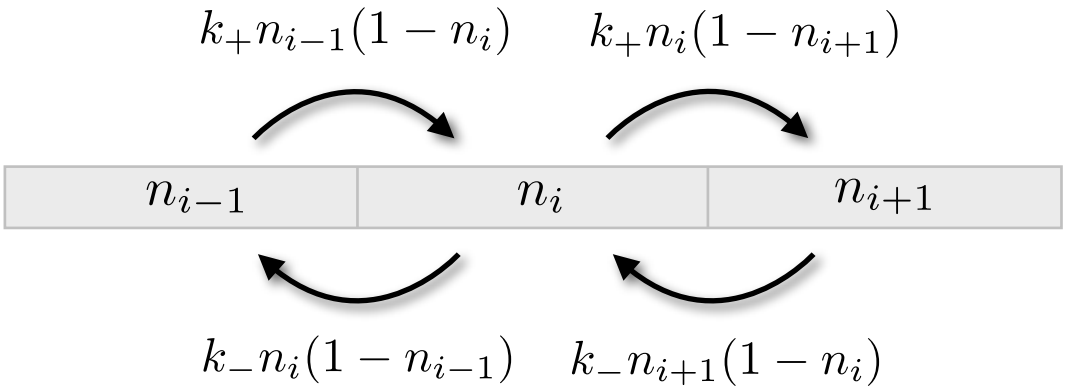

FIGURE 3.3: Diagrammatic representation of the asymmetric simple exclusion process as given by (3.40). Particles move in the positive and negative directions at rates k_+ and k_- only if the cell is unoccupied.

with gradient

$$\nabla\left[\frac{\delta\mathcal{F}[\rho(\mathbf{r})]}{\delta\rho(\mathbf{r})}\right] = -\frac{k_bT}{1-\rho V_0}\frac{\nabla\rho}{\rho} \tag{3.39}$$

For non interacting ideal-gas like particles the free energy is given by $\mathcal{F}_{ni} = -k_bT\int\rho(\ln\rho - 1)$ and by comparison to Fick's law, $J = -D\nabla\rho$, we find $\Gamma(\rho)_{ni} = \rho/\zeta$. For other systems a dynamical model containing information on the kinetics must be used to provide Γ. Assuming the interacting system to follow a diffusive flux with the same form of Fick's law we would expect $\Gamma(\rho)_i = (1-\rho V_0)\rho/\zeta$.

Once a dynamical model has been described it can be useful to map this non-equilibrium process onto an effective free energy picture that satisfies detailed balance such that standard phase separation techniques can be used to describe the system. This approach has been used with great success by Tailleur and Cates [39, 40].

3.4.2 Lattice dynamics

We consider an asymmetric simple exclusion process (ASEP) [41] on a lattice where each cell has an occupancy number, $n_i(t)$, that at any time is either vacant, $n_i = 0$, or occupied, $n_i = 1$. Particles can only move on the lattice to vacant sites, with a jump rate that can differ in the positive, k_+, and negative, k_-, directions, see Figure 3.3. The dynamics of a bulk cell in one dimension has four contributions

$$\begin{aligned} \frac{dn_i}{dt} &= k_+ n_{i-1}(1-n_i) - k_- n_i(1-n_{i-1}) \\ &- k_+ n_i(1-n_{i+1}) + k_- n_{i+1}(1-n_i) \end{aligned} \tag{3.40}$$

We can rewrite this equation in terms of average diffusive, $\bar{k} = (k_+ + k_-)/2$, and drift, $\Delta k = (k_+ - k_-)/2$, rate constants

$$\begin{aligned} \frac{dn_i}{dt} &= \bar{k}\,(n_{i-1} - 2n_i + n_{i+1}) \\ &+ \Delta k\,(n_{i-1} - 2n_{i-1}n_i + 2n_i n_{i+1} - n_{i+1}) \end{aligned} \tag{3.41}$$

and take the continuum limit of the occupancy to probability $p(x,t)$

$$\begin{aligned} n_i(t) &\to p(x,t) \\ n_{i+1}(t) &\to p(x,t) + \epsilon\partial_x p(x,t) + \frac{\epsilon^2}{2}\partial_x^2 \rho(x,t) \\ n_{i-1}(t) &\to p(x,t) - \epsilon\partial_x p(x,t) + \frac{\epsilon^2}{2}\partial_x^2 p(x,t) \end{aligned}$$

giving

$$\frac{\partial p}{\partial t} = \epsilon^2 \bar{k} \partial_x^2 p + 2\epsilon \Delta k \left(\partial_x p^2 - \partial_x \rho \right) \tag{3.42}$$

Rewriting in the second advective-like term in the continuity form $\dot{p} = -\partial_x J_a$ we see

$$J_a = 2\epsilon \Delta \kappa (1-p) p \tag{3.43}$$

which can be interpreted as a modified drift velocity, $v_{\text{ex}} = v(1-p)$, that advects the probability, p.

In terms of thermally active colloids the number density, ρ, is related to the probability by $\rho = p/V_0$, suggesting a modified excluded volume advection flux of the form

$$\mathbf{J}_a^{(ex)} = -(D_T \nabla T) \left(1 - \frac{\rho(\mathbf{r})}{\rho_{\max}} \right) \rho(\mathbf{r}) \tag{3.44}$$

where characteristic volume can be identified as $\rho_{\max} = 1/V_0$.

3.5 With orientation

A half coated particle under isotropic illumination will have a self propulsion velocity $v_0 = -D_T I/(2(\kappa_i + 2\kappa_o))$ in direction $\hat{\mathbf{n}}$ that will undergo rotational diffusion. At time scales longer than the rotational diffusion time this results in an effective diffusion coefficient of $D_{\text{eff}} = D_0 + v_0^2/(6D_r)$, as given in Section 2.3.1, and so the collective diffusion coefficient

becomes

$$\mathcal{D}(\eta) = \left[1 + \frac{1}{18}\left(\frac{\eta}{2(\tilde{\kappa}_i + 2)}\right)^2\right] D_0 \tag{3.45}$$

If we assume that the thermal conductivity of the colloid and the fluid are comparable, $\tilde{\kappa_i} = 1$, then the thermophoretic strength must become larger than $\eta_c = 18\sqrt{2} \sim 26$ in order for rotational diffusion to be dominant. If we assume that the colloids are highly insulating, such that $\tilde{\kappa}_i \to 0$, then $\eta_c = 12\sqrt{2} \sim 17$.

An alternative formulation of the equations of motion begins from the master equation for the probability distribution $p(\mathbf{r}, \hat{\mathbf{n}})$ to find a particle at position $\mathbf{r}$ and orientation $\hat{\mathbf{n}}$. By considering time scales longer than the rotational diffusion time an equivalent closed form solution for the density field can be found. The alternative formalism allows for a more general method of constructing the field equations and could be used to introduce orientational couplings. For further information see references [40, 42].

3.6 Summary

We can combine these results into a set of general dimensionless equations

$$\chi \frac{\partial \tilde{T}}{\partial \tilde{t}} = \tilde{\nabla}^2 \tilde{T}(\tilde{x}, \tilde{t}) + \tilde{\gamma}\tilde{\rho}(\tilde{x}, \tilde{t}) \tag{3.46}$$

$$\frac{\partial \tilde{\rho}(\tilde{x}, \tilde{t})}{\partial \tilde{t}} = -\nabla \cdot \left[-\tilde{\mathcal{D}}(\eta)\tilde{\nabla}\tilde{\rho}(\tilde{x}, \tilde{t}) - \left(\hat{S}_T \tilde{\nabla}\tilde{T}(\tilde{x}, \tilde{t})\right) \mathcal{A}(\tilde{\rho}, \phi)\tilde{\rho}(\tilde{x}, \tilde{t})\right] \tag{3.47}$$

The coupling coefficient will take the form $\tilde{\gamma} = \pi\eta\nu\tilde{\Omega}\phi$ where $\eta = |S_T|I\sigma/\kappa$ is the thermophoretic strength and can be controlled by the light intensity I, ν will depend on the

	non interacting	excluded volume
half coated, $\tilde{\Omega} = 1/2$	η, $\nu\phi$	η, ν, ϕ
fully coated, $\tilde{\Omega} = 1$	$\tilde{\gamma}$	$\eta\nu$, ϕ

TABLE 3.1: Free parameter combinations for the four possible cases that form the coupling parameter $\tilde{\gamma} = \pi\eta\nu\tilde{\Omega}\phi_L$. The individual parameters are defined as $\eta = |S_T|I\sigma/\kappa$ the thermophoretic strength, ϕ the packing fraction and ν a geometric confinement parameter are dependent on the dimension/confinement, $\tilde{\Omega} = \Omega/(\pi\sigma^2)$ the rescaled absorption area where Ω is the absorption surface area.

number of particles and the geometry of the system, $\tilde{\Omega} = \Omega/(\pi\sigma^2)$ is the rescaled dimensionless absorption area, Ω, with $\tilde{\Omega} = 1$ for a fully coated sphere and $\tilde{\Omega} = 1/2$ for half coated and ϕ will represent the packing fraction of particles with $0 \leq \phi \leq 1$.

The dimensionless collective diffusion coefficient, $\tilde{\mathcal{D}}(\eta)$, depends on the coating of the colloid and thermophoretic strength η. For a fully coated sphere $\tilde{\mathcal{D}} = 1$ and for a half coated sphere the collective diffusion coefficient becomes $\tilde{\mathcal{D}} = 1 + (\eta/\eta_c)^2$ with $\eta_c = 18\sqrt{2}$. The advective flux modifier $\mathcal{A}(\tilde{\rho})$ will equal unity without excluded volume, $\mathcal{A} = 1$, and with excluded volume $\mathcal{A}(\tilde{\rho}) = (1 - \tilde{\rho}/\tilde{\rho}_{\max})$, where $\tilde{\rho}_{\max} = 1/\phi$.

There are four cases we can consider resulting from whether the colloid is half or fully coated and whether or not we include excluded volume. These decisions will result in a different set of free parameters to explore the system, see Table 3.1. These free parameters can in principle always be supplemented with the relative time scale χ and the colloid conductivity $\tilde{\kappa}_i$, but we will set $\tilde{\kappa}_i = 1$ for the remainder of the discussion and only consider χ.

Chapter 4

Aggregation and dynamic collapse

4.1 Introduction

The thermally active colloid model was introduced in the previous chapter along with a set of equations for their collective behaviour. In this chapter we will study some solutions to these equations of motion with and without excluded volume for the thermoattractive case.

These equations of motion have previously been studied without excluded volume. Golestanian (2012) has drawn analogies between the thermorepulsive equilibrium solutions and the Poisson-Boltzmann equation for counter ion condensation and has studied some of the properties of the attractive solution [42]. The equations for the attractive case take the same form of a widely studied approximation of the Keller-Segel equation for bacteria chemotaxis [43]. These equations can also be viewed as a self gravitating system in the viscous hydrodynamics regime [44].

Bacterial colonies starting from a small population have been observed to grow into highly symmetric patterns known as chemotactic rings [9]. Biological pattern formation has long

been of interest to mathematicians with a history that stems from the morphogenesis study of Turing (1952) [45]. Attention has turned to the physical mechanisms behind this pattern formation with the work of Brenner *et al.* (1998) [46]. Cates *et al.* (2010) have shown that pattern formation can result from a density dependent motility of self propelled particles [47]. This can lead to so called *active phase separation* with a persistent dissipation of energy as opposed to its equilibrium counterpart. Fily *et. al* (2012) have shown that introducing excluded volume between self propelled particles is sufficient to form an active high density and low density phase [48].

The directed self-assembly of phase separating block-copolymers has recently received much attention in order to reproducibly fabricate nanoscale features for the semiconductor industry [49]. Taking example from this success, one can imagine that active phase separation could lead to patterned domains with dynamic flowing channels. This could lead to more complicated self-assembled chemical processing devices, or to biomimetic systems that self-organise into regulatory channels that draw in 'nutrients' and expel 'waste', as develops in biofilms [50].

One particularly interesting feature of the simplified Keller-Segel equations is the so called *chemotactic blow-up* that arises in solutions of the equation in space dimensions higher than one. These blow-ups have been widely studied and occur at a critical mass and at finite time and have been investigated using methods such as similarity solutions and free energy-like functionals [51, 52]. In the thermally active colloid system these blow-ups could lead to further explosive thermal instabilities, however, it is important to consider excluded volume in order to maintain physical densities.

4.2 Methods

To numerically study the dynamics of colloid number density we will discretise the equation of motion using an approach based on the finite volume method (FVM). The finite volume method discretises the integral form of the differential equation and is particularly suited to conservation laws [53], providing a consistent framework for construction of higher order solutions [54], adaptive cells [55] and inclusion of shock capturing methods [56].

We will briefly outline the discretisation process for a grid of simple square cell with side length Δl. We will discretise the flux from the conservation law using upwind advection for greater stability. Once this flux function is specified the colloid dynamics can be iterated numerically. We use first order Euler time integration here but higher order methods, such as the Runge-Kutta family [57], could be used.

Given a general conservation law of the form $\partial_t \rho(\mathbf{x}, t) = -\nabla \cdot \mathbf{J}$ we can integrate over a control cell $C_{i,j}$ and use the divergence theorem to consider the flux through the cell. The contour integral of the flux can be broken into individual integrals across the face. We can approximate the integrals using the midpoint rule and use Euler rule for time integration to write an expression for the average density update as

$$\rho_{\mathbf{c}}^{(n+1)} = \rho_{\mathbf{c}}^{(n)} + \frac{\Delta t}{\Delta l} \sum_{\hat{\mathbf{f}}_i}^{F_{\mathbf{c}}} J(\mathbf{c}, \mathbf{c} + \hat{\mathbf{f}}_i) \tag{4.1}$$

where $\mathbf{c} = (i, j)$ gives the coordinates of the cell on the Cartesian grid and $F_{\mathbf{c}}$ is the set of faces for cell indices $\mathbf{c}$. This will depend on the boundary conditions as, for instance, for

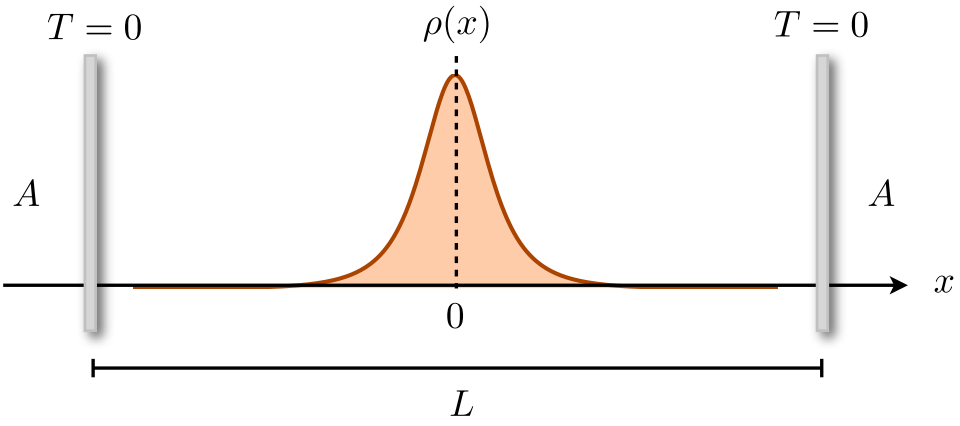

FIGURE 4.1: Schematic of the one-dimensional system. Two plates of area A are held at temperature $T = 0$ and separated by a distance L. The colloids are confined between the two plates and aggregate in 'sheets' given by density $\rho(x)$.

no flux boundary conditions some faces will be omitted. Each face $\hat{\mathbf{f}}_i$ has a corresponding outward normal unit vector $\hat{\mathbf{f}}_i \in \{(0,1),(0,-1),(1,0),(-1,0)\}$, which can used to access the neighbouring cell, $\mathbf{d} = \mathbf{c}+\hat{\mathbf{f}}_i$. The flux function is given by $J(\mathbf{c},\mathbf{d}) = J_D(\mathbf{c},\mathbf{d})+J_A(\mathbf{c},\mathbf{d})$ with the diffusive flux, J_D, simply given by $J_D = -(\rho_\mathbf{d} - \rho_\mathbf{c})/\Delta l$ where $\rho_\mathbf{c}$ is the density of the current cell and $\rho_\mathbf{d}$ is the density of the cell through the connecting face. The advective flux, $J_A(\mathbf{c},\mathbf{d}) = v_f\rho_\mathbf{e}$, depends upon the sign of the advection though the face due to temperature, $v_f = -\hat{S}_T(T_\mathbf{d} - T_\mathbf{c})/\Delta l$, if $v_f > 0$ then $\rho_\mathbf{e} = \rho_\mathbf{c}$ and if $v_f < 0$ then $\rho_\mathbf{e} = \rho_\mathbf{d}$, this is known as upwind advection [56]. For excluded volume the advective flux term is modified to $J_A(\mathbf{c},\mathbf{d}) = v_f(1 - \rho_\mathbf{e}/\rho_\mathbf{max})\rho_\mathbf{e}$ with $\rho_\mathbf{e}$ specified by the upwind rule as before.

Writing an update equation in this form is particularly convenient as the flux function needs only to be specified once in the numerical procedure.

4.3 One dimension

We consider the case where spatial variations only occur in one dimension $\rho(x)$, for instance, if the system is confined between two 'semi-infinite' plates of fixed temperature separated by distance L. We can consider the colloids arranging into N_L sheets with a fixed number of colloids per sheet, N_A, to give the total number of colloids $N = N_A N_L$. Since each sheet will be σ thick there can be a maximum of $\tilde{L} = L/\sigma$ sheets in the system. Without excluded volume the only length scale in the system is L and we use units of L, L^2/D_0, $|S_T|^{-1}$ and $N/(AL)$ for length, time, temperature and density to give the reduced equations of motion

$$\chi \frac{\partial \tilde{T}}{\partial \tilde{t}} = \frac{\partial^2 \tilde{T}(\tilde{x},\tilde{t})}{\partial \tilde{x}^2} + \tilde{\gamma}\tilde{\rho}(\tilde{x},\tilde{t}) \tag{4.2}$$

$$\frac{\partial \tilde{\rho}(\tilde{x},\tilde{t})}{\partial \tilde{t}} = -\frac{\partial}{\partial \tilde{x}}\left[-\tilde{\mathcal{D}}(\eta)\frac{\partial \tilde{\rho}(\tilde{x},\tilde{t})}{\partial \tilde{x}} - \left(\hat{S}_T \frac{\partial \tilde{T}(\tilde{x},\tilde{t})}{\partial \tilde{x}}\right)\mathcal{A}(\tilde{\rho},\phi_L)\tilde{\rho}(\tilde{x},\tilde{t})\right] \tag{4.3}$$

$$\int_{-1/2}^{1/2} d\tilde{x}\, \tilde{\rho}(\tilde{x},t) = 1 \tag{4.4}$$

The coupling coefficient is $\tilde{\gamma} = \pi\eta\nu\tilde{\Omega}\phi_L$ where $\eta = |S_T|I\sigma/\kappa$, $\nu = L^2 N_A/A$ and $\phi_L = N_L/\tilde{L}$. The maximum density is given by the number of colloids in a single sheet $\rho_{\max} = N_A/(\sigma A)$, which becomes $\tilde{\rho}_{\max} = 1/\phi_L$ in dimensionless units.

4.3.1 Equilibrium solution

In equilibrium without excluded volume equations (4.2) and (4.3) become

$$\frac{d^2\tilde{T}(\tilde{x})}{d\tilde{x}^2} = -\tilde{\gamma}\tilde{\rho}(\tilde{x}) \tag{4.5}$$

$$\frac{1}{\tilde{\rho}(\tilde{x})}\frac{d\tilde{\rho}(\tilde{x})}{d\tilde{x}} = -\frac{\hat{S}_T}{\tilde{\mathcal{D}}(\eta)}\frac{d\tilde{T}}{d\tilde{x}} \tag{4.6}$$

We can write the left hand side of (4.6) as $\partial_{\tilde{x}} \ln \tilde{\rho}(\tilde{x})$, integrate from the centre of the system $\tilde{x} = 0$ to $\tilde{x}$, set $T(0) = 0$ and solve for $\tilde{\rho}(\tilde{x})$ to find

$$\tilde{\rho}(\tilde{x}) = \tilde{\rho}_0 \exp\left(-\frac{\hat{S}_T}{\tilde{\mathcal{D}}(\eta)}\tilde{T}(\tilde{x})\right) \tag{4.7}$$

Substituting this into the temperature equation (4.5) yields the differential equation

$$\frac{d^2\tilde{T}(\tilde{x})}{d\tilde{x}^2} = -\tilde{\gamma}\tilde{\rho}_0 \exp\left(-\frac{\hat{S}_T}{\tilde{\mathcal{D}}(\eta)}\tilde{T}(\tilde{x})\right) \tag{4.8}$$

For $\hat{S}_T < 0$ we have the following solutions for temperature and density

$$\tilde{T}(\tilde{x}) = \tilde{\mathcal{D}}(\eta) \ln\left[\mathrm{sech}^2\left(\tilde{x}\sqrt{\frac{\tilde{\gamma}\tilde{\rho}_0}{2\tilde{\mathcal{D}}(\eta)}}\right)\right] \tag{4.9}$$

$$\tilde{\rho}(\tilde{x}) = \tilde{\rho}_0 \mathrm{sech}^2\left(\tilde{x}\sqrt{\frac{\tilde{\gamma}\tilde{\rho}_0}{2\tilde{\mathcal{D}}(\eta)}}\right) \tag{4.10}$$

Using the divergence theorem on (4.5) we find the steady state relationship between the flux at the boundary and the heat source, $\partial_{\tilde{x}}\tilde{T}|_{\tilde{x}=1/2} = -\tilde{\gamma}/2$, and combine this with (4.9)

to provide a transcendental equation for the density at the centre of the system, ρ_0.

$$\alpha = \beta \tanh \beta \tag{4.11}$$

$$\alpha = \frac{\tilde{\gamma}}{8\tilde{\mathcal{D}}(\eta)}, \qquad \beta = \frac{1}{2}\sqrt{\frac{\tilde{\gamma}\tilde{\rho}_0}{2\tilde{\mathcal{D}}(\eta)}} \tag{4.12}$$

where α is a known quantity and β is solved for to find $\tilde{\rho}_0 = \beta^2/\alpha$. For small β we can approximate $\tanh\beta \sim \beta$ to find $\alpha = \beta^2$ and so $\tilde{\rho}_0 \to 1$ for $\tilde{\gamma}/\tilde{\mathcal{D}} \to 0$. At large β we have the asymptote $\tanh\beta \to 1$ and so for $\tilde{\gamma}/\tilde{\mathcal{D}} \to \infty$ we have $\tilde{\rho}_0 \to \tilde{\gamma}/(8\tilde{\mathcal{D}})$. The density can be expressed as $\tilde{\rho}(\tilde{x}) = \beta^2 \mathrm{sech}^2(2\beta\tilde{x})/\alpha$ which takes the form $\tilde{\rho}(\tilde{x}) = \alpha \mathrm{sech}^2(2\alpha\tilde{x})$ at large α. From this we can calculate the second moment $\sigma^2(\alpha) = \int \tilde{x}^2\tilde{\rho}(\tilde{x},\alpha)$, which scales as α^{-2} and so the width of the aggregation is inversely proportional to $\tilde{\gamma}$ at strong interaction.

We can find a relationship between the density at the edge and the middle of the system [58] by differentiating $\tilde{\rho}(\tilde{x})$ in (4.7) with respect to $\tilde{x}$ to find

$$\frac{d\tilde{\rho}(\tilde{x})}{d\tilde{x}} = \frac{\tilde{\rho}(\tilde{x})}{\tilde{\mathcal{D}}(\eta)}\frac{d\tilde{T}(\tilde{x})}{d\tilde{x}} \tag{4.13}$$

Substituting (4.5) yields the differential equation

$$\frac{d\tilde{\rho}(\tilde{x})}{d\tilde{x}} = -\frac{1}{\tilde{\gamma}\tilde{\mathcal{D}}(\eta)}\frac{d^2\tilde{T}(\tilde{x})}{d\tilde{x}^2}\frac{d\tilde{T}(\tilde{x})}{d\tilde{x}} \tag{4.14}$$

Using $\partial_x[(\partial_x T)^2] = 2\partial_x T \partial_x^2 T$ and integrating from the centre $\tilde{x} = 0$ to the edge $\tilde{x} = 1/2$

$$\tilde{\rho}_e - \tilde{\rho}_0 = -\frac{1}{2\tilde{\gamma}\tilde{\mathcal{D}}(\eta)}\left[\left(\frac{d\tilde{T}}{d\tilde{x}}\right)^2\Bigg|_{\tilde{x}=1/2} - \left(\frac{d\tilde{T}}{d\tilde{x}}\right)^2\Bigg|_{\tilde{x}=0}\right] \tag{4.15}$$

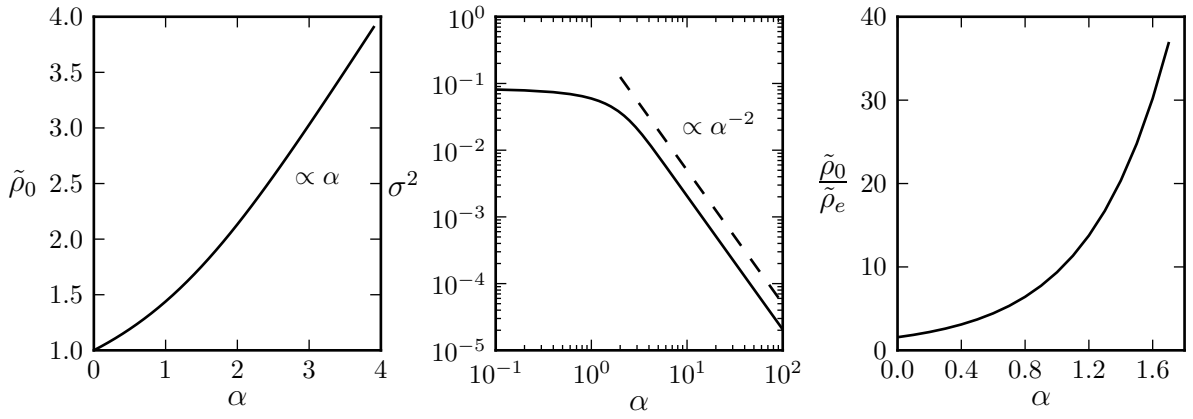

FIGURE 4.2: Equilibrium properties of a one-dimensional aggregation of thermally active colloids without excluded volume. The density at the centre of the cell increases linearly at high $\alpha = \tilde{\gamma}/8\tilde{\mathcal{D}}(\eta)$ (left) with the width becoming inversely proportional to α (middle) and the depletion growing exponentially (right).

where from the divergence theorem we have $\partial_{\tilde{x}} T|_{\tilde{x}=1/2} = -\tilde{\gamma}/2$ and from symmetry $\partial_{\tilde{x}} T|_{\tilde{x}=0} = 0$ giving $\tilde{\rho}_0 - \tilde{\rho}_e = \tilde{\gamma}/(2\tilde{\mathcal{D}})$, which can be expressed as a ratio of the middle to the edge density as

$$\frac{\tilde{\rho}_0}{\tilde{\rho}_e} = \frac{1}{1 - (\alpha/\beta)^2} \tag{4.16}$$

where $(\alpha/\beta)^2 = \tilde{\gamma}/(8\tilde{\rho}_0\tilde{\mathcal{D}}(\eta))$ and β is found from the transcendental equation (4.11) as before. A summary of some of the properties of the equilibrium solution is shown in Figure 4.2

4.3.2 Steady temperature field

In the limit that thermal diffusion is faster than the colloid diffusion, $\chi \to 0$, we solve the steady temperature equation, $\tilde{\nabla}^2\tilde{T} = -\tilde{\gamma}\tilde{\rho}$. Through discretisation using the finite

volume method (FVM) we obtain the three-point stencil

$$\frac{\tilde{T}_{i-1} - 2\tilde{T}_i + \tilde{T}_{i+1}}{\Delta l^2} = -\tilde{\gamma}\tilde{\rho}_i \tag{4.17}$$

We can solve (4.17) with, Dirichlet, zero temperature boundary conditions by writing the discretisation in the matrix form $KU = F$

$$\frac{1}{\Delta l^2}\begin{pmatrix} -2 & 1 & & & & \\ 1 & -2 & 1 & & & \\ & \ddots & \ddots & \ddots & & \\ & & 1 & -2 & 1 & \\ & & & 1 & -2 & \end{pmatrix}\begin{pmatrix} \tilde{T}_1 \\ \tilde{T}_2 \\ \vdots \\ \tilde{T}_{N-1} \\ \tilde{T}_N \end{pmatrix} = -\tilde{\gamma}\begin{pmatrix} \tilde{\rho}_1 \\ \tilde{\rho}_2 \\ \vdots \\ \tilde{\rho}_{N-1} \\ \tilde{\rho}_N \end{pmatrix} \tag{4.18}$$

where the K matrix has a tridiagonal structure and we can solve for F in $\mathcal{O}(N)$ time using the tridiagonal matrix algorithm (TDMA) [57], also known as the Thomas algorithm.

We initially prepare the colloids in a uniform distribution. At $\tilde{\gamma} = 0$ there will be no generation of a temperature field in the system and the colloids would remain in the equilibrium uniform state. As $\tilde{\gamma} = 0$ increases more heat is absorbed, but as we are in steady state the amount of heat entering is balanced by the heat flux out of the system. The boundary conditions result in a smooth temperature profile forming with a negative curvature peaking at the middle. This temperature field with negative Soret coefficient drives the colloids to the centre of the system forming a condensate with density increasing linearly with $\tilde{\gamma} = 0$ unless excluded volume is present.

From the initial uniform distribution a travelling front can be seen to develop at the

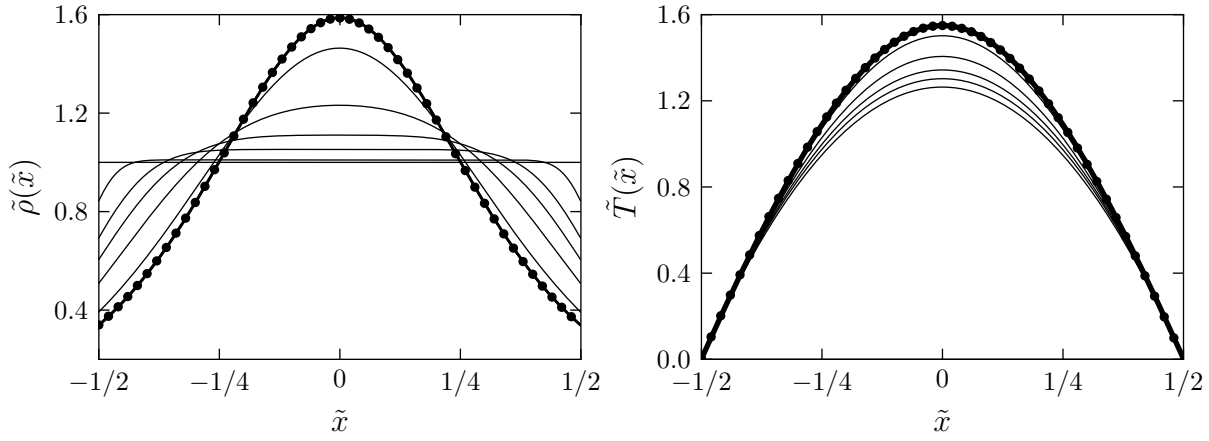

FIGURE 4.3: Snapshots of density and temperature fields at times $\tilde{t} = 1e^{-3}, 5e^{-3}, 1e^{-2}, 2e^{-2}, 5e^{-2}$ and 1.0 for a fully coated colloid without excluded volume with $\tilde{\gamma} = 10$ using (4.1) & (4.18) . For the final type the analytical equilibrium solution, as given by (4.9) & (4.10), is plotted in a thick line with numerical data shown with circle markers. Non-dimensional quantities $\rho = N/(AL)\tilde{\rho}$, $x = L\tilde{x}$, $t = L^2/D\tilde{t}$ and $T = |S_T|^{-1}\tilde{T}$ have been used.

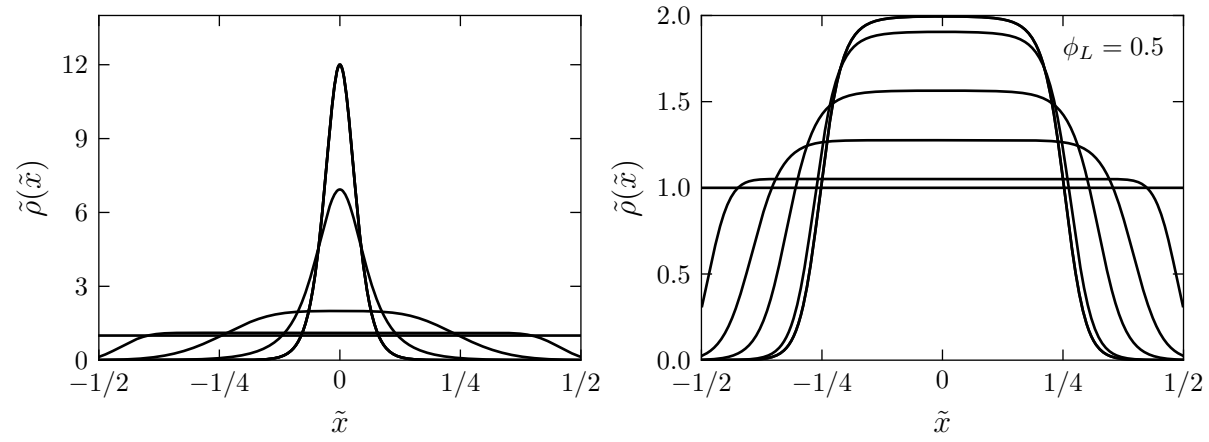

FIGURE 4.4: Comparison of the density profile evolution at $\tilde{\gamma} = 100$ without excluded volume (left) and with excluded volume with $\phi_L = 0.5$ (right). The difference becomes more dramatic at high $\tilde{\gamma}$ and ϕ_L. In the excluded volume the density at maximum packing fraction is $\tilde{\rho}_{max} = 1/\phi_L$ where the packing fraction $\phi_L = N_L\sigma/L$ with N_L as the number of particle per sheet.

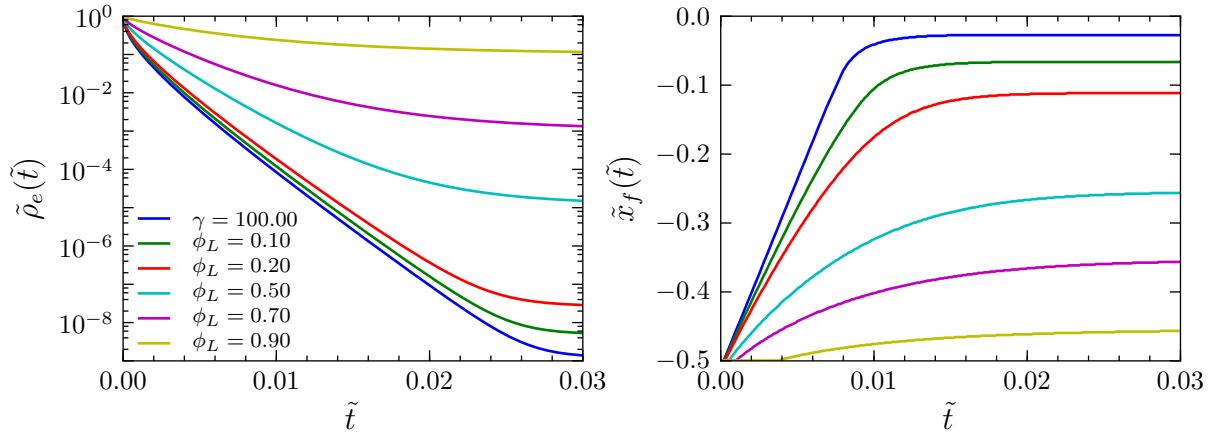

FIGURE 4.5: Dynamic depletion of the density at the system edge (left) and the position of the propagating front (right) for $\tilde{\gamma} = 100$ at increasing ϕ_L.

boundary propagating to the centre. Interestingly, there is some finite time before the bottom of the front develops positive curvature. Without excluded volume the density and temperature profiles relax to the known analytical forms given by equations (4.9) and (4.10), as shown in Figure 4.3. The propagating front becomes sharper for the excluded volume case with increasing $\tilde{\gamma}$ and ϕ_L, see Figure 4.4. With increasing γ a dense region of width ϕ_L and height $1/\phi_L$ is formed.

We can characterise the impact of excluded volume further by using the density at the edge $\tilde{\rho}_e$ as a probe of the depletion, see Figure 4.5. Without excluded volume, $\tilde{\rho}_e$ can be seen to decay exponentially with time for a relatively long period until reaching the plateau at equilibrium. Increasing ϕ_L decreases this decay time and depletion is suppressed.

We can identify the position of the front by the inflection point in the density profile curvature found at the position of the maximum in $\partial_{\tilde{x}}\tilde{\rho}(\tilde{x},\tilde{t})$. Without excluded volume the front propagates with a constant velocity until formation of a condensate at the middle. This is due to the temperature profile having a near linear section near the boundaries driving the colloids with a constant velocity $v \propto \partial_x T$. As the colloids condense into the centre the temperature profile becomes more linear, as would be expected from a point source solution of the temperature field in one dimension, sustaining the migration until the advective flux is balanced by the diffusive flux penalising the formation of the sharply peaked region. For half-coated colloids increasing η at fixed $\tilde{\gamma}$ will result in a higher diffusion coefficient, reducing the peak density of the condensate.

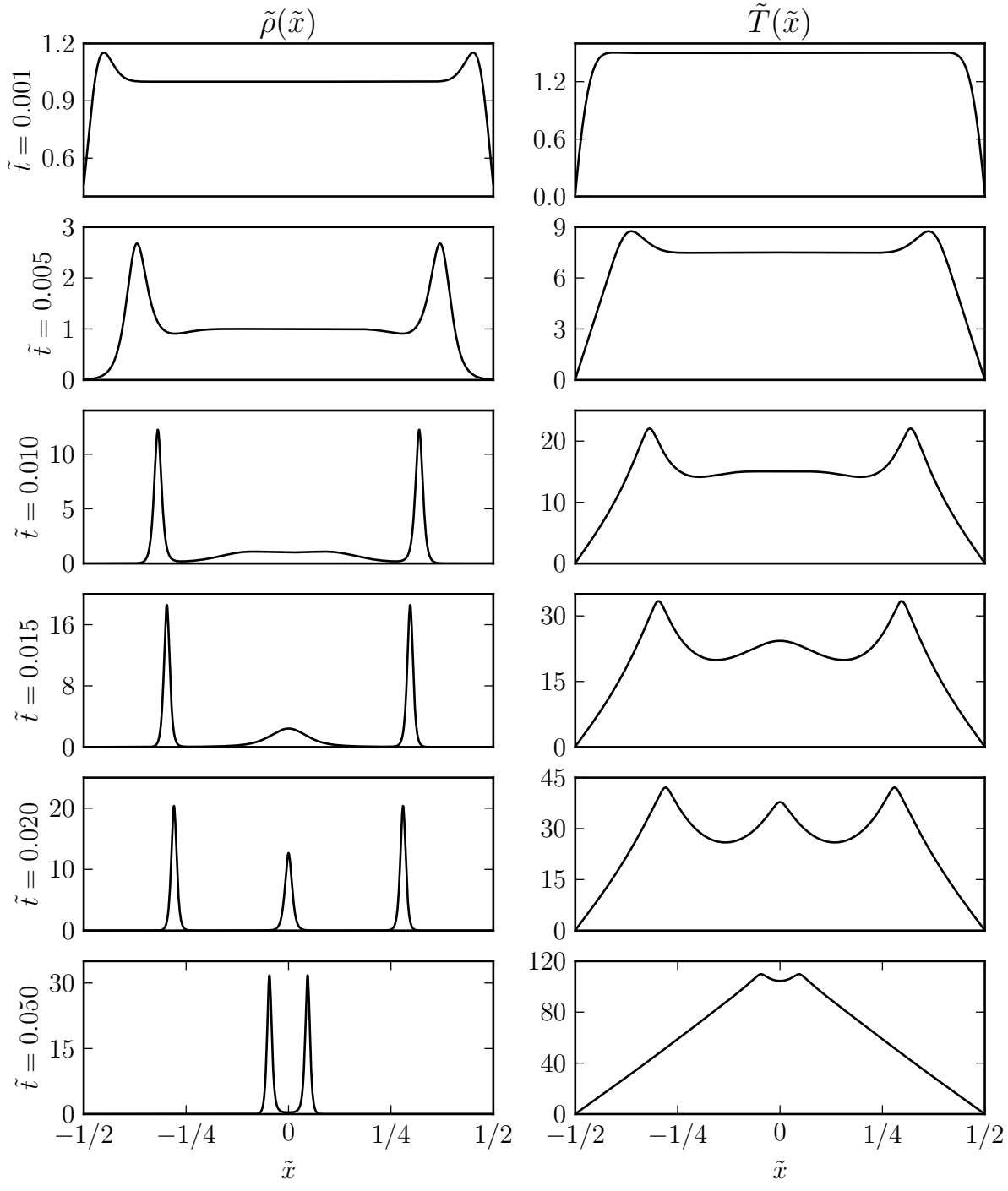

FIGURE 4.6: Snapshots of the density field $\tilde{\rho}(\tilde{x})$ (left) and temperature field $\tilde{T}(\tilde{x})$ (right) at times $\tilde{t} = 1e^{-3}, 5e^{-3}, 1e^{-2}, 1.5e^{-2}, 2e^{-2}$ and $5e^{-2}$ from top to bottom showing dynamic collapse for $\tilde{\gamma} = 1500$ and $\chi = 1$

4.3.3 Dynamic temperature field

Allowing the temperature field to be time dependent relaxes some of the constraints on its smoothness. Having looked at the limit $\chi = 0$ we now look at the other extreme $\chi = 1$. Starting with a uniform density distribution we find that the density profile can collapse into a hierarchy of peaks that ultimately merge at the centre, see Figure 4.6. At the initial stages the temperature profile has a sharp increase from the zero temperature boundary condition to the finite temperature created by the colloids acting as a heat source. This drives the colloids to accumulate slightly away from the boundary but have zero velocity elsewhere (first frame). This accumulation feeds back into the temperature field until a point when the temperature field becomes peaked such that further accumulation into the near boundary density peak is driven from both directions (second frame). The driving into the boundary peak depletes the neighbouring density towards the central region (third frame). This negative curvature then drives formation of a third peak (fourth and fifth frames), which ultimately combines with the boundary peaks (last frame).

A comparison between dynamic collapse of the density profiles at $\tilde{\gamma} = 1500$ with and without excluded volume is shown in Figure 4.7. Including excluded volume restricts the height of the peaks and as a result increases the widths. The temperature profile between the peaks with excluded volume has less curvature, and slows down the collapse. In the final frame of Figure 4.7 an asymmetry can be seen in the excluded volume boundary peak due to the steep temperature gradient between the peak and the boundary producing a sharp edge and the low curvature between the peaks allowing diffusion to smooth the corner towards the centre.

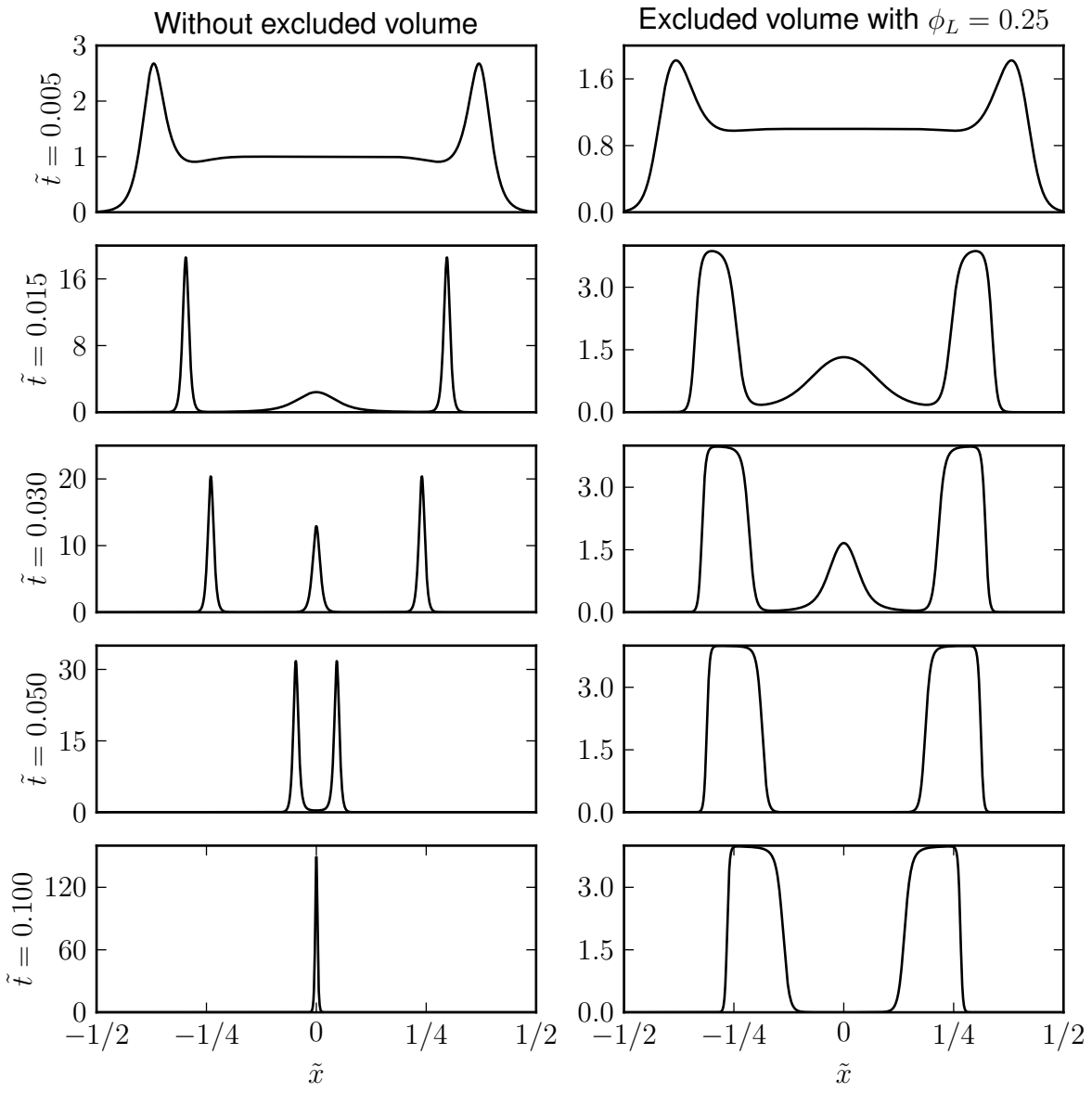

FIGURE 4.7: Snapshots of the density field without excluded volume (left) and width excluded volume with $\phi_L = 0.25$ (right) at times $\tilde{t} = 5e^{-3}, 15e^{-3}, 3e^{-2}, 5e^{-2}$ and $1e^{-1}$ from top to bottom showing dynamic collapse for $\tilde{\gamma} = 1500$ and $\chi = 1$

In order to quantify the dynamics we can look at the total absolute rate of change

$$C(\tilde{t}) = \int \left| \frac{\partial \tilde{\rho}(\tilde{x}, \tilde{t})}{\partial \tilde{t}} \right| d\tilde{x} \tag{4.19}$$

Signatures of the hierarchical collapse can be seen in Figure 4.8a) through plotting $C(\tilde{t})$ at increasing $\tilde{\gamma}$ without excluded volume. At $\tilde{\gamma} = 100$ the profile is smooth and the system

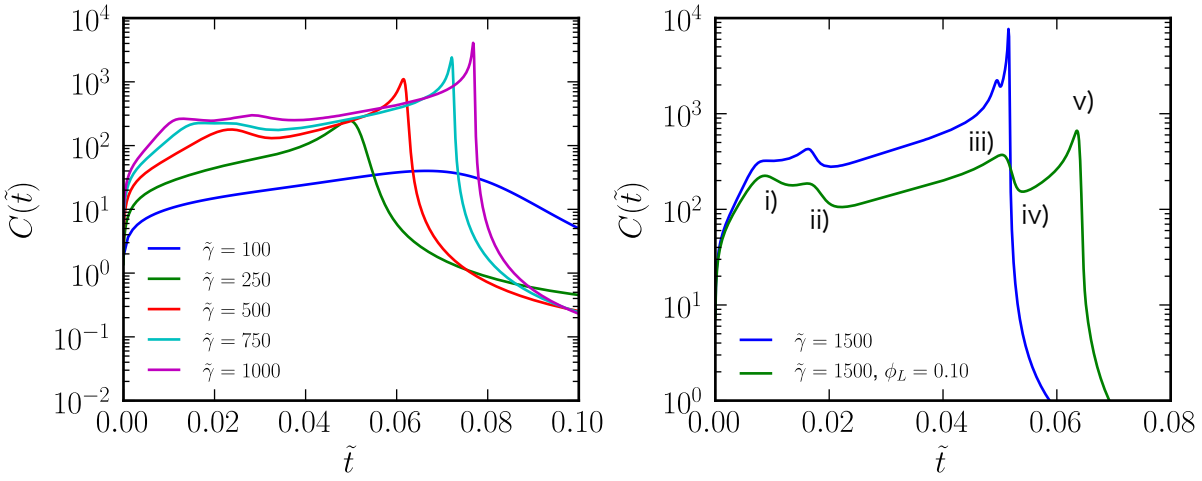

FIGURE 4.8: The total absolute rate of change $C(\tilde{t})$, as given by (4.19), is plotted for systems without excluded volume (left) and a particular case is compared with excluded volume (right) i) corresponds to the collapse into the boundary peaks ii) marks the growth of the middle peak after which the boundary peaks slowly move towards the centre until iii) when the central peak is absorbed into the outer peaks at iv) and finally the two peaks merge into the final central aggregation at v). The time unit is given by $t = L^2/D\tilde{t}$ where L is the system size and D the colloid diffusion coefficient.

slowly aggregates into the centre and relaxes. At slightly higher $\tilde{\gamma} = 250$ the collapse into the centre becomes more dynamic, indicated by a peak at late times with a sharp relaxation. At $\tilde{\gamma} = 500$ a minimum develops before the final peak. This signifies the boundary peaks have condensed, such as in Figure 4.6 (third frame). Formation of the central peak can be seen for $\tilde{\gamma} = 1000$ with appearance of another earlier minima. The time for the maximum in the final peak seems to form a minimum as a function of $\tilde{\gamma}$.

Including excluded volume slows down the final stage of the collapse, see Figure 4.8b).

4.4 Conclusions and future outook

In this chapter we have considered some of the consequences of including excluded volume in the thermoattractive collective dynamics of the thermally active colloids model

as introduced in the previous chapter. This provides a foundation to introduce further interactions between the colloids that could lead to novel active phase separation.

With zero temperature boundary conditions the colloids aggregate into the centre of the chamber. In one dimension the density of the aggregate increases linearly with $\tilde{\gamma}$ and as a result the width is inversely proportional to $\tilde{\gamma}$. For a steady temperature field without excluded volume the density at the edge depletes exponentially in time until the final stages with a density wave propagating from the boundary linearly in time. With excluded volume the exponential depletion period becomes shorter and the density front propagates sub-linearly in time.

Looking at the dynamic temperature at the limit $\chi = 1$, where both fields diffuse at the same rate, we find a hierarchical collapse of the density field into peaks beginning at the boundary. Introducing excluded volume constrains the maximum density of the peaks. Before collapse into the central aggregate the two boundary peaks were found to be asymmetric, with larger fluctuations occurring towards the centre than towards the boundary. The hierarchical collapse left signatures in the total absolute rate of change of the density field. This has revealed a useful parameter to study the process in more detail.

A future direction for this work would be to consider the impact of excluded volume in two dimensions. As mentioned in the introduction, without excluded volume these equation show 'chemotactic blowup' into a density singularity. This makes consideration of excluded volume necessary to produce physical solutions applicable to colloids.

In contrast to the one-dimensional case the width of the condensate decreases rapidly with

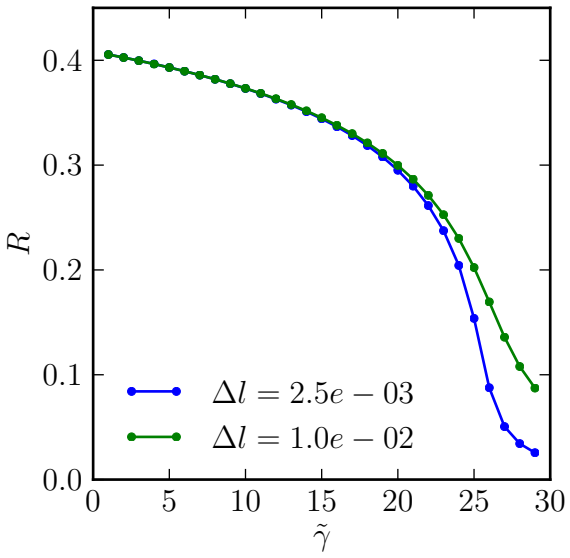

FIGURE 4.9: Characteristic width of the aggregation as a function of γ for different lattice sizes.

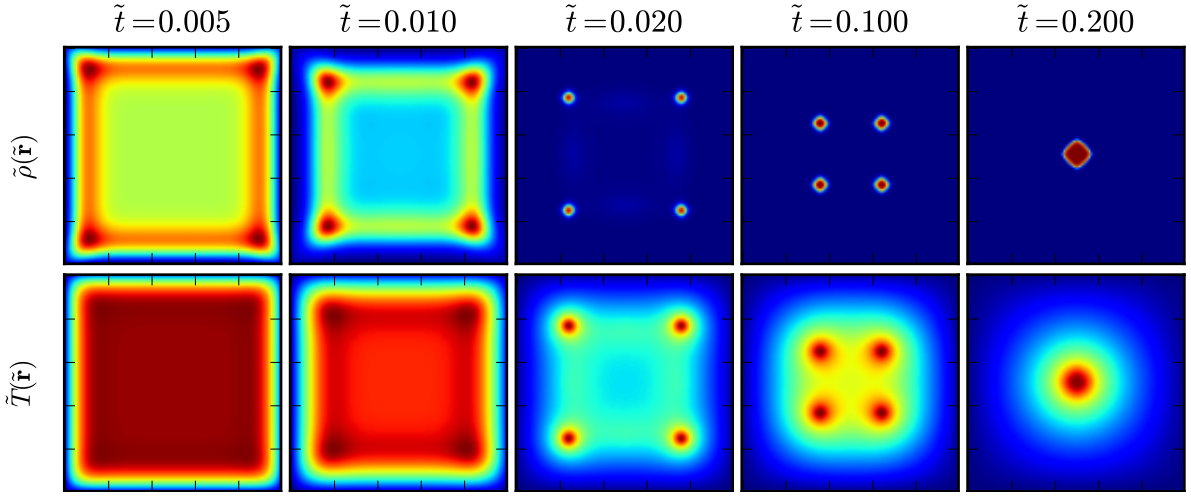

FIGURE 4.10: Collapse in two-dimensions with zero temperature boundary conditions showing the density (top) and temperature (bottom) with values increasing from blue to red for $\tilde{\gamma} = 500$ and $\chi = 1$.

increasing $\tilde{\gamma}$, see Figure 4.9. It becomes difficult to study the collapse numerically as the size of the singularity becomes comparable to the lattice spacing and acts to artificially stabilise the condensate. Figure 4.9 shows the results become dependent on the lattice size at around $\tilde{\gamma} = 15$, suggesting that an adaptive-mesh would be necessary to study the two-dimensional case without excluded volume further.

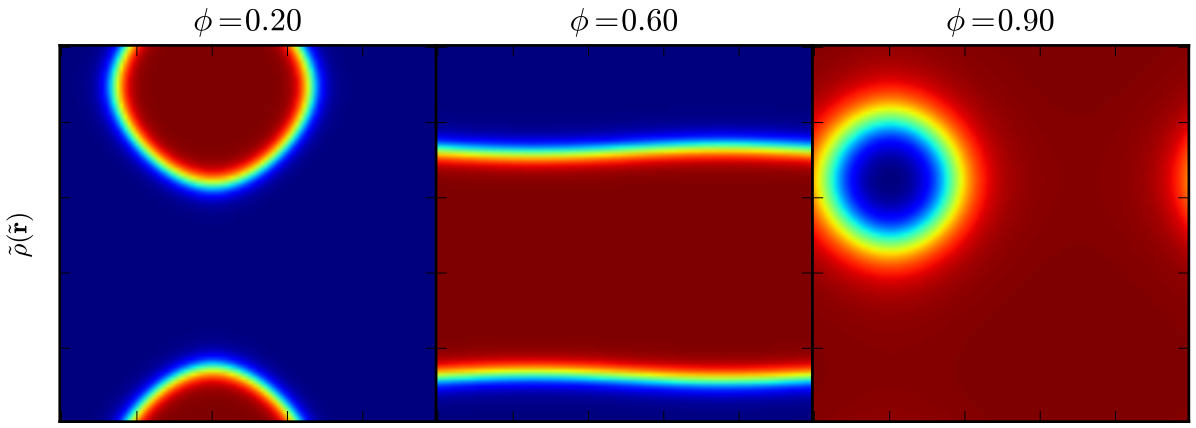

FIGURE 4.11: Three phases are observed with periodic boundary conditions, an aggregation (left), a band (middle) and a hole (right) for increasing ϕ (top).

Including excluded volume for dynamical temperature fields with $\chi = 1$ we observe collapse similar to the one-dimensional case beginning at the corners of the domain, see Figure 4.10.

We see three final phases when imposing periodic boundary conditions on the density and temperature field with excluded volume. We can solve the steady temperature Poisson equation with periodic boundary conditions using Fourier transforms. However, for uniqueness of solution it is required that there is no net flux out of the system at any time. Imposing this condition we see that a random initial density profile of colloids either forms a ball like aggregate, a band or a mostly uniform distribution with a hole at low, medium and high packing fraction, see Figure 4.11.

Chapter 5

Self-organisation and comet-like swarming

5.1 Introduction

We extend the previous investigations to the case of a collection of unconfined fully coated colloids illuminated by a directed light source with a uniform intensity distribution. The light intensity received at the surface of each colloid must take into account the interception of light by any colloids in between the subject and the source, see Figure 5.1a).

We show that in response to self and collectively generated thermal gradients the system exhibits self-organisation into a moving comet-like swarm with novel non-equilibrium dynamics, see Figure 5.1 b). Although these active colloids propel in the low Reynolds number viscous hydrodynamics regime their collective behaviour shows inertial traits. We observe propagation of transverse waves from bottom to top, ejection of hot colloids from the head and circulation of the swarm's constituents.

A particle with a clear view of the light source will have an illuminated, hot top hemisphere and a dark, cold bottom hemisphere. This asymmetric temperature distribution results

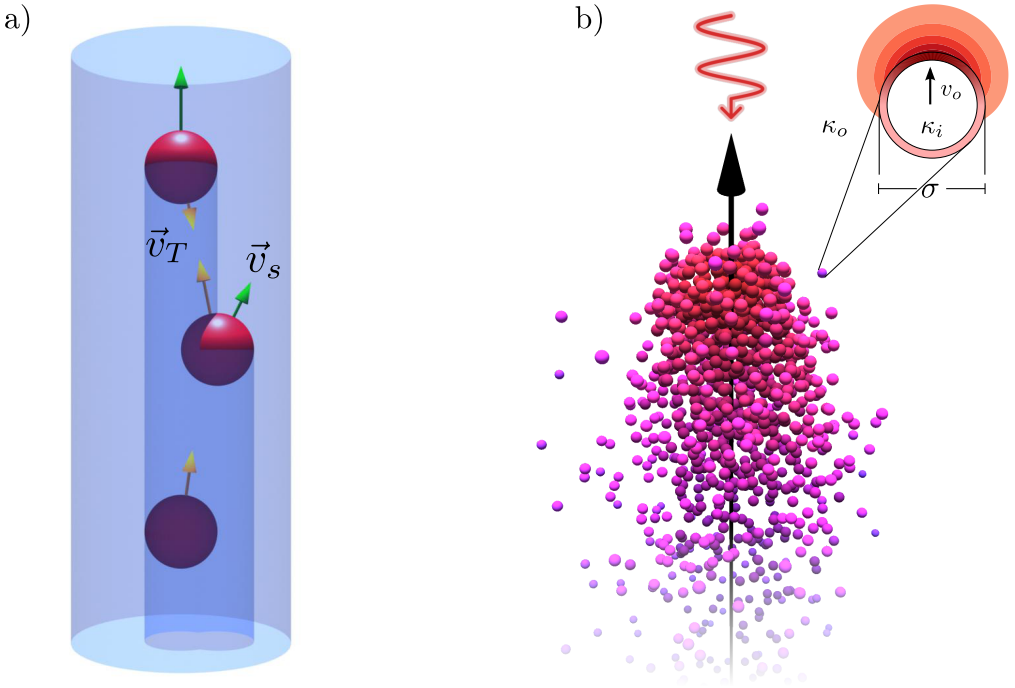

FIGURE 5.1: a) The surface intensity on each colloid is calculated taking into account obstructing colloids between the subject and the light source. The motion of the colloids is a result of the collective thermal attraction, $\vec{v}_T$, and the self propulsion driven by surface intensity distribution, $\vec{v}_s$. b) The system self-organises into a comet-like swarm that collectively moves towards the light source. Top right shows an enlarged view of an unobstructed colloid with velocity v_0, diameter σ and thermal conductivities κ_i and κ_o inside and outside the colloid.

in the colloid propelling towards the source with a maximum velocity $v_o = D_T I/(9\kappa)$ as evaluated in (3.16) with equal conductivities inside and outside the colloid.

We simulate the active colloids using coupled overdamped Langevin equations. We neglect the change in viscosity due to the heating of the water, although this is known to produce enhanced diffusion [59]. At every time step the incident intensity on the surface of each colloid is calculated, taking into account any obstructions. This is used to calculate the surface and external temperature field generated by the colloid, from which the self and collective contributions to the thermophoretic propulsion velocity are calculated and used to update the position. Collisions between particles are handled using a short range repulsive interaction.

The behaviour of the system depends on the thermal coupling strength $\eta = \sigma\epsilon I|S_T|/\kappa$ with σ the colloid diameter, I the intensity of the light source and $|S_T| = |D_T|/D$ is the magnitude of the Soret coefficient, which is the ratio of the thermophoretic mobility, D_T, to the colloid diffusion coefficient $D = k_B T/(3\pi\mu\sigma)$ where μ is the viscosity, and κ is the thermal conductivity, which is set to be equal inside and outside the colloid. By considering all other parameters to be fixed η can be controlled by the intensity of the light source. All results presented here are for simulations of $N = 1024$ colloids with η varied between 5 and 30 inclusive.

5.2 Methods

5.2.1 Surface intensity calculation

The surface intensity is sampled at discrete values of θ_i where $0 \leq \theta_i < \pi$ and ϕ_j where $0 \leq \phi_i < 2\pi$ with $i = 0, \ldots, N_\theta - 1$ and $j = 0, \ldots, N_\phi - 1$, see Figure 5.2a). This is achieved by checking whether the (x, y) coordinates of the surface sample point are contained within the projected radius of all colloids above the subject. If the sample point is not contained by any higher colloid it is assigned a surface intensity $I(\theta_i, \phi_j) = \cos(\theta_i)$ in units of I_∞ and 0 otherwise, see Figure 5.2b). This is achieved in an efficient fashion by sorting the colloid positions by z component and building a neighbour cell list.

The surface intensity expansion coefficients are calculated by

$$I_{l,m} = \int_0^\pi \sin\theta d\theta \int_0^{2\pi} d\phi\, I(\theta, \phi) Y^*_{l,m}(\theta, \phi) \tag{5.1}$$

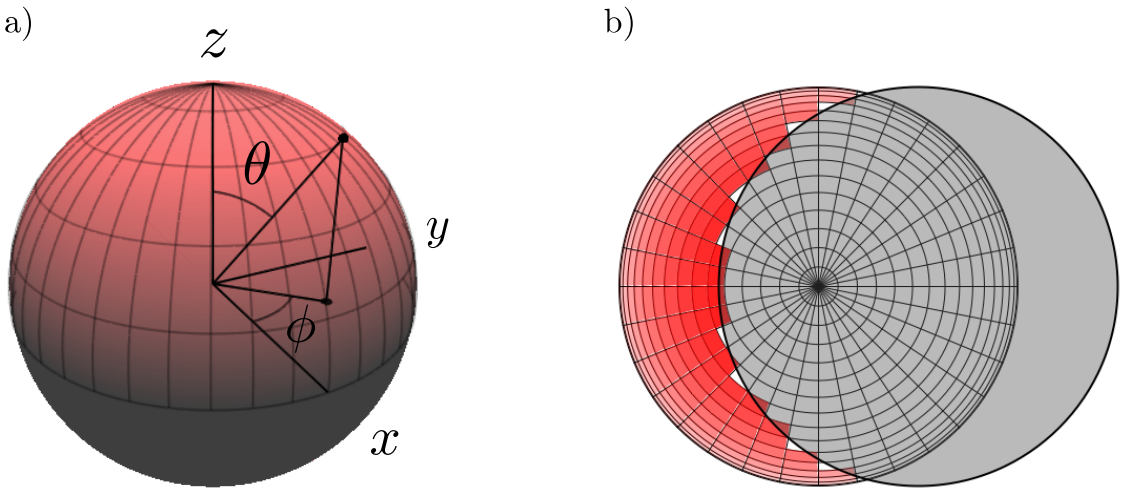

FIGURE 5.2: a) The geometry of the sphere surface discretisation b) An example of the overlap calculation viewed in the direction of light propagation, the surface panels within the shadow (grey circle) have zero intensity, the surface panels outside the shadow have an intensity weighted by $\cos\theta$

By using $Y_{l,m}(\theta,\phi) = P_{l,m}(\cos\theta)e^{im\phi}$ where $P_{l,m}$ are the normalised associated Legendre functions we can write

$$I_{l,m} = \int_0^{\pi} \sin\theta d\theta \hat{I}(\theta,m) P_{l,m}(\cos\theta) \tag{5.2}$$

where the integral over ϕ has been written as a transformation to m

$$\hat{I}(\theta,m) = \int_0^{2\pi} d\phi\, I(\theta,\phi) e^{-im\phi} \tag{5.3}$$

This allows the transformation to be approximately integrated as

$$\hat{I}(\theta_i,m) \sim \frac{2\pi}{N_\phi} \sum_{j=0}^{N_\phi-1} I\left(\theta_i,\phi_j\right) e^{-im\phi_j} \tag{5.4}$$

spacing ϕ linearly, $\phi_i = 2\pi i/N_\phi$, this can be performed efficiently using a fast Fourier

transform. The integral over θ is performed using Gauss-Legendre quadrature. We use $x = \cos\theta$ as the integration variable such that $dx = -\sin\theta d\theta$ and

$$I_{l,m} = -\sum_{i=0}^{N_g-1} \hat{I}(\theta_i, m) P_{l,m}(x_i^{(N_g)}) w_i^{(N_g)} \tag{5.5}$$

where $\theta_i = \cos^{-1}(x_i^{(N_g)})$ and N_g Gauss-Legendre nodes, $x_i^{(N_g)}$, are used with weights $w_i^{(N_g)}$. We set $N_g = N_\theta$ and $N_\phi = 2N_\theta$. For the simulations presented here we use $N_\theta = 32$. For further information on numerical calculation of spherical harmonic expansion coefficients consult references [60, 61].

5.2.2 Langevin equations

Colloid positions are integrated through an overdamped Langevin equation scheme where positions from time step n to $n+1$ are updated by $\mathbf{r}^{(n+1)} = \mathbf{r}^{(n)} + d\mathbf{r}$, where $d\mathbf{r} = \mathbf{v}\Delta t + \xi\sqrt{2\Delta t}$ uses units σ and σ^2/D for distance and time respectively. Random fluctuations are included through the white noise term ξ with $\langle\xi(t)\rangle = 0$ and $\langle\xi(t)\xi(t')\rangle = \delta(t-t')$. The particle velocity consists of three parts $\mathbf{v} = \mathbf{v}_s + \mathbf{v}_T + \mathbf{v}_{\text{ex}}$ where $\mathbf{v}_s$, $\mathbf{v}_T$ and $\mathbf{v}_{\text{ex}}$ are the self-propulsion, collective thermal drift and excluded volume contributions. The colloid self-propulsion velocity is given by (2.27) rewritten here in dimensionless parameters

$$\mathbf{v}_s = \frac{\eta}{3} \frac{\left[\sqrt{2}\left(-\text{Re}\left\{I_{1,1}\right\}\hat{\mathbf{x}} + \text{Im}\left\{I_{1,1}\right\}\hat{\mathbf{y}}\right) + I_{1,0}\hat{\mathbf{z}}\right]}{\sqrt{3\pi}} \tag{5.6}$$

where $I_{l,m}$ is the spherical harmonic expansion coefficient of degree l and order m of the discretised surface light intensity, $I(\theta_i, \phi_j)$, incident on the colloid, where θ_i and ϕ_j are the discrete polar and azimuthal angles in spherical coordinates. The collective drift velocity

is

$$\mathbf{v}_{T,i} = \frac{\eta}{8\sqrt{\pi}} \sum_{j=1}^{N} \frac{I_{0,0}^{(j)}}{|\mathbf{r}_j - \mathbf{r}_i|^2} \hat{\mathbf{r}}_{ij} \tag{5.7}$$

where i and j are particle indices and $\hat{\mathbf{r}}_{ij} = (\mathbf{r}_j - \mathbf{r}_i)/|\mathbf{r}_j - \mathbf{r}_i|$ is the unit vector along the centre line of the two particles. The excluded volume component takes the Lennard-Jones form $\mathbf{v}_{\text{ex}} = 24(2r^{-13} - r^{-7})\hat{\mathbf{r}}_{ij}$ for $r < 2^{1/6}$ and zero otherwise. Excluded volume and surface light intensity are calculated through the use of neighbour lists and integration is performed with an adaptive time step that constrains the maximum displacement to be less than $\sigma/100$ on average over the last 100 steps.

5.3 Results

5.3.1 Swarm formation

The simulations begin with the particles randomly arranged inside a cube of side length 20σ with the directed light source oriented down the z axis. Illuminated colloids in the top section of the cube become heated by the absorption of light. Some colloids will be partially illuminated due to obstruction by colloids between the subject and the source and emit a lower heat flux. All illuminated particles will feel a locally generated propulsion along the z axis towards the light source with a velocity proportional to η and the illumination coverage with a potential maximum value of v_o. Partially illuminated colloids will also experience propulsion in the xy plane due to the asymmetric heat distribution in the polar azimuth angle resulting in the lower of two colloids overlapping in the xy

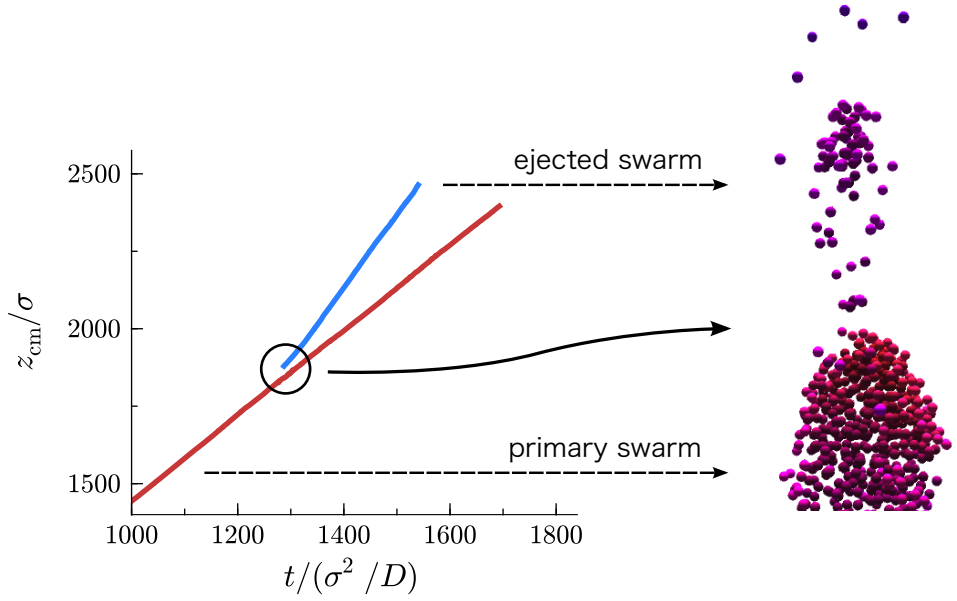

FIGURE 5.3: The swarms move with a velocity dependent on the number of particles in the swarm due to thermal drag. Fluctuations in the swarm shape facilitates ejection of hot colloids at the swarm tip forming faster moving sub swarms.

plane to move away from the connecting centre line, contrary to the motion of thermal attraction, see equation (5.6). All colloids, whether illuminated or not, can have a velocity component from the thermal gradients in the collective temperature field generated by the illuminated colloids, $\mathbf{v}_T = -D_T \nabla T$, driving aggregation to regions of higher temperature. For the values of η presented here this leads to formation of a high density head region with the outer most illuminated colloids generating a central hot core. This high density head blocks the light for all colloids below it, essentially casting a shadow. The combination of the self-propelled illuminated head and attraction to the core leads to a swarm that is collectively moving towards the light source. After an initial transient organisation period the swarm's centre of mass position in the z direction increases linearly with time giving rise to a constant swarm velocity, $V_{\rm swarm}$, see Figure 5.3.

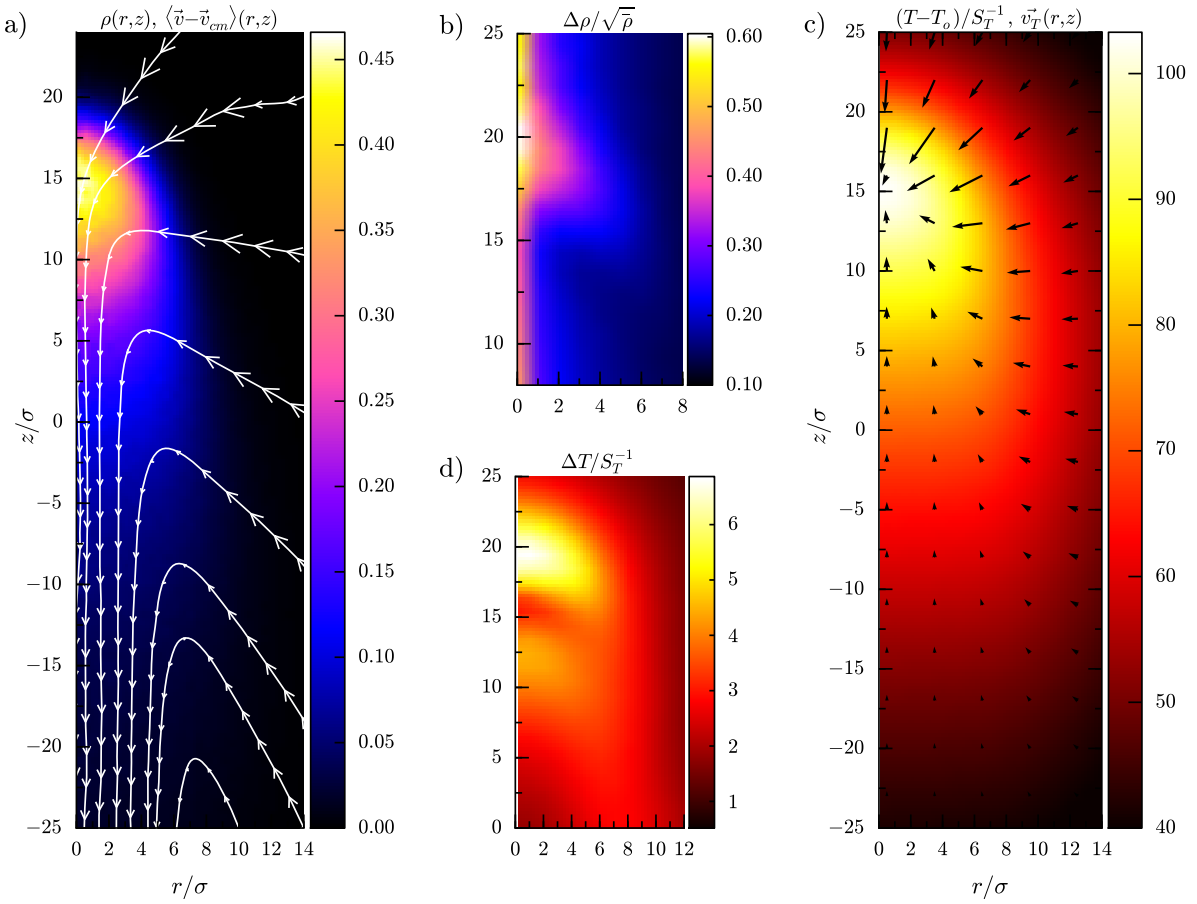

FIGURE 5.4: Using the moving centre of mass swarm frame of reference fields can be reconstructed using time and ensemble averaging. The swarm fields are axially averaged and presented in cylindrical coordinates (r, z) with z axis pointing towards the light source and r the radial distance. a) Density field and average colloid velocity relative to centre of mass velocity. The relative colloid velocity is represented by the size of the arrows placed along the streamlines. b) Density fluctuation field normalised by equilibrium fluctuations. c) Temperature field with phoretic velocity due to temperature gradients. d) Temperature fluctuation field.

5.3.2 Structure and circulation

We use a connectivity based clustering algorithm with a euclidean distance metric to define which particles belong to the swarm. We find the set of connected particles where no particle is greater than a distance s from another member of the set. We define the swarm to be the connected set with the largest number of members. We use the arbitrary value of $s = 5\sigma$ for the swarm separation in the results presented here.

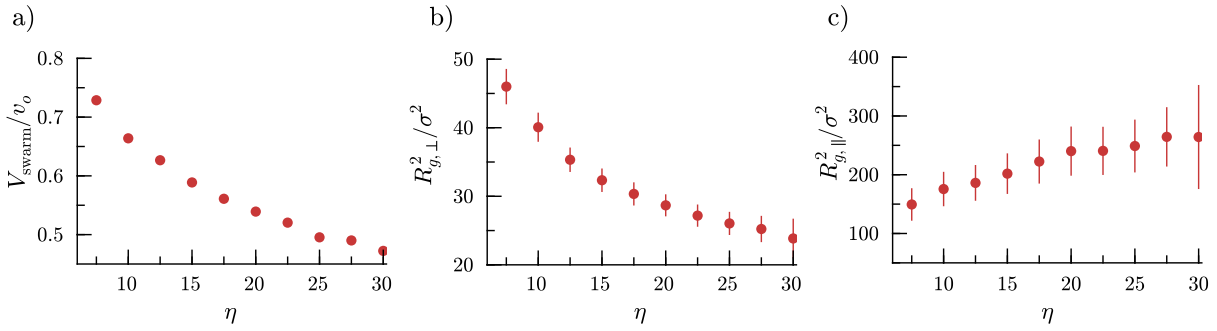

FIGURE 5.5: a) Swarm velocity normalised to fastest colloid velocity. b) Radius of gyration of the swarm in a direction perpendicular to the axis of illumination and radius of gyration parallel c) with error bars showing standard deviation over an ensemble average of 10 simulations.

By using the centre of mass of the swarm as a moving frame of reference we can reconstruct the time and ensemble average density and temperature fields. The axially averaged versions of these fields are presented in Figure 5.4 along with their fluctuations. The high density head region and hot core can be clearly seen in Figure 5.4a) and c). The fluctuations of the density field have been normalised by the equilibrium expectation in Figure 5.4b) such that any deviation of this field away from a constant value indicates non-equilibrium density fluctuations. These density fluctuations are seen to occur at the very tip of the head region as a result of illuminated self-propelled particles attempting to escape the influence of the thermal attraction, as shown by the vector field in Figure 5.4c), during fluctuations of the swarm shape. These particles usually return to the swarm, however spectacular ejection events have been observed at the tip with likelihood increasing with η, see Figure 5.3. Density fluctuations at the swarm tip lead to large and unusual temperature fluctuations due to the transient appearance of heat sources as shown in Figure 5.4d).

The thermally induced drift velocity towards the core shown in the vector field of Figure 5.4c) competes against the propulsion towards the light source of the illuminated head

particles producing a 'thermal drag' that leads to a sub linear dependence of the swarm velocity, V_{swarm}, on η, see Figure 5.5a). This leads to a novel effect as particles outside of the swarm move faster than inside the swarm. A particle in the shadowed tail of the swarm, where the thermal attraction of the core is not great enough to keep the particle within the bulk of the swarm, may be left behind. At some point this inactive colloid will diffuse out of the shadow to become active again and propel towards the source. As it moves faster individually than in the swarm it may catch up and find itself attracted back to the hot core creating a circulation of particles. Alternatively, the colloid may escape the influence of thermal attraction and propel past the swarm no longer to feel its influence. The reconstructed average colloid velocity streamlines relative to the swarm centre of mass frame, $\vec{v}_{cm}$. Figure 5.4a) shows that colloids attracted to the hot core reverse their direction on crossing the shadow boundary.

The average shape of the swarm is affected by the value of η and can be measured quantitatively by using shape descriptors derived from the eigenvalues $\lambda_1^2 < \lambda_2^2 < \lambda_3^2$ of the radius of gyration tensor $R_{\alpha,\beta} = N^{-1}\sum_{i=1}^{N} \mathbf{d}_{i,\alpha}\mathbf{d}_{i,\beta}$, where $\mathbf{d} = \mathbf{r}_i - \bar{\mathbf{r}}$, $\mathbf{r}_i$ is the colloid position, $\bar{\mathbf{r}}$ is the average position of the set, i is a particle index and α and β are cartesian coordinate indices. The eigenvalues can be combined to define the perpendicular radius of gyration $R_{g,\perp} = \sqrt{\lambda_1^2 + \lambda_2^2}$, and the parallel radius of gyration $R_{\parallel} = \sqrt{\lambda_3^2}$. The radius of gyration perpendicular to the axis of illumination correlates to the size of the shadow cast by the swarm. This becomes smaller as η is increased as shown in Figure 5.5b). The swarm also becomes longer with increasing η resulting in an increased aspect ratio as shown in the parallel radius of gyration in Figure 5.5c).

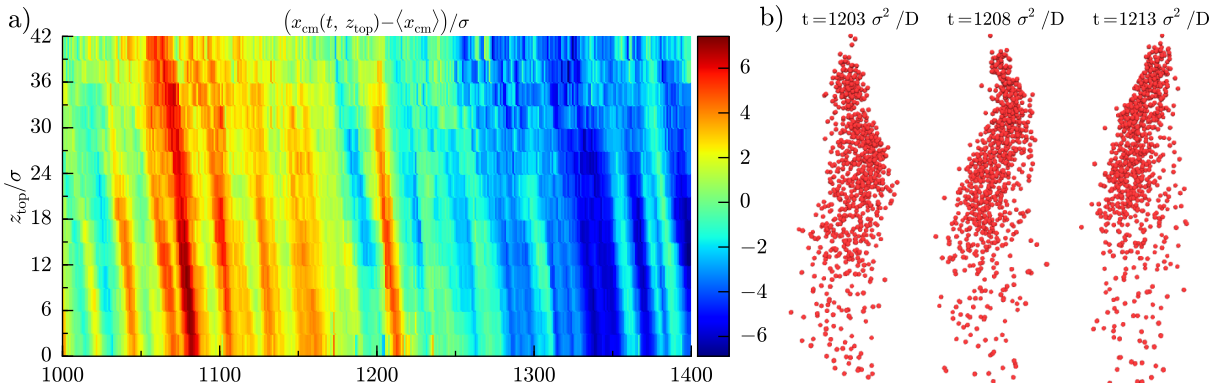

FIGURE 5.6: a) Kymograph of centre of mass x location for section thickness $\Delta z = 3\sigma$ a distance z_{top} from the swarm top at time t for $\eta = 25$. Colour represents the x value of the centre of mass around the time average within the displayed window. b) Snapshots of swarm conformation at three successive times as shown by the kymograph in a) displaying wave propagation from bottom to top.

5.3.3 Wave propagation

The swarm exhibits waves of colloids displaced from the central axis in a randomly selected azimuthal direction propagating from tail to head with pronunciation increasing with η. These undulations arise from tail colloids diffusing out of the shadow, aided by the effect of partial illumination when crossing the shadow boundary driving their motion away from the swarm. The colloids then become thermally active and attract colloids above them out of the shadow further propagating the wave along the swarm length. The wave can be observed by partitioning the swarm along the z-axis into sections of Δz moving down from the top of the swarm and recording the centre of mass position in x or y as a function of time in each section. This produces a three dimensional kymograph as displayed in Figure 5.6, with connected lines of colour representing propagation of an in-plane centre of mass displacement up the swarm. The rate of this propagation is seen to increase with η.

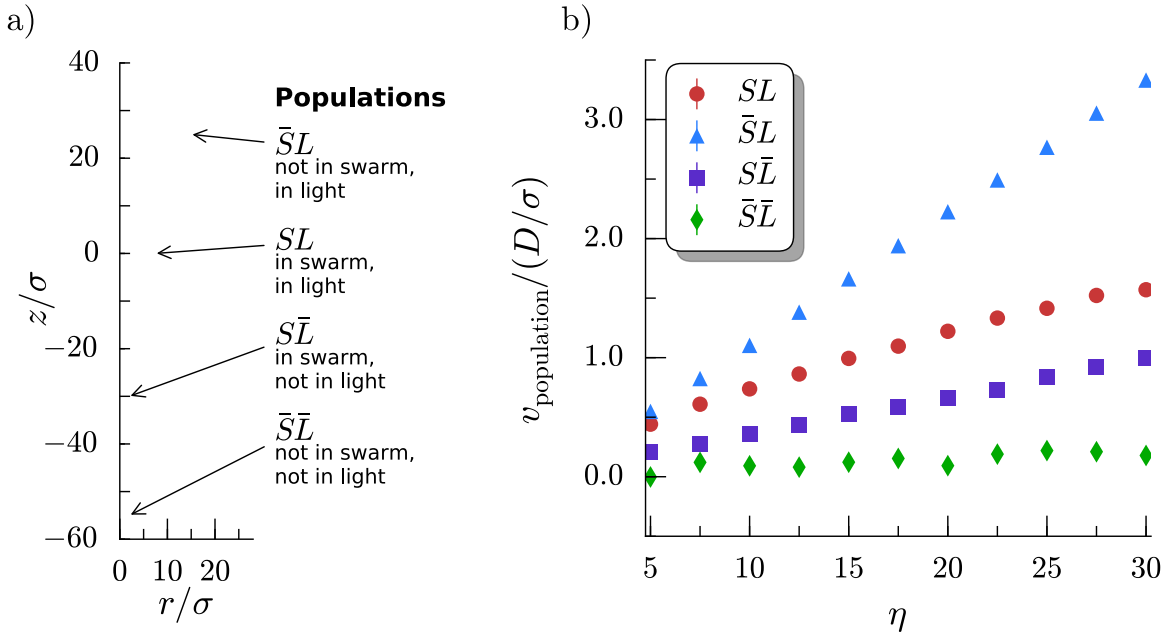

FIGURE 5.7: a) Spatial reconstruction of the most probable population at each location in the moving swarm frame of reference with a description of the two letter population type notation. b) Average colloid velocity within each population as a function of η.

5.3.4 Population analysis

The colloid behaviour is dependent on whether it is illuminated or not, L or $\bar{L}$ respectively, and whether it is in the swarm or not, S or $\bar{S}$ respectively. We can define four distinct populations that the colloid can belong to at any instant of time from these possibilities: SL, $S\bar{L}$, $\bar{S}L$ or $\bar{S}\bar{L}$. SL colloids self-propel and cooperate to generate the heated core of the swarm whilst constituting the largest fraction of in-swarm particles while $S\bar{L}$ form the core of the swarm and are influenced only by thermal gradients. $\bar{S}L$ colloids have typically propelled past the swarm and $\bar{S}\bar{L}$ colloids have fallen behind the swarm, yet remain in the shadow soon to diffuse out into $\bar{S}L$ and possibly rejoin SL or $S\bar{L}$. The spatial location of these populations can be reconstructed in the moving swarm frame of reference by plotting the most probable population at each location, see Figure 5.7a). The velocities of the populations vary differently with η. Active colloids outside the swarm $\bar{S}L$ show the

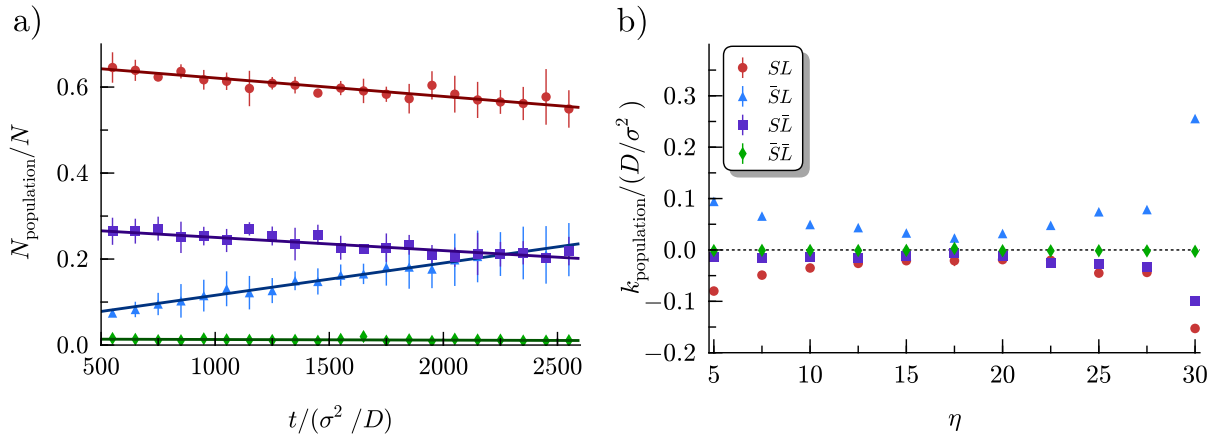

FIGURE 5.8: a) size of population normalised to number of particles in the system as a function of time for $\eta = 10$, error bars show standard deviation over ensemble averaging of 10 simulation. b) The rate of change of population sizes as a function of η as obtained from fitting population numbers as in a), horizontal dotted line marks $k = 0$.

linear increase with η while the velocities of colloids inside the swarm increase at a slower rate. This creates larger differences in the velocities between the populations at higher η increasing the likelihood of fission of the swarm into sub-swarms, as demonstrated in Figure 5.3.

The number of $\bar{S}\bar{L}$ colloids is generally very small and stays almost constant in time while the number of in-swarm colloids, $SL + S\bar{L}$, are decreasing in time with the majority permanently passing to $\bar{S}L$, see Figure 5.8a). The rate of change of these populations is dependent on η with a turning point seen at $\eta \sim 17.5$. Values of η greater than this turning point represent an increasingly unstable swarm. It is interesting to note that $k_{S\bar{L}}$ remains constant until the turning point and then begins to follow the trend of k_{SL} colloids, see Figure 5.8b).

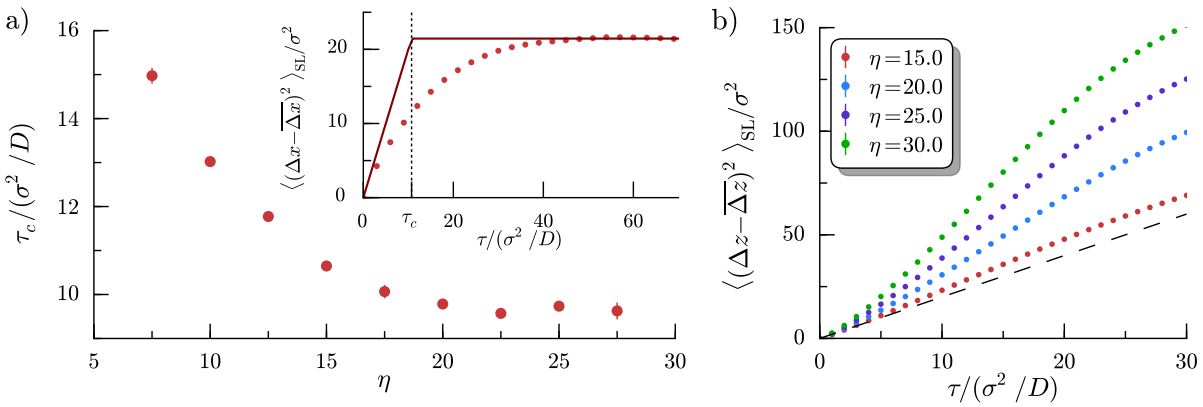

FIGURE 5.9: a) Confinement time as a function of η for SL particles in the x direction, inset shows confinement time calculation for $\eta = 25$. b) Mean squared displacement for SL particles in the z direction for multiple η values, dashed black line shows standard $\langle \Delta z^2 \rangle = 2D\tau$ diffusion.

5.3.5 Population diffusivities

Analysis of the population dependent statistical dynamics can be performed by tracking colloid trajectories within the distinct populations. The time dependence of the mean squared displacement (MSD) reveals information on the fluctuations of the particle position around the mean.

The MSDs presented are calculated from trajectories recorded within the SL population. All displacements of a given time difference $\tau_i = i\Delta t$ along the length of each trajectory and over multiple ensembles are used to calculate the mean displacement $\overline{\Delta x}(\tau_i) = n^{-1}\sum_j^n \Delta x_j(\tau_i)$ and the mean of the square displacement $\overline{\Delta x^2}(\tau_i) = n^{-1}\sum_j^n \Delta x_j^2(\tau_i)$ in order to calculate the variance $\langle(\Delta x(\tau_i) - \overline{\Delta x}(\tau_i))^2\rangle = \overline{\Delta x}^2(\tau_i) - \overline{\Delta x^2}(\tau_i)$, where n is the number of displacements recorded.

Standard diffusion is observed for all populations of particles external to the swarm, however within the swarm the colloid becomes confined by the thermal attraction leading to a plateau in the MSD at long times. A confinement time can be measured by finding

the crossover time between standard diffusion at short times and a constant MSD at long times, see Figure 5.9a) for the confinement time in the x direction for SL colloids as a function of η and inset for visualisation of the method use to determine crossover time. The confinement time decreases with η until the turning point, above which it becomes almost constant. This correlates with the response of the radius of gyration perpendicular to the axis of illumination shown in Figure 5.5b). For the MSD of SL particles in z direction we observe enhanced diffusion with a coefficient increasing with η. The response of the MSD shows standard diffusion at short times but crosses to enhanced diffusion at intermediate times, see Figure 5.9b). At long times the MSD plateaus due to confinement in the swarm, however, as the swarm elongates with η the confinement size does not plateau in η as shown in Figure 5.9a).

5.4 Conclusions and future outlook

Here we have considered non-scattering colloids in the regime of geometric optics, however, we expect many of the features of the results presented here to remain for scattering particles. Any sample of light absorbing colloids illuminated with a directed light source will experience a temperature gradient along the illumination axis providing the necessary conditions for self-organisation and collective propulsion. Dimensional values for this system can be estimated by considering coated polystyrene colloids with thermal conductivity $\kappa_{PS} = 0.033\,\mathrm{W/(m \cdot K)}$, diameter $\sigma = 1\,\mu\mathrm{m}$, Soret coefficient $|S_T| = 10\,\mathrm{K}^{-1}$ and absorption efficiency $\epsilon \sim 1$ irradiated by a monochromatic defocused laser beam over an area of $A = 1\,\mathrm{mm}^2$ to yield a laser power related to η of $P \sim 1\eta\,\mathrm{mW}$. The quoted

Soret coefficient corresponds to temperature variations smaller than 20 K for the highest η presented here. The diffusion coefficient for a single colloid in water around room temperature, $D \sim 1\,\mu\mathrm{m}^2\mathrm{s}^{-1}$, sets the maximum colloid velocity to $v_o \sim 0.01\eta\,\mu\mathrm{m}/s$.

We have described an active colloid system that displays a wide range of interesting non-equilibrium features including self-organisation, circulation, density and temperature fluctuations, wave propagation, swarm fission, time dependent population dynamics and enhanced diffusion. This work demonstrates the possibility of engineering emergent behaviour from basic physical principles.

Future directions of this work include incorporating near-field boundary effects in the temperature and hydrodynamic calculations, allowing different patterns of the surface coating and considering light scattering by the colloids. We have exclusively considered the case of thermoattraction caused by a negative Soret coefficient, however, the more common thermorepulsive case may show long range correlations due to these colloids favouring the shadows cast by others. A similar system of chemically active colloids could be studied, but in this case how the 'fuel' is depleted and replenished must be considered carefully. Including other short-range potentials could also vastly change the dynamic nature of the aggregate.

Active colloids have great potential in the study of complex non-equilibrium systems. The self-organisation present in biological systems can only be emulated through developing strong theoretical foundations and by constructing synthetic systems to test, explore and demonstrate the possibilities for active matter.

Part II

Polymer Translocation

Chapter 6

Introduction

Understanding the physics of the nanoscale promises a new level of inspection and control of molecules. This is becoming increasingly relevant as the frontiers of knowledge in biology and medicine approach the molecular scale. Next generation DNA sequencing is one future technology that is set to have an immediate impact on diagnosis and soon molecular based medicine and medical diagnostics will be a common occurrence.

We consider the passage of a linear polymer through a pore within a membrane, known as *polymer translocation*, and investigate the statistical dynamics of this process. In Chapter 7 we consider the effect of pore patterning on homopolymer and block co-polymer translocation and describe a stochastic sensing protocol capable of identifying a target molecule within a collection of known candidates. In Chapter 8 we consider the passage of a homopolymer through a pore that is changing geometrically in time and present and compare analysis of translocation through time dependent environments.

This chapter intends to outline the background of polymer translocation and introduce a coarse grained model used in the numerical investigations presented in the following chapters.

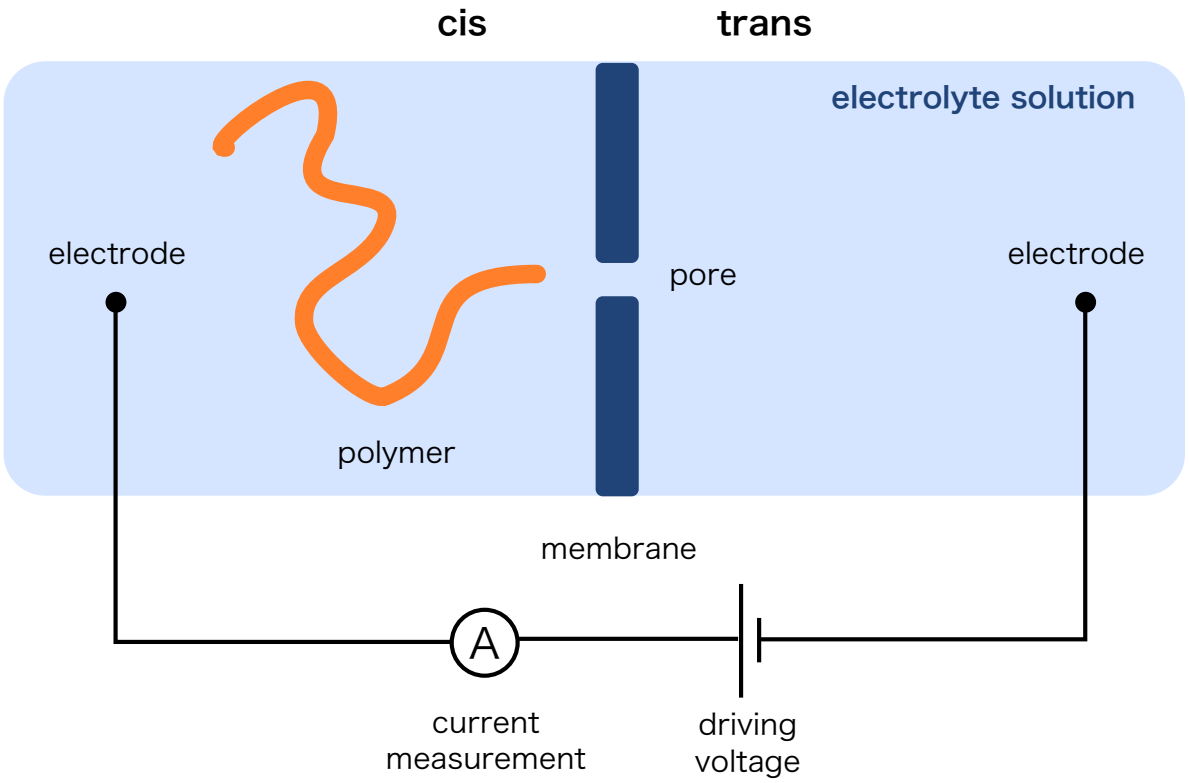

FIGURE 6.1: Schematic representation of a generic current-blockade polymer translocation experiment. Two electrodes placed in an electrolyte solution are used to apply a voltage across a membrane. An ion current flows through the pore unless blocked by a polymer. Measurement of the duration of a reduction in the ion current allows determination of the translocation time.

6.1 Experiments

A generic current-blockade polymer translocation experiment is represented schematically in Figure 6.1. Two regions of an electrolyte solution are separated by a membrane and connected through a single pore. Application of an electric field across the membrane leads to a flow of ions with a conductivity that is proportional to the free volume within the pore. An object entering the pore can be detected by a reduction in the measured current. In order to detect a single molecule the cross-sectional area of the pore must be comparable to the polymer. The width of single stranded DNA (ssDNA) is approximately 1 nm requiring nano scale pores (nanopores).

Rough estimates for force scales and current magnitudes can be made from simple arguments. A voltage drop, V, across the pore gives rise to the force $F = qV/L$ on each monomer where q is the effective charge per monomer and L is the pore length. Order of magnitude estimates of $q = 1e$, $V = 100\,\mathrm{mV}$ and $L = 1\,\mathrm{nm}$ give a force $F \sim k_bT/L \sim 10\,\mathrm{pN}$. The current can be estimated from $J = znv$, where z is the ionic charge, n is the charge number density and v is the drift velocity with typical salt concentrations of 1 M and a velocity $v = F/\zeta = zE/(6\pi\eta a) = zV/(6\pi\eta aL)$ where the friction coefficient $\zeta = 6\pi\eta a$ is given by Stoke's drag for a sphere with ionic radius $a \sim 1\,\text{Å}$, giving typical ionic currents of 10 pA, which are readily measured by electrophysiological methods. At this scale ions act as probes for the pore contents, leaving signatures in the current measurement time series.

The suggestion of nanopore based DNA sequencing was made early on in the literature along with the following requirements for a successful device [62]:

- only a single base or very few bases should be within the pore at any time
- bases must be distinguishable in the ion-current measurement
- the sample time is much faster than single base translocation
- each base moves through the pore sequentially

These challenges have been addressed [63] and overcome with the first commercial nanopore based DNA sequencing device announced in 2012 (Oxford Nanopore Technologies, Oxford, UK) [64]. Besides sequencing, nanopores offer great potential for sorting and detection of a wide range of molecules.

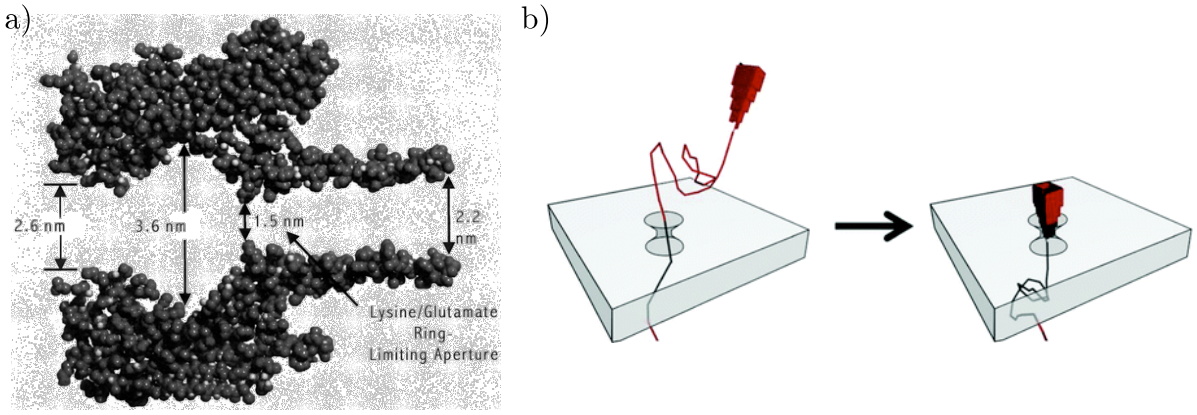

FIGURE 6.2: a) Atomistic structure of αHL. Reprinted with permission from D. W. Deamer and D. Branton, Acc. Chem. Res., 35, 10, 817-825, 2002. Copyright 2002 American Chemical Society. b) Schematic of the DNA origami pore insertion into a solid state pore. Reprinted with permission from N. A. W. Bell *et al.*, Nano Lett., 12, 1, 512-517, 2012. Copyright 2012 American Chemical Society.

As an aside, the method of using ion flow current measurements to detect objects moving through holes goes back to Coulter (1957) [65], and is known as the Coulter principle. This principle has long been employed commercially in blood cell counting and in characterisation of other suspended particles.

Polymer translocation experiments have progressed from the use of biological pores to solid state synthetic pores and to a hybrid combination of biological and synthetic pores. In the following sections we will highlight a few experimental developments followed by progress in theory and simulation. We will conclude this chapter with a description of the polymer translocation model to be used in the following two chapters.

6.1.1 Biological pores

Initial DNA translocation experiments by Kasianowicz *et al.* (1996) [62] made use of the biological pore α-hemolysin (αHL), which is secreted by the bacterium Staphylococcus

Aureus as a toxin. The secreted proteins self assemble into a pore across lipid membrane bilayers. The biological function of this pore is to puncture the membrane of a prey bacterium such that S. Aureus can consume the nutrients through lysis. This self assembly mechanism is utilised to insert the pore across an artificial lipid bilayer formed between a Teflon coated support. αHL has a mushroom like geometry with the 'cap' of the mushroom housing a chamber, known as the vestibule, leading to the 'stork', known as the barrel, see Figure 6.2a). The vestibule and the barrel are separated by a narrow constriction of diameter $\sim 1.5\,\mathrm{nm}$ making it attractive for sequencing purposes.

DNA was found to translocate through the pore at speeds of $1\,\mathrm{base}\,\mu\mathrm{s}^{-1}$ under a driving voltage of $100\,\mathrm{mV}$. This high speed raised questions on the ability to distinguish the sequence dependent modulations in the current against ionic noise at typical measurement rates of $\sim 10\,\mathrm{kHz}$ [66]. This suggested that translocation needed to be slowed down in order to gain accurate readings.

Two peaks were observed in the translocation time distribution, one at later times with a broader width revealing that ssDNA exhibited orientation dependence with a $5'$ entry translocating slower than $3'$. Kasianowicz *et al.* (2000) [67] later showed that polymer translocation is much more likely to occur from the cis side rather than the trans side. This is attributed to the large vestibule on the cis side of αHL having a positively charged entrance and an entropically more favourable geometry as compared to the negatively charged exit on the trans side with the more restrictive barrel geometry. Meller *et al.* (2001) [68] found that the translocation velocity scales quadratically with voltage and is faster and nonlinear for ssDNA strands of less than 20 bases and is independent of length above this. Subsequent experiments by Meller, Deamer and Branton have shown that the

mean translocation time increases linearly with polymer length for αHL, however, these results are only given for strands of less than 500 bases long [62, 69, 70]. Claims for the scaling behaviour of polymer translocation has caused some controversy and will be a recurring theme in this introduction.

Biological pores have the advantage of atomistic accuracy in their structure with the ability of modification by genetic engineering. Experimentalists from the Bayley group, have engineered αHL by site specific mutations in order to increase its performance [71]. Biological pores can also be adapted by the addition of other functional proteins. One proposed method of sequencing involved the addition of exonuclease to the cis side of αHL in order to cleave bases from ssDNA to be subsequently passed through the pore for identification, one by one [72]. This is a fantastic demonstration of the possibilities of biotechnology.

6.1.2 Synthetic pores

Artificial nanopores have been fabricated in solid state wafers. This is a desirable platform for nanopore technology as wafers are mechanically more stable than lipid membranes and allow a greater level of control over pore size, number and configuration. However, precise control over nanoscale artefacts is a technological challenge [73]. Membranes of Si, SiN or SiO_2 are typically used as they are well understood from the microelectronics industry and produced at high quality. The Deamer group (2001) described a method for nanopore fabrication that involves exposing the sample to a focused ion beam to be ceased on detection of ion transmission [74]. It was found that the size of the pore could be controlled to nanometre precision by careful regulation of the temperature and ion rate.

Another technique from the Dekker group (2005) uses a two step process, first electron beam lithography etches holes of around 20 nm, then it was found that imaging these holes with a transmission electron microscope (TEM) under high-intensity illumination would cause the pore size to grow or shrink, allowing nanometre control of the pore size by using image feedback [75].

6.1.3 Hybrid pores

Solid state pores have recently been used as a cradle to embed biological pores, combining the advantages of atomically precise structure with a stable and spatially configurable membrane. This was first achieved in a collaboration between the Bayley and Dekker groups (2010) [66] by chemically attaching a long double stranded DNA chain to the end of the αHL barrel. The grafted strand of DNA acts as guide for the biological pore, threading through the solid state pore by electrophoresis and subsequently embedding the biological pore into the solid state support. This concept was taken further in the Keyser group (2012) [76] by constructing the biological pore from a self-assembling DNA template, commonly known as DNA origami, see Figure 6.2b). This allows the construction of a wide range of geometric structures and base patterning with atomistic accuracy. In Chapter 7 we build upon the possibility of internal pore patterning for stochastic sensing.

6.2 Theory

6.2.1 Scaling

Polymer theory has a long history of scaling arguments going back to de Gennes [77]. Here we will consider only a few key arguments related to polymer translocation. In general, the average size of a polymer scales as $\bar{R} \propto N^{\nu}$ where ν is the Flory exponent. An equilibrium ideal freely-jointed chain, or Gaussian chain, scales as $\bar{R} \propto N^{1/2}$. Solvents in which a polymer behaves as an ideal chain are called *theta solvents*. These ideal chain models do not take into account excluded volume between segments of the polymer. If the polymer-solvent interaction is energetically favourable then the excluded volume interaction is felt between segments and the polymer said to exist in a *good solvent*. The Flory exponent for a good solvent depends on dimension, $\mathcal{D}$, with an approximate relation $\nu \sim 3/(2+\mathcal{D})$.

Whether or not the polymer chain attains an equilibrium conformation on either side of the membrane is dependent on the polymer having a fast relaxation time as compared to its translocation time. The relaxation time for a polymer chain without hydrodynamics is given by the Rouse model and scales as $\tau_R \propto \tau_0 N^2$. With hydrodynamic interaction it is given as $\tau_Z \propto \tau_0 N^{3/2}$ by the Zimm model, where $\tau_0 = \eta b^2/k_b T$ is a microscopic time scale set by the solvent viscosity η, bead size b, and thermal energy $k_B T$ [35]. Notice how hydrodynamic interaction leads to a faster relaxation time for a given polymer size.

The dissipation dynamics can be captured more generally in terms of a *dynamic exponent*, z. We define the friction coefficient $\gamma = \gamma_0 N^{(z-2)\nu}$, which sets the diffusion coefficient by

the Stokes-Einstein relationship $D = k_bT/\gamma$ and is related to the relaxation time by $\gamma \sim m/\tau$. *Free-draining* dissipation corresponds to Rouse dynamics with $z = (1+2\nu)/\nu$ and *non-draining* to Zimm dynamics with $z = 3$.

Several scaling arguments have been proposed for the length dependence of the translocation time $\tau \propto N^\alpha$, where α is the exponent of interest. These can be categorised on the basis of equilibrium or non-equilibrium arguments. It is becoming well understood that translocation is a highly non-equilibrium process and so equilibrium arguments have a very narrow range of applicability. We reserve the non-equilibrium arguments to a later section and mention here only a few points of interest for equilibrium arguments. The boundary between equilibrium and non-equilibrium conditions can be approximately captured by comparing the driving force to thermal energy $fbN^\nu \sim k_bT$. Defining the dimensionless forcing parameter $\tilde{f} = fb/k_bT$, we expect equilibrium arguments to hold only when $\tilde{f} < N^{-\nu} \ll 1$.

Following Sakaue (2010) [78], the translocation dynamics are given by the balance between driving force f and dissipation γv. The friction coefficient can be expressed as $\gamma \sim R^{z-2} = \gamma_0 N^{(z-2)\nu}$ where $\gamma_0 \sim \eta a$ is the single monomer friction coefficient and z is the dynamic exponent, which is dependent on the mode of dissipation [77]. Under a driving force the number of untranslocated monomers $N(t)$ will decrease in time. The equilibrium conformation of the polymer on the cis side will therefore have a time dependent radius of gyration. Defining the velocity $v = -\partial_t R(t) = -b\partial_t N(t)^\nu$, the force balance results in the differential equation $\partial_{\tilde{t}} N(t)^\nu = -N^{-(z-2)\nu}/\tilde{f}$, where time has been made dimensionless by τ_0. This gives the translocation time as $\tilde{\tau} = N_0^{(z-1)\nu}/\tilde{f}$. If the friction is local, or free-draining, then $\gamma \sim \gamma_0 N$, and so $z = (1+2\nu)/\nu$, and the translocation time scales as

$\tau = N_0^{1+\nu}/\tilde{f}$, as originally derived by Kantor and Kardar (2004) [79]. For non-draining interactions the dynamic exponent is $z = 3$ and the translocation time scales as $\tau = N_0^{2\nu}/\tilde{f}$ as quoted by Storm *et al.* to interpret the results from their solid state nanopores experiments [75].

6.2.2 Free energy

In the same year as the initial Kasianowicz translocation experiment Sung and Park (1996) [80] constructed an equilibrium free energy barrier description of the translocation process. The free energy of a polymer of m beads with Kuhn length b was calculated by considering the entropy of an ideal freely-jointed chain polymer with one end fixed to an infinite plane and is found to vary logarithmically with m. A polymer of total subunits N with m beads on one side and $N - m$ on the other has a total free energy $\beta\mathcal{F} = 1/2 \ln m + 1/2 \ln(N-m) - \beta m \Delta\mu$ where $\beta = (k_b T)^{-1}$ and $\Delta\mu$ is the transmembrane chemical potential difference that can arise though a voltage or concentration difference. This analysis reveals a free energy barrier for translocation with a critical number of translocated beads for the process to become favourable [81]. When considering the initial filling of a pore by a polymer with excluded volume the free energy barrier can be much higher than the method stated here. As this is an equilibrium argument it is only valid for polymer relaxation times that are much faster than the translocation time.

6.2.3 Fokker-Planck

A model for homopolymer translocation inspired by the experiments of Kasianowicz *et al.* was described by Lubensky and Nelson (1999) [82]. This was the first study to derive an analytical form for the translocation time distribution that takes into account the polymer-pore interaction. The translocation was modelled phenomenologically as a one dimensional Fokker-Plank drift-diffusion process, $\partial_t P(x,t) = D\partial_x^2 P(x,t) - v\partial_x P(x,t)$ with D and v as an effective diffusion and average drift velocity to be determined from a microscopic model of the pore and x as the translocated polymer length. Absorbing boundary conditions were set at each end of the domain, which created some difficulty when taking the limit of the initial condition at the boundary. The effective diffusion D and average velocity v were calculated by considering an effective particle in a one dimensional periodic potential described by the Smoluchowski equation $\partial_t P = D_o \partial_x \left[\partial P + \beta(\partial_x U - F)P\right]$ where $U(x+b) = U(x)$ and b is the distance between bases. The periodic landscape represents the energetic interaction between the polymer and the pore.

A number of important conclusions were obtained from their results. The translocation time distribution, $\rho(\tau)$, was found to be skewed, suggesting that the average translocation time $\langle\tau\rangle$ is not a good measure. Instead the most probable translocation time should be used, $\tau_{\max}$, unless $v \gg D$, in which case they should approach the same value. Unfortunately, the average translocation time tends to be quoted more often in the literature. The most probable translocation time shows the simple form $\tau_{\max} = aN/v$ as $N \to \infty$, but falls away rapidly from this value at finite N.

Surprisingly, there was little comparison of their model with experimental data. However,

recent work by Reimann *et al.* (2012) [83] has revisited the Lubensky-Nelson model and has shown an excellent agreement. It was also found that the Lubensky-Nelson model predicts the experimentally observed exponential decay in the translocation time distribution.

In later sections, we will use the form of the Lubensky-Nelson translocation time distribution as given by Reimann *et al.*

$$\psi(\tilde{t}) = \frac{c}{\tilde{t}} \sum_{n=1,3,5\ldots} \frac{\dfrac{n^2}{\kappa\tau} - \dfrac{1}{2}}{\exp\left\{\dfrac{2(n-1)}{\kappa} + \dfrac{(\tau-n)^2}{\kappa\tilde{t}}\right\}} \tag{6.1}$$

where c is a normalisation constant

$$c = \frac{v}{L}\sqrt{\frac{\kappa}{\pi}}\left[1 - e^{-4/\kappa}\right] \tag{6.2}$$

$\tilde{t} = rt$ is the rescaled time and the distribution is specified by two parameters $r = v/L$ and $\kappa = 4D/vL$. A value for κ can be estimated from the translocation time distribution as $\kappa = [(t_{\mathrm{R}} - t_{\mathrm{L}})/t_{\max}]^2/2$.

6.2.4 Non-equilibrium

It has become clear that translocation is a highly non-equilibrium process and this must be considered in order to capture the correct translocation dynamics and scaling behaviour for even moderate forces. This remains an active area of research and the purpose of this section is to qualitatively describe the non-equilibrium features and highlight some notable contributions.

The non-equilibrium translocation process can be pictured intuitively by considering a macroscopic argument proposed by Grosberg *et al.* (2006) [84]. Imagine a rope placed carelessly on a desk with one end dangling at the edge. Pulling this free end down smoothly would not cause the rope to move all at once. Instead, the nearest section would start to *unfold* and straighten out. As it straightens the pulling force would be transmitted to the next fold, this process repeats propagating the tension along the rope. This notion of *tension propagation* is central to non-equilibrium polymer translocation.

For a complete description of tension propagation in a polymer one must consider the hydrodynamic friction response, the stiffness of the backbone, excluded volume interaction and thermal fluctuations under external perturbations. For instance, Hallatschek *et al.* (2005) [85] have considered a worm-like chain model with thermal fluctuations in free solution under the influence of a wide range of external perturbations. However, for polymer translocation one must also consider the effects of confinement and surface interactions resulting in a formidable list of requirements.

Sakaue [78, 86–88] has considered the scaling behaviour of non-equilibrium translocation by separating the polymer into a tensed and relaxed region bounded by a propagating front. An equation of motion for the front can be made by relating a continuity equation for monomers in the tensed region to the speed and the monomer density at the front. At very weak driving forces $f < k_bT/aN^\nu$, equilibrium arguments can be considered, but for moderate driving forces, $k_bT/aN^\nu < f < k_bT/a$, the dynamic unfolding of the polymer must be taken into account. This has been considered within the blob model by introducing a spatially dependent length scale such that the blobs near the pore are very small and increase in size towards the tension front. A drag force balance can then be

made to find the front velocity and monomer density. For larger forces $f > k_b T N^{\nu}/a$ the polymer becomes highly extended in the tensed region and at some point the blob model will break down. The scaling results were generalised in terms of the Flory Exponent, ν, and the dynamic exponent, z, allowing a wide comparison to simulations and experiments in different dimensions and conditions with excellent agreement [78].

6.3 Simulations

Many simulation methods have been used to study polymer translocation, including Monte Carlo methods using kink-jump [89], standard [90] and fluctuating bond moves [91], Brownian/Langevin Dynamics methods [92–96], combined Langevin Dynamics with Poisson-Nernst-Planck for ionic currents [97] and all-atom molecular dynamics [98]. Several simulations have considered the atomistic structure of αHL [97, 98], while most concentrate on simple holes in planar membranes. Much confusion about the translocation time scaling with polymer length $\tau \sim N^{\alpha}$ has been created in part due to the multitude of simulation methods. The scaling exponent is dependent on dimension and the dissipation mechanism such that there are many levels of description available to simulation. Several reviews have begun to clarify this confusion, see Luo (2009) [96] and Sakaue (2010) [78].

Most simulations proceed in a similar fashion. The focus of interest is the polymer dynamics during the translocation process and not on how translocation was initiated. To this end, simulations begin with a small section of the polymer in or close to the pore. The duration of the translocation event is then measured using a clock that starts on entry of the polymer head and stops on exit of the tail. By repeating this process hundreds or

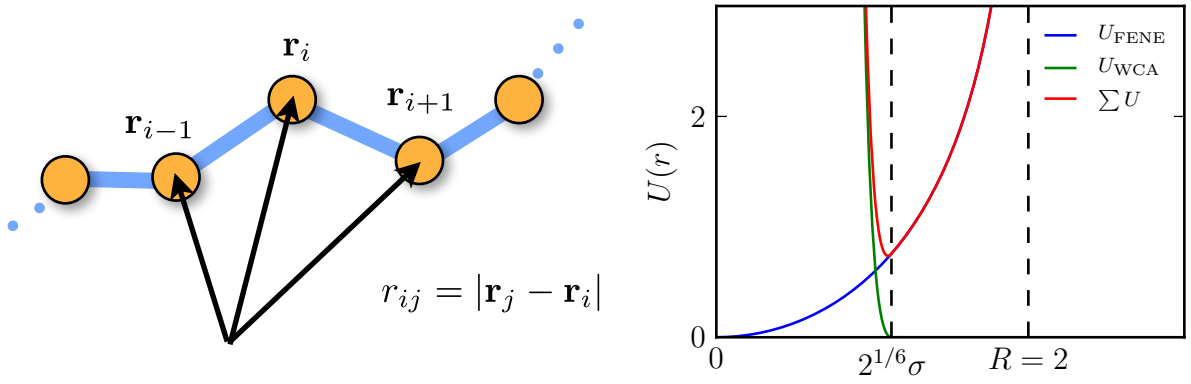

FIGURE 6.3: The polymer is modelled as WCA beads connected by FENE springs (left). The FENE and WCA potential is shown along with the sum of the two (right)

thousands of times sufficient statistics can be gained to construct the translocation time distribution.

6.4 Model

In this section we describe the polymer model and numerical method used in the following two chapters.

6.4.1 Interaction potentials

The polymer is coarse grained into a series of Lennard-Jones (LJ) beads connected with finite extension nonlinear elastic (FENE) springs, see Figure 6.3. The LJ potential enforces excluded volume between beads and has the following piecewise short range repulsive form

$$U_{\mathrm{WCA}}(r) = \begin{cases} 4\epsilon\left[\left(\frac{\sigma}{r}\right)^{12} - \left(\frac{\sigma}{r}\right)^{6}\right] + \epsilon & : r \leq 2^{1/6}\sigma \\ 0 & : r > 2^{1/6}\sigma \end{cases} \tag{6.3}$$

where ϵ is the Lennard-Jones depth parameter r is the centre to centre separation between beads and σ is the bead diameter. This is commonly known as the Weeks-Chandler-Andersen (WCA) potential.

The FENE spring ensures that the polymer cannot be stretched beyond a maximum length, R. This is an important constraint in simulations where the polymer is forced as it prevents unphysical extension lengths that could occur with a harmonic potential. The FENE potential takes the form

$$U_{\mathrm{FENE}}(r) = -\frac{1}{2}kR^2 \ln\left(1 - \frac{r^2}{R^2}\right) \tag{6.4}$$

where k is the spring constant. U_{FENE} slowly diverges as $r \to R$ enforcing a maximum extension length of $L = NR$ where N is the number of beads. In two dimensions it is possible that the numerical method may allow unphysical polymer chain crossing unless the maximum separation is constrained such that $R \leq 2\sigma$.

The pore is constructed from a static arrangement of beads. When an attractive interaction is desired between pore beads and monomers a standard Lennard-Jones potential is used

$$U_{\mathrm{LJ}}(r) = 4\epsilon_{\mathrm{pm}}\left[\left(\frac{\sigma}{r}\right)^{12} - \left(\frac{\sigma}{r}\right)^{6}\right] \tag{6.5}$$

Here ϵ_{pm} sets the bonding affinity of monomers to the pore beads. Monomers inside the pore feel a driving force due to the applied electric field. We assume the following potential

across the pore

$$U_{\rm pore}(\mathbf{r}) \;=\; qV \begin{cases} 1/2 & : \quad x < -L/2 \\ -x/L & : \; -L/2 < x < L/2 \\ -1/2 & : \quad x > L/2 \end{cases} \tag{6.6}$$

where q is the charge on the coarse grained monomer, V is the potential difference and L is the length of the pore, which is symmetric about the coordinate system. The driving force within the pore is $F = qV/L$.

6.4.2 Langevin equation

The position of a polymer bead, $\mathbf{r_i}$, is updated using the Langevin equation

$$m\ddot{\mathbf{r}}_\mathbf{i} = -\zeta\dot{\mathbf{r}}_\mathbf{i} - \nabla_{\mathbf{r_i}}\mathbf{U_i}(\mathbf{r_i}) + \xi \tag{6.7}$$

where $U_i(\mathbf{r_i})$ includes the interactions from all particles and neighbouring bonds $U_i(\mathbf{r_i}) = \sum_{j\neq i} U_{\rm WCA}(r_{ij}) + U_{\rm LJ}(r_{ij}) + U_{\rm FENE}(r_{ij}) + U_{\rm pore}(\mathbf{r_i})$ and $U_{{\rm FENE},j}(r) = 0$ for $|j-i| > 1$ where $r_{ij} = |\mathbf{r_j} - \mathbf{r_i}|$ and $\xi(t)$ describes thermal fluctuations with $\langle\xi(t)\rangle = 0$ and $\langle\xi(t)\xi(t')\rangle = 2k_bT\zeta\delta(t-t')$ satisfying the fluctuation dissipation theorem [99]. A commonly employed velocity Verlet type algorithm described by Allen and Tildesley [100] is used to numerically integrate the positions.

We solve the Langevin Dynamics equations neglecting hydrodynamic interactions corresponding to a self avoiding polymer with Rouse dynamics.

6.4.3 Reduced units

We make all parameters dimensionless using units of ϵ, σ, m and $(m\sigma^2/\epsilon)^{1/2}$ for energy, length, mass and time respectively. Following Luo *et al.* [95], we assume that the size of each bead in our coarse grained polymer model corresponds to the Kuhn length of a ssDNA, which is approximately three nucleotide bases. This sets the bead size $\sigma \approx 1.5\,\mathrm{nm}$, the mass of the bead $m \approx 936\,\mathrm{amu}$, given that the mass of a base in DNA is $\approx 312\,\mathrm{amu}$, and the charge of a bead $q \approx 0.3\,\mathrm{e}$, each base effectively having a charge of $0.1\,\mathrm{e}$ [101]. We set $\zeta = 0.7$ and $k_BT = 1.2$ to allow comparison with known results. Therefore, the interaction strength at $T = 295\,\mathrm{K}$ is given by $\epsilon = k_BT/1.2 \approx 3.4 \times 10^{-21}\,\mathrm{J}$. This gives the time scale of $(m\sigma^2/\epsilon)^{1/2} \approx 30\,\mathrm{ps}$ and a force scale of $\epsilon/\sigma \approx 2.3\,\mathrm{pN}$. Therefore an external driving force in the range $0.5 - 1.0$ corresponds to a voltage range $V = FL/q \approx 190 - 380\,\mathrm{mV}$ across the pores.

6.4.4 Discussion

It is worthwhile to discuss a few decisions made about the model and simulation method.

Langevin Dynamics simulations are very flexible and appropriate for capturing non-equilibrium effects. Standard Monte Carlo simulations sample only the equilibrium state making it inappropriate for non-equilibrium study. Other methods, such as dynamic or kinetic Monte Carlo, can be used for non-equilibrium systems. However, in these cases the transition rates between all states must be known beforehand, which may not be practical.

The choice of particle interaction potentials in coarse grained models is not unique. For instance, the Morse potential offers greater flexibility in defining the range and strength of interaction over the Lennard-Jones potential. The cut-off distance between long range potentials can affect results and cause problems due to discontinuities. This has led some people to interpolate the potentials such that they tend to zero smoothly over a finite range.

Enforcing a maximum bond length is an important constraint for polymers. Rather than using an interaction potential, constrained dynamics algorithms such as RATTLE and SHAKE could be used. Although effective, these algorithms have reported issues with cyclic or branched topologies. Here simple linear polymers have been used but future polymer models may have more complex bonding, which is easily incorporated with FENE potentials.

Hydrodynamics cannot easily be incorporated into Langevin Dynamics simulations due to particle inertia. Having a compatible description of hydrodynamics would require solution of the Navier-Stokes equation allowing momentum transfer between polymer and fluid. Solution of these equations by methods such as SIMPLE, Multi-particle Collision Dynamics (MPCD) or Lattice Boltzmann can become computationally very costly and impractical for gaining large statistics, although less so for MPCD. When considering time scales longer than the molecular scale of the solvent, m/ζ, the overdamped limit approximation can be made, effectively making $\ddot{\mathbf{r}}$ negligibly small in Equation 6.7. This marks the distinction between Langevin Dynamics (with inertia) and Brownian Dynamics (without inertia).

At small length scales it is appropriate to make the low Reynolds number approximation resulting in the Stokes equations of hydrodynamics. Green's function, or singularity [102], solutions to the Stokes equation can then be used in Brownian Dynamics to incorporate hydrodynamic interactions [103]. However, analytical solutions of the Green's function are only known in bulk or for a few simple geometries [104]. In complex confinements numerical methods can be used to calculate the Green's functions [105–107] or the Stokes equations can be solved by Finite Volume Method (FVM), Finite Element Method (FEM) or Boundary Element Method (BEM) techniques.

Chapter 7

Patterned pores

Corresponding publication:

- J. A. Cohen, A. Chaudhuri and R. Golestanian,
  Stochastic Sensing of Polynucleotides Using Patterned Nanopores,
  Physical Review X **2**, 021022 (2012)

7.1 Introduction

As described in the previous chapter, much experimental and theoretical work has been motivated by the goal of next generation sequencing devices. One great difficultly in accurate sequencing is the noise inherent in current-blockade measurements. In order to gain reliable readings time averaging must be performed, requiring the translocation process to be much slower than the current measurement sampling time. The spread in translocation times can be very large despite identical polymers passing through the same pore. These observations lead to a central conclusion applicable to many systems at the mesoscale with important implications for sensing: *noise is unavoidable.*

Many quantities at the mesoscale no longer have well defined values and must be described probabilistically. Instead of trying to eliminate noise, which in many cases is futile, it is

provocative to think that the extra information could be used to our advantage. This brings us to the notion of *stochastic sensing*.

In this chapter we show that the statistics of polymer translocation can be controlled through patterning of surface interactions. These patterns could be created by designing a hybrid DNA origami pore, as mention in Section 6.1.3, that has a few bases open for binding in the pore interior. This leads to the question of whether translocation time distributions can be engineered such that different molecules are sufficiently distinguishable.

We demonstrate that this is possible using a set of block co-polymers of length $N = 64$ with block sizes of $M = 2, 4, 8, 16, 32$ and 64 translocating through two types of specially designed pores integrated into a model device. We describe two sensing algorithms that allow identification through exclusion of unlikely candidates and consider the effect of randomised entry orientations. By increasing the number of measurements, and thus sampling the distributions more fully, we show this can be made increasingly robust. This could lead to faster sensing devices as the process no longer needs to be slowed down in order to gain reliable readings. Instead, a series of high-speed measurements could be made.

In Section 7.2 we introduce the set of three pores used in this study and define the filling, transfer and escape translocation times. In Section 7.3 we study the translocation statistics for a homopolymer with variable affinity to the pores. We show that the escape time becomes the limiting process for all pores at high affinity. In Section 7.4 we describe the block co-polymers and present their translocation distributions. In Section 7.5 we describe two stochastic sensing algorithms and compare their accuracy with fixed and uncorrelated translocation orientations. Finally we draw some conclusions from this investigation.

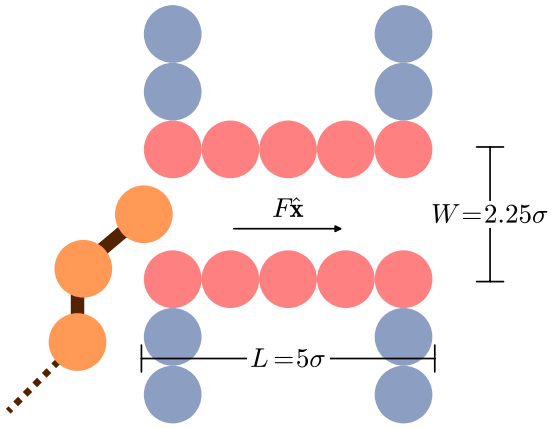

FIGURE 7.1: Schematic representation of the system. The polymer (orange) translocates from the *cis* to the *trans* side of the pore. The pore (red) is embedded within a wall (blue). The pore will be patterned with attractive and repulsive monomers as described later.

7.2 Methods

7.2.1 Patterns

We consider a polymer translocating through a pore in a rigid membrane, see Figure 7.1. Three types of pore patterns are investigated, shown schematically in Figure 7.2. Pore α is the control pore and is uniformly attractive. Pore β is symmetric with an attractive entrance and exit. Pore γ is asymmetric with an attractive entrance and is coarsely similar to αHL. The pores have a width $W = 2.25\sigma$ and length $L = 5\sigma$. The polymer monomers feel an affinity ϵ_{pm} to the attractive beads and experience a driving force F with the pore.

In terms of ssDNA translocation through hybrid pores, the attractive interaction between pore monomers and polymer monomers represents a binding interaction between an 'open' base inside the DNA origami pore and a base along the translocating ssDNA, for example an A-T or C-G interaction. The short range repulsive interaction represents a region of

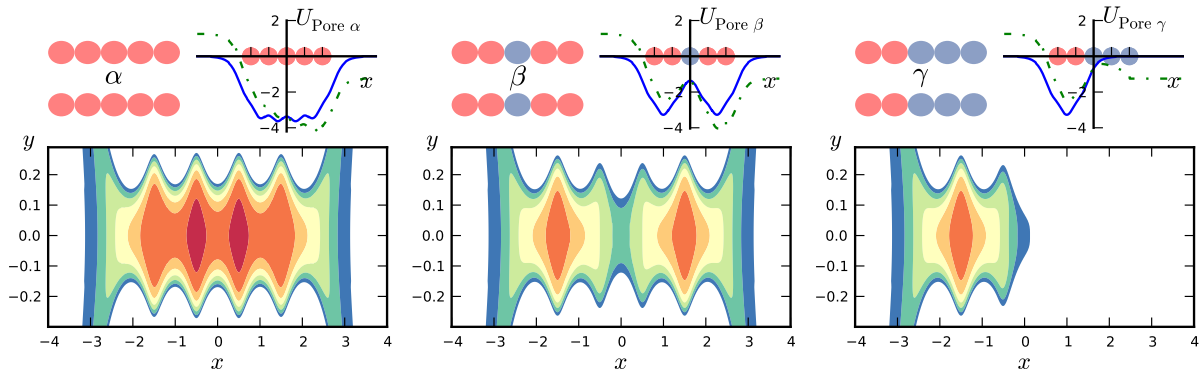

FIGURE 7.2: Comparison of the pore-monomer interaction potentials shown in three panels, Pore α (left), Pore β (middle), Pore γ (right). For each panel there are three sub panels. (Top left) A schematic of the pore. Pore monomers can either have an attractive (LJ) interaction (red) or a short range repulsive (WCA) interaction (blue) with the polymer monomers. (Top right) The potential energy landscape in the center ($y = 0$) along the length of the channel (blue) is modified (green) in the presence of an external driving force $F = 0.5\epsilon/\sigma$. (Bottom) The potential energy landscape experienced by a single polymer monomer inside the pore. Blue to red represents increasing potential depth with only the $U < 0$ regions shown.

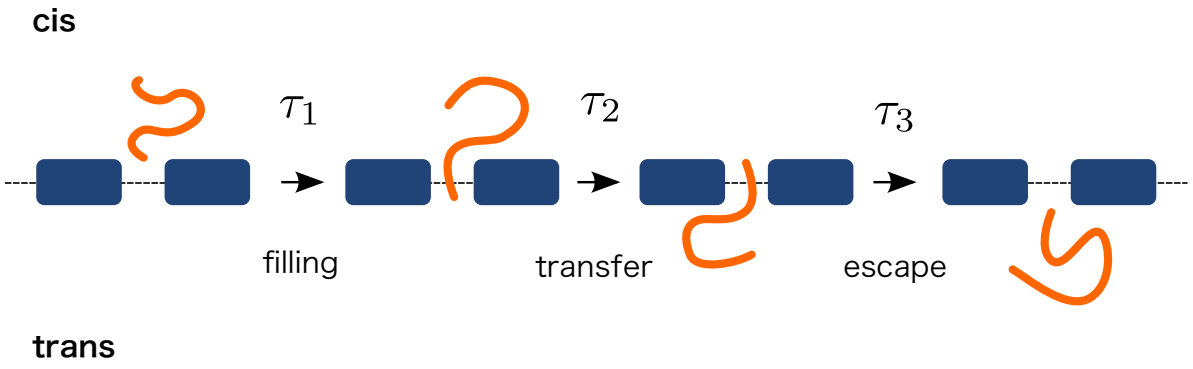

FIGURE 7.3: Translocation subintervals.

the pore where there are no bases exposed for binding and instead the polymer interacts with the DNA origami backbone.

At this level of description the pore patterning could equally well apply to a hydrophobic and hydrophilic interaction between proteins, or changes in Van der Waals interaction due to different material properties.

7.2.2 Translocation stages

We split the translocation time, τ, into three subintervals corresponding to the time to fill the pore, τ_1, to transfer the bulk of the polymer to the trans side, τ_2, and to escape from the pore, τ_3, see Figure 7.3. These times are characterised by counting the number of monomers on the cis size $N_{\text{cis}} = \int \mathrm{d}y \int_{-\infty}^{-L/2} \mathrm{d}x\, \rho(x,y)$, inside the pore $N_{\text{pore}} = \int \mathrm{d}y \int_{-L/2}^{L/2} \mathrm{d}x\, \rho(x,y)$ and on the trans side $N_{\text{trans}} = \int \mathrm{d}y \int_{L/2}^{\infty} \mathrm{d}x\, \rho(x,y)$ where $\rho(x,y) = \sum_{i=1}^{N} \delta(x-x_i)\delta(y-y_i)$ and (x_i, y_i) are the monomer coordinates.

Four events in the translocation process are used to determine the subintervals. The start time, t_0, is marked at the point $N_{\text{cis}} \neq N$ and is reset if $N_{\text{cis}} = N$, the filled time, t_1, at $N_{\text{trans}} \neq 0$ and is reset if $N_{\text{trans}} = 0$, the transferred time, t_2, at $N_{\text{cis}} = 0$ without a reset, and the translocated time, t_4, occurs when $N_{\text{trans}} = N$. From this we calculate the *filling* interval, $\tau_1 = t_1 - t_0$, the *transfer* interval, $\tau_2 = t_2 - t_1$, and the *escape* interval, $\tau_3 = t_3 - t_2$. These definitions best capture the nature of the three stages and are sequential such that $\tau = \tau_1 + \tau_2 + \tau_3$.

7.3 Homopolymer translocation

7.3.1 Hard rod model

The impact of pore patterning on the different stages of translocation can be understood by considering a simplified hard rod model. This is relevant because within the pore the polymer assumes a one dimensional conformation. Consider N beads arranged at coordinates $(x_i,\, y_i) = (s - \sigma i,\, 0)$ where s is the head position and can be thought of as a translocation 'reaction' coordinate, σ is the bead diameter and i is the particle index. The hard rod interaction potential, $U(s)$, is found by summing the Lennard-Jones

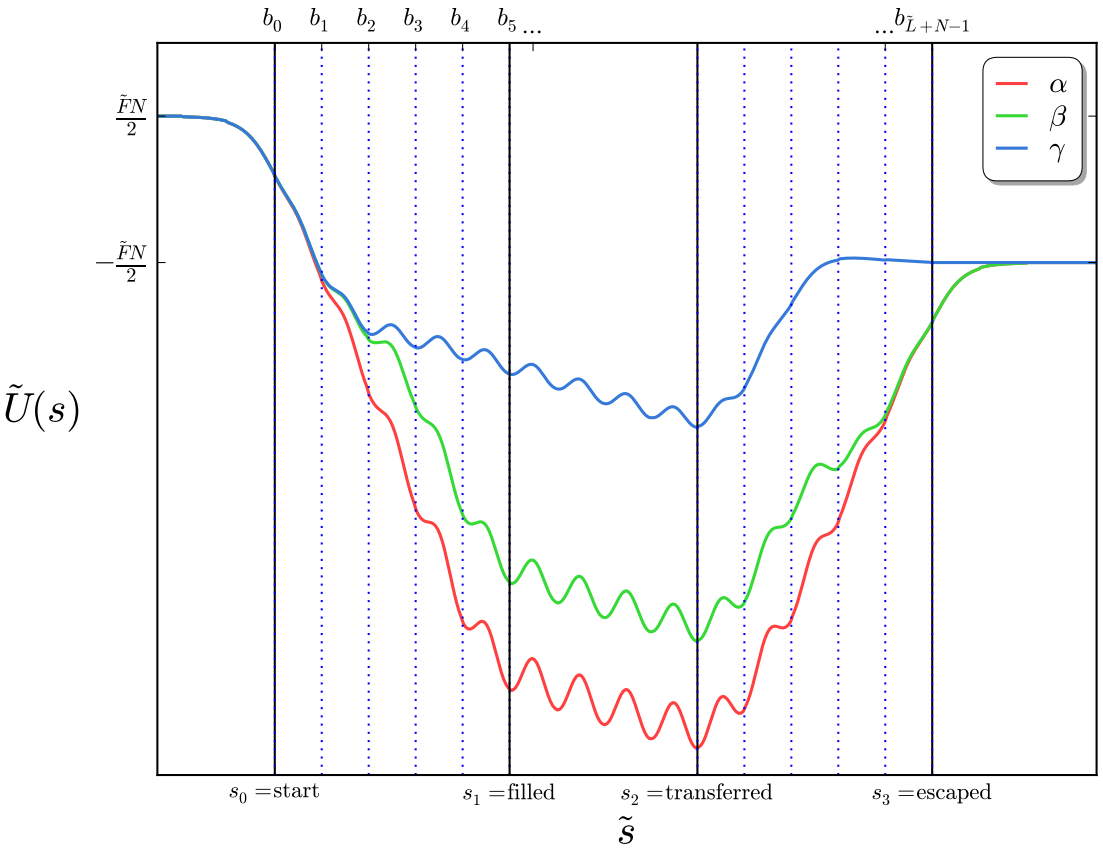

FIGURE 7.4: Interaction potential, $\tilde{U}(\tilde{s}) = U(s/\sigma)/\epsilon$, as a function of translocation coordinate, $\tilde{s} = s/\sigma$ for a hard rod. Black lines mark the translocation events. Dotted blue lines mark 'binding sites' that occur in the spaces between the pore monomers. Shown for $\epsilon_{\rm pm} = \epsilon$ and $F = 0.5\epsilon/\sigma$.

potential between rod and pore beads and is shown for the three pore types in Figure 7.4. The translocation coordinates corresponding to the four key translocation events are: start $s_0 = -L/2$, filled $s_1 = L/2$, transferred $s_2 = (N-1)\sigma - L/2$ and escaped $s_3 = (N-1)\sigma + L/2$. It is helpful to consider 'binding sites' signified by minima in the interaction potential between the pore monomers and their associated forward, k_+, and backwards, k_-, hopping rates. The binding sites are marked with dotted blue lines in Figure 7.4 and the hopping rates, $k_\pm \sim (k_B T/\gamma)e^{-E_\pm/k_B T}$, can be estimated relative to each other by considering the height of the next, E_+, or previous, E_-, barrier. The homopolymer translocation results will be interpreted with reference to these quantities.

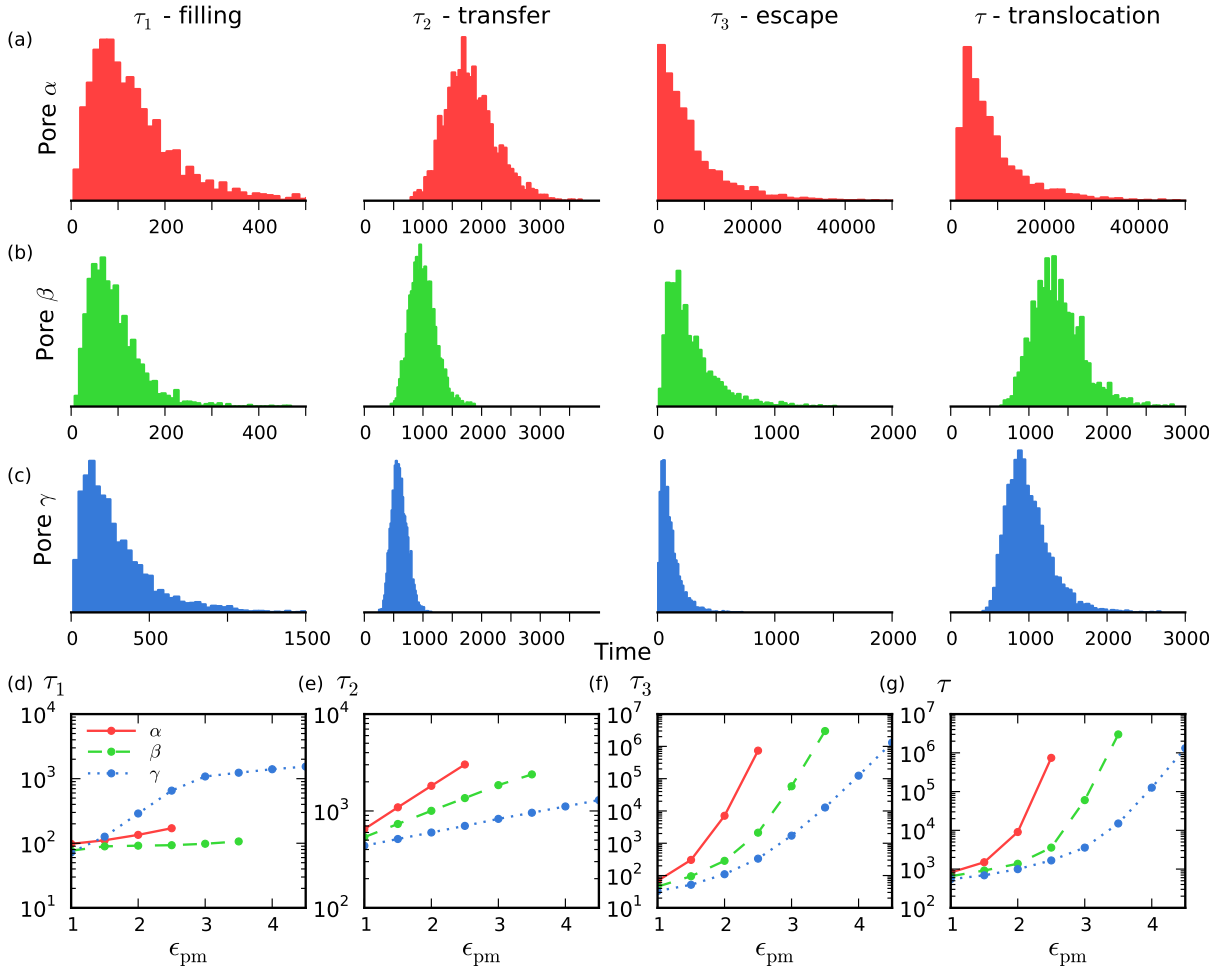

FIGURE 7.5: Translocation time statistics for homopolymers obtained from Langevin Dynamics simulation. (a-c) Comparison of translocation time distributions for the three patterned pores, with $F = 0.5\epsilon/\sigma$ and $\epsilon_{pm} = 2.0\epsilon$. (d-f) Comparison of average filling, transfer and escape times as a function of ϵ_{pm} for the three different pores with $F = 0.5\epsilon/\sigma$.

7.3.2 Translocation times

The filling, transfer and escape distributions are similar across the three pores but have distinctly different scales, resulting in discernibly different total translocation time distributions, see Figure 7.5. For Pore α and Pore β the filling time, τ_1, is weakly dependent on the affinity, ϵ_{pm}, however Pore γ initially shows a stronger dependence, see Figure 7.5 d). It can be seen from Figure 7.4 that Pore γ has to overcome several barriers between s_0 and s_1 in order to initiate the transfer stage. These barriers are reflected in the longer exponential tail seen in the filling time distribution relative to the other two pores, see

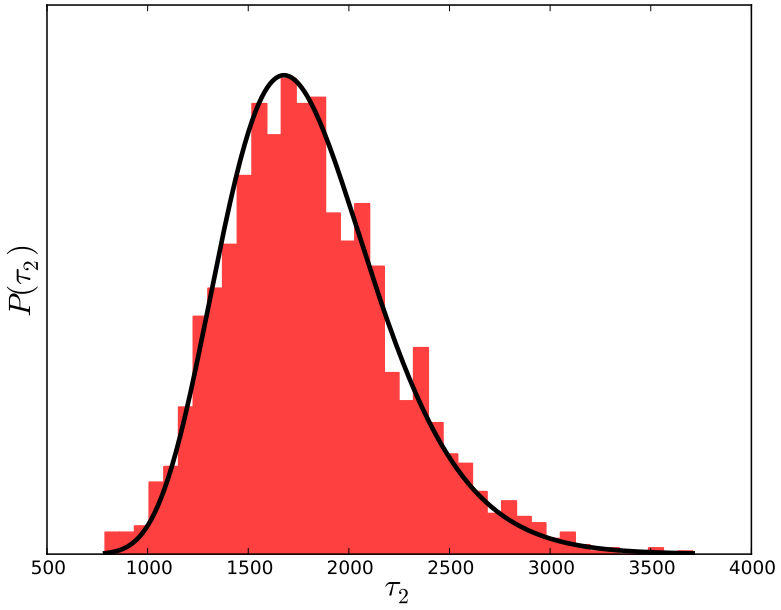

FIGURE 7.6: Transfer time distribution fit with the Lubensky-Nelson model, as given by (6.1), using parameters $r = v/L = 0.5 \times 10^{-3}\,\mathrm{s}^{-1}$ and $\kappa = 0.1$.

τ_1 in Figure 7.5 a)-c). This is due to the asymmetric shape of Pore γ favouring filling only up to binding size b_2, see Figure 7.2. Likewise, in the final stages of filling Pore α must overcome a larger barrier than Pore β at site b_4. This results in a slightly stronger dependence of the filling time of Pore α as compared to Pore β.

Between the filled, s_1, and transferred, s_2, stages the hard rod potential closely resembles a sinusoid with a period set by the monomer separation. In the absence of a forcing bias the amplitudes roughly follow the relationship $A_\beta/A_\alpha \sim 4/5$ and $A_\gamma/A_\alpha \gtrsim 2/5$ as expected from the number of attractive monomers in each pore, with the latter being slightly larger. This is represented in the decreasing mean position of the transfer distributions, see τ_2 in Figure 7.5 a) - c). The transfer time exhibits a regular exponential dependence on ϵ_{pm} for all pores with relative time scales consistent with the number of attractive monomers, Figure 7.5 e).

The Lubensky-Nelson model to applies to the transfer stage, and one would expect the

analytically obtained translocation time distribution to match the numerical results. Surprisingly, there are no known comparisons in the literature. Indeed, estimating κ as described in Section 6.2.3 and allowing the second parameter, $r = v/L$, as a free parameter the distribution is found to match the numerical data very well, see Figure 7.6. It should be possible to calculate the distribution parameters κ and r by considering a simplified polymer model, although there is some difficulty in assigning a value for the effective friction coefficient in the one coordinate Fokker-Planck equation.

The escape time, τ_3, becomes the longest time scale and differs most dramatically across the three pores, see τ_3 in Figure 7.5 a)-c). This is a result of the large difference in interaction potential between s_2 and s_3 with decreasing magnitude for Pores α, β and γ respectively. It can be seen from the hard rod potential for Pore γ in Figure 7.4 that a peak occurs at $b_{\tilde{L}+N-3}$ with escape becoming energetically favourable once this has been surmounted. For Pore β there is a minimum at site $b_{\tilde{L}+N-3}$ with a lower backwards rate, k_-, than the previous or following site. This serves as an intermediate point before attempting escape at s_3. Pore α, however, has a very high probability of a backwards hop compared to forwards for the entire region, making transit to s_4 very unlikely. This is reflected in the very strong affinity dependence of Pore α, see Figure 7.5 f).

Under the weak driving force investigated here, the average total translocation time, τ, becomes dominated by the escape time with increasing affinity, see Figure 7.5 g), causing the form of the translocation time distribution to differ significantly between the pores, see τ Figure 7.5 a)-c). This sensitivity to patterning suggests it may be possible to engineer pores to generate unique statistical features that could be used in stochastic sensing.

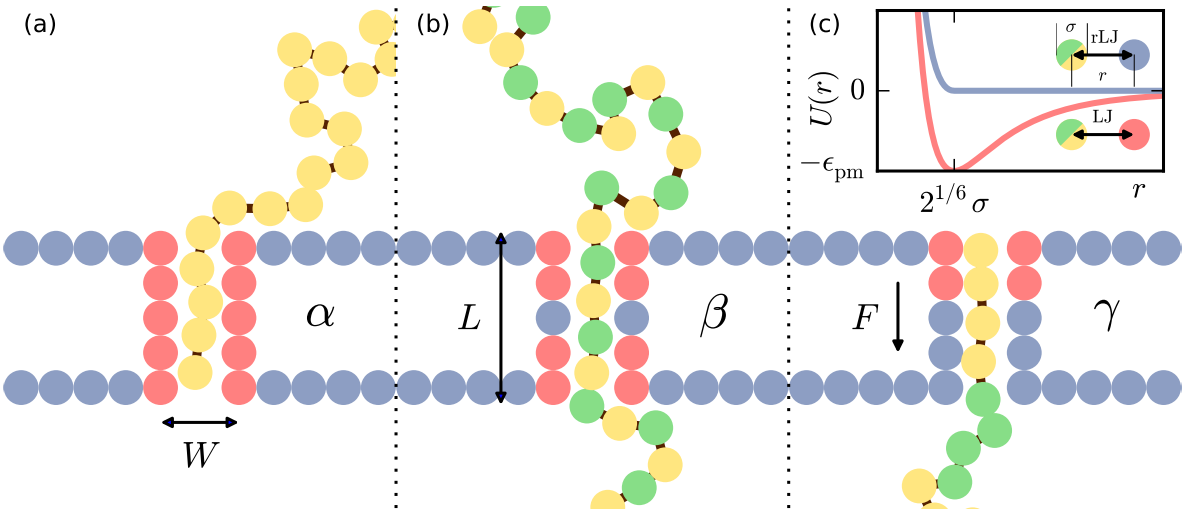

FIGURE 7.7: Translocation of symmetric block-copolymers of the form A_nC_n, where $M = 2n$ is the block length, through the three patterned pores. Type 'A' monomers (yellow) experience a higher affinity to the attractive pore monomers (red) than the type 'C' monomers (green). Both A and C have a short ranged WCA interaction with the wall monomers (blue). The interaction potentials are summarised at the top right.

7.4 Block co-polymer translocation

It has been seen from the homopolymer investigation that pore patterning can significantly impact the form of the translocation time distributions. We now examine the possibility of heteropolymer detection by extending this investigation to block co-polymers containing symmetric purine-pyrimidine nucleotide blocks of the form A_nC_n, where $M = 2n$ is the block length. This choice of polynucleotide is in keeping with previous experimental [108] and theoretical [109] studies and simplifies the investigation as no secondary structures are formed.

We assign different values for the affinities of base A, ϵ_{pA}, and base C, $\epsilon_{pC} = \epsilon$, with the attractive pore monomers, such that $\epsilon_{pA} = 3\epsilon_{pC}$. This represents a preference for base A to bind with the attractive pore monomers as would be achieved by patterning the pore with complementary base T to form the base pair A-T. The weaker interaction represents a less favourable binding mismatch, such as C-T. The short range repulsive interaction corresponds to a region of the pore that does not have any open bases exposed and the

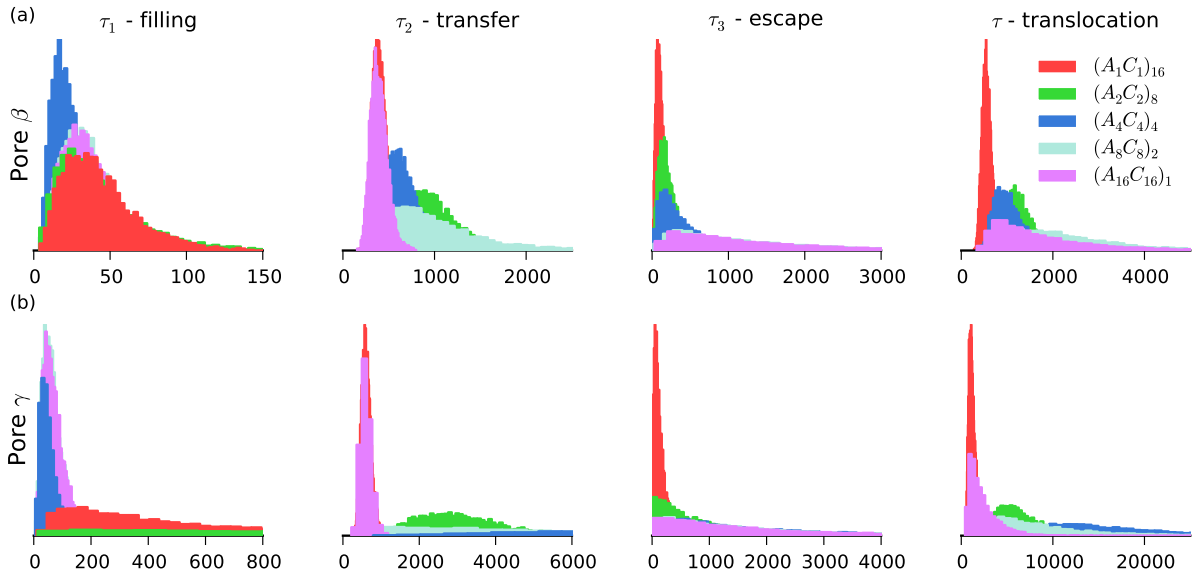

FIGURE 7.8: Translocation distributions for five block co-polymers.

translocating ssDNA interacts instead with the DNA origami backbone (BB), such as A-BB and C-BB, see Figure 7.7.

The simulation results for five different sequences corresponding to $n = 1, 2, 4, 8$ and 16 are shown for Pore β and Pore γ in Figure 7.8 sub panels a) and b), respectively. It can be seen that the different translocation intervals respond differently to both block length and pore type such that the overall translocation time distributions are quite distinct. In order to present this data in a more informative way we summarise the distributions for each sequence in a scatter plot using only the mean and standard deviation, see Figure 7.9.

An interesting trend is observed between block length and the distribution moments for both pores. For Pore β the mean and standard deviation seem to increase up to $n = 8$ and then reverse, although this does not hold for $n = 2$ and $n = 4$. For Pore γ a similar trend can be seen up to $n = 4$ and holds in the mean for $N = 32$ and $N = 64$ and the standard deviation for $N = 32$, but the AC orientation of $n = 16$ in $N = 32$ breaks this pattern.

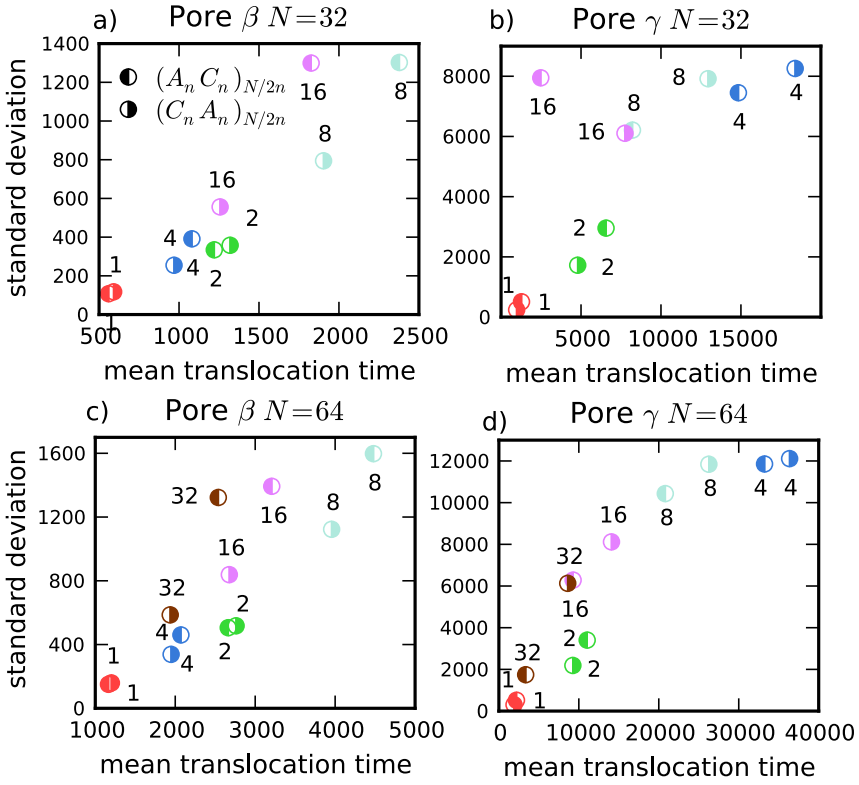

FIGURE 7.9: The translocation time distributions for each pore and sequence are simplified into the mean and standard deviation. The results have been grouped by pore and nucleotide length, N, with each scatter point representing a unique sequence. The numeric label next to each point represents the value of n. The results for different entry orientations are marked by half filled circles.

Returning to the hard rod model these features can be easily explained. Considering Pore β and AC type orientations only, see Figure 7.9 a), the hard rod model, see Figure 7.10, shows that although sequences $n = 2$ and $n = 4$ are similar, a crucial difference occurs between the two. After translocation event s_1, sequence $n = 4$ has a series of minima up to its peak. These binding sites improve the chances of forward movement. Sequence $n = 2$ on the other hand has a large barrier to cross from s_1 to the next binding site, appearing to have one site missing as compared to $n = 4$. This barrier reduces the probability of forward movement resulting in a longer mean translocation time. Sequence $n = 8$ has to cross a similar barrier to $n = 16$, however it must do this twice before translocation, resulting in a translocation time that is roughly twice as long. The asymmetry between (s_0, s_1) and (s_2, s_3) explains the importance of orientation.

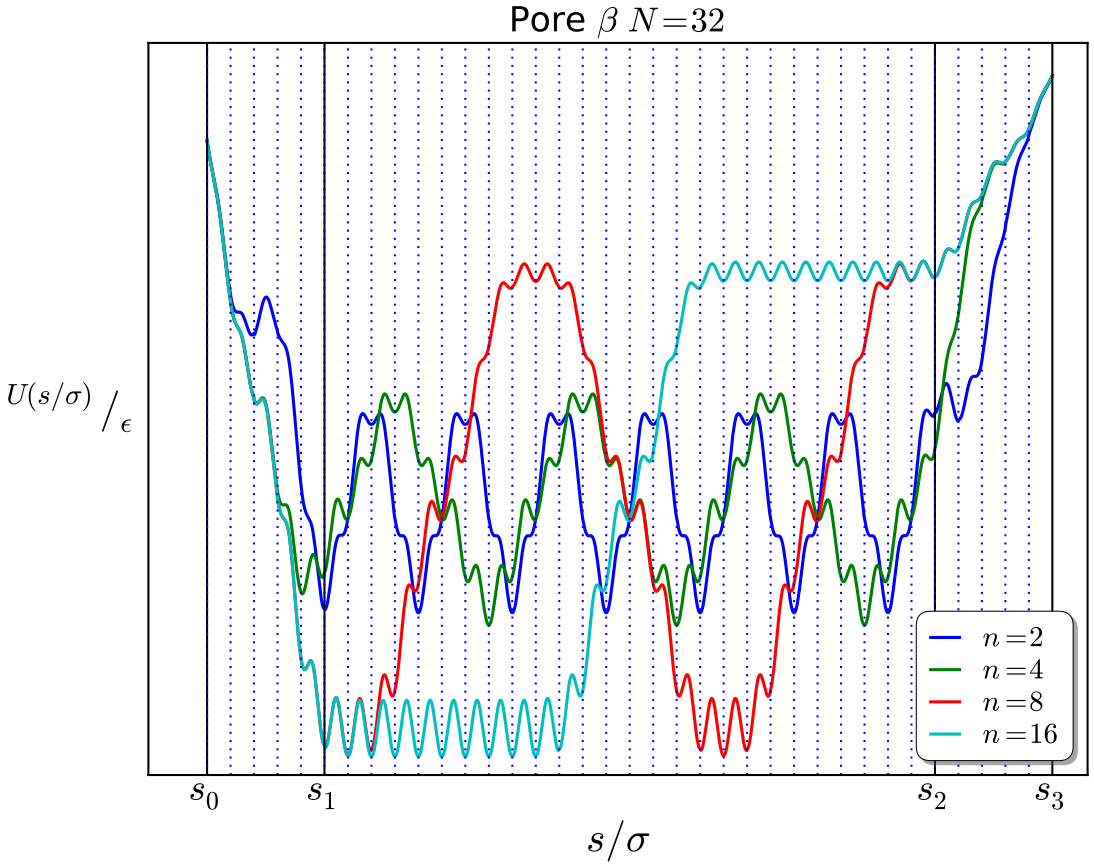

FIGURE 7.10: Interaction potential obtained from the hard rod model with sequence $(\mathrm{A_nC_n})_{\mathrm{N/2n}}$ without a driving force.

The scatter plots of Figure 7.9 most clearly indicate the *distinguishability* of each sequence. The closer the scatter points are the less distinguishable their distributions. Pore β cannot easily distinguish between $(\mathrm{A_4C_4})_4$ and $(\mathrm{A_2C_2})_8$, see Figure 7.9 a), while Pore γ can, see Figure 7.9 c). The reverse is true for $(\mathrm{A_4C_4})_4$ and $(A_8C_8)_8$. This suggests that combining translocation time measurements across the two pores could help identify an unknown sequence.

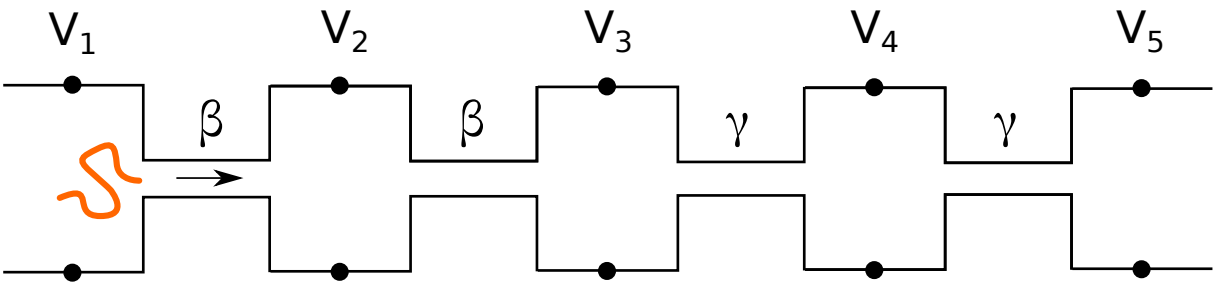

FIGURE 7.11: Schematic of multipore sensing system. Here $m = 2$ and two Pore βs are in series with two Pore γs. Multiple translocation time measurements are made for a single polymer.

7.5 Stochastic sensing

7.5.1 Model device

To demonstrate the idea of using multiple pores in identifying an unknown sequence we run a test on a model sensing device. We consider a device that consists of m Pore βs in series with the same number of Pore γs such that m measurements are taken from each pore type and $2m$ measurements are made in total. The pores connect to chambers which we assume to be much larger than the radius of gyration of the polymer such that each pore is independent from the last allowing the possibility of a flip in orientation before the next translocation, see Figure 7.11.

Across each pore is a pair of electrodes giving $2m + 1$ electrodes in total. The voltage applied across electrode i and $i + 1$ sets the driving force across the pore. In order to consecutively drive the polymer through each pore we constrain the voltages to satisfy $V_1 < V_2 < V_3 ... < V_{2m+1}$, where the potential difference across each pore need not be constant, allowing different driving forces. The current measurement across each electrode pair gives the total translocation time, τ_i, through pore i.

As an alternative to this, one could consider just two pores with three electrodes that reverse polarity on detection of a successful translocation to 'shuttle' the subject strand

back and forth across the pore to make multiple measurements. In this case the asymmetry of the pore would be important and an odd number of measurements is required in order to progress the chain forward. We do not consider the effect of reversing the pore orientation in what follows and so the model described previously will be considered.

7.5.2 Algorithms

We consider two algorithms for stochastic sensing. These algorithms are based on prior knowledge of the pore statistics. In practice this could be gained from a one time calibration of the system. Here we use the distributions obtained from the simulations. For the first method we consider only the mean and standard deviation and in the second we use the full distribution.

7.5.2.1 Moment method

For the moment method, we calculate the mean and standard deviation from the $m \geq 2$ measured translocation times through pore p to obtain the vector $\vec{u}_m^p = (\tau_m^p, \sigma_m^p) = (N^{-1}\sum_{i=1}^m \tau_i, \sqrt{N^{-1}\sum_{i=1}^m [\tau_i - \tau_m^p]})$. We compare these measured values to known means and standard deviations for each pore and sequence, $\vec{u}_n^p = (\tau_n^p, \sigma_n^p)$, where n refers to the sequence, using the following relative error metric

$$\Delta(\vec{u}_m^p, \vec{u}_n^p) = \sqrt{\left(\frac{\tau_m^p - \tau_n^p}{\tau_n^p}\right)^2 + \left(\frac{\sigma_m^p - \sigma_n^p}{\sigma_m^p}\right)^2} \tag{7.1}$$

We sum this value across the pores to calculate the relative error for the measured sequence against sequence n, $\Delta_{m,n} = \sum_{p=\{\beta,\gamma\}} \Delta(\vec{u}_m^p, \vec{u}_n^p)$. The most likely sequence is given by the sequence that minimises $\Delta_{m,n}$ across all n, seq $\equiv$ seq[min$\{\Delta_{\mathrm{m,n}}\}$]. When applying this algorithm we consider only a fixed orientation.

7.5.2.2 Distribution method

Instead of using only the mean and standard deviation we can choose to use the known full distribution, $\mathcal{P}_n^p(\tau)$. Considering first a single orientation, we can construct the likelihood of the m measured values belonging to the distribution of sequence n through the pore p as $\mathcal{L}_n^p = \Pi_{i=1}^m \mathcal{P}_n^p(\tau_i)$. For multiple pore types we find the likelihood across pores by $\mathcal{L}_n = \Pi_{p\in\{\alpha,\beta\}}\mathcal{L}_n^p$. The mostly likely structure of the unknown polymer is given by the sequence that maximises the likelihood, $\mathrm{seq} \equiv \mathrm{seq}[\max\{\mathcal{L}_\mathrm{n}\}]$.

When considering random entry orientations it is not known which distribution the measured values belong to out of $\mathcal{P}_{n,o}^p$, where $o \in \{A, C\}$, corresponding to an A or C leading entry. For example, two measurements τ_1 and τ_2 could correspond to any of the four possible orientations AC, AA, CA and CC. To evaluate the likelihood we sum over all permutations of the measurements $\mathcal{L}_n^p = \sum_{\mathrm{perm[o]}} \Pi_{i=1}^m \mathcal{P}_{n,o}^p$. This can be intuitively understood as a search for the correct set of orientations, returning a high likelihood, all other incorrect permutations should contribute a very small partial likelihood. In order to combine measurements over multiple pore types we perform the same operation as before, $\mathcal{L}_n = \Pi_{p\in\{\alpha,\beta\}}\mathcal{L}_n^p$.

7.5.2.3 Accuracy

We define the accuracy of the sensing algorithms as the ratio of the number of successful sequence identifications to the total number of attempts, and turns out to be remarkably high, see Figure 7.12.

For fixed orientations, a completely unintelligent sensing algorithm would achieve an accuracy of $1/N_\mathrm{seq}$ where N_seq is the number of sequences to be identified. The accuracy for the full distribution method begins at 70% and for the moment method at 75% with a minimum of 1 and 2 measurements per pore type, respectively. The accuracy quickly

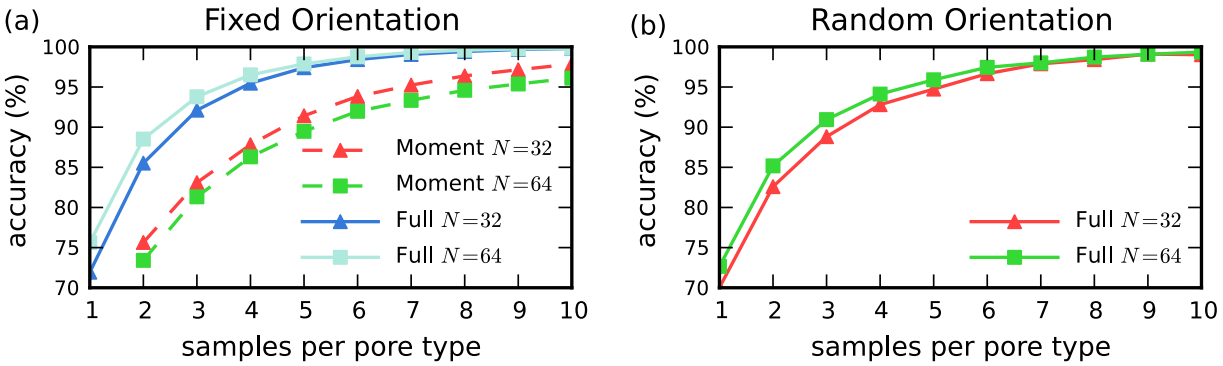

FIGURE 7.12: Schematic of multipore sensing system. Here $m = 2$ and two Pore βs are in series with two Pore γs. Multiple translocation time reads are made for a single polymer.

increases with the number of measurements with the full distribution method attaining very high accuracy.

When considering randomised orientations in the full distribution method the accuracy remains robust. Where 95% accuracy was obtained for fixed orientations with 4 samples per pore this accuracy can be matched considering random orientations with just 5 samples per pore.

This shows that these methods do indeed perform intelligent stochastic sequencing. The moment method is less computationally demanding, but has weaker performance compared with the full distribution method.

7.6 Conclusions and future outlook

In this chapter we have considered the effect of pore patterning on translocation dynamics through numerical investigation amounting to 100,000s of individual simulation runs. We began by characterising the impact of pore patterning on the three translocation periods for a homopolymer: filling, transfer and escape. It was seen that the interaction potential obtained from the hard model is helpful in explaining these features. The Lubensky-Nelson distribution was also found to fit the transfer distributions accurately. This could provide a

method of reducing the complex form of the distribution down to two parameters, r and κ. We extended this investigation to consider a set of block co-polymer sequences of the form $(\mathrm{A_nC_n})_{\mathrm{N/2n}}$. The hard rod model once again proved useful in understanding the differing translocation time scales between sequences. From the promising distinguishability seen across sequences by combining different pore types we proposed a model device, and applied two simple algorithms for stochastic sensing. These algorithms returned a high accuracy, suggesting stochastic sensing as a viable approach.

A promising future direction for this research would be to construct approximate analytical forms for the hard rod interaction potential taking into account pore patterning and sequence. Indeed, it seems the regular forms of the potentials could be produced with only a few components. One line of investigation could be to use this understanding to construct a lattice model of translocation with hops between predicted binding sites. This would provide useful information on the modulation on translocation time for sequencing that would be useful in all sequencing methods.

During the transfer period the potential takes a periodic form, suggesting an analysis similar to the Lubensky-Nelson study could be used to calculate the translocation time distribution. For another research direction, an accurate description of the process could be obtained by combining the hard rod interaction potential, the Lubensky-Nelson analysis and considering modifications to the dynamical friction coefficient from non-equilibrium translocation. This would, in essence, provide a mapping between sequence and distribution parameters, seq $\rightarrow \mathcal{P}(\tau)$, corroborated by, but obtained independently of, simulation. Using such a mapping this research could be extended to investigate a wide range of pore patterns and sequences with potential for increased polymer length.

When considering sequencing, any method that requires sequence dependent information for identification has severe limitations, as even with a short strand of $N = 32$ this amounts to an astronomical $4^{32} \sim 10^{19}$ combinations. The moment space picture of Figure

7.9 would quickly become over saturated and kill the identification accuracy. However, for a small sample set involving counting, separation or sorting of a known mixture the technique described here could be highly effective.

Stochastic, or noisy, sensing is an interesting principle in itself with wide applications to many fields. As with many things at the mesoscale, biology has already perfected the art of stochastic sensing and our knowledge of these principles can be developed further by studying its solutions [110].

Chapter 8

Active pores

Corresponding publications:

- J. A. Cohen, A. Chaudhuri and R. Golestanian,
  Active Polymer Translocation through Flickering Pores,
  Physical Review Letters **107**, 238102 (2011)
- J. A. Cohen, A. Chaudhuri and R. Golestanian,
  Translocation through environments with time dependent mobility,
  Journal of Chemical Physics **137**, 204911 (2012)

8.1 Introduction

Until recently [111, 112], translocation has only been considered through static, non time-dependent, environments. It is interesting to ask how dynamically changing conditions could affect translocation efficiency and if any information about the polymer could be inferred from its response.

There are many examples in biological systems where channels show active 'gating' or flickering between open and closed states (Mitochondria). Active processes can also change the conditions or conformation of the biological channel, such as in the nuclear pore where polymer brushes are thought to contract or expand due to translocation factors, or in the

relative subunit rotation of ribosome during transcription. It is becoming increasingly common to model proteins as a collection of continuous elastic elements reflecting the flexibility of protein structures at certain points. Under thermal fluctuations this elasticity could allow channel cross sections to fluctuate in time. A recent experiment has begun to investigate translocation through artificial active systems by applying mechanical stress to induce shape changes in a flexible elastic channel [113].

We explore these ideas by extending the numerical model of the previous section to allow the pore width to oscillate during the translocation process. This adds another time scale that could be used to probe polymer relaxation dynamics and provide interesting tests for the robustness of non-equilibrium translocation theory.

We will investigate the change in translocation time for translocation through periodic time dependent environments, τ_{osc}, as compared to static translocation, τ_{stat}, using the gain $\eta(\omega) = \tau_{\text{stat}}/\tau_{\text{osc}}(\omega)$ and an oscillation frequency ω. We will proceed by first performing analysis on single particle translocation, reducing the problem to time dependent mobilities in both diffusive and non-diffusive situations. Then, using Langevin Dynamics simulations as described in Section 6.4, we will investigate the effect of periodic variation of the pore geometry on polymer translocation and compare the results to the single particle analysis.

8.2 Time dependent mobilities

It is common to project the polymer translocation process down to a single coordinate producing an effective single particle description. The friction coefficient of this single particle representation is likely to depend on the stage of the translocation process, as mentioned in the introductory section on non-equilibrium translocation, however we neglect this contribution here. Instead, our focus is to obtain the translocation time distribution,

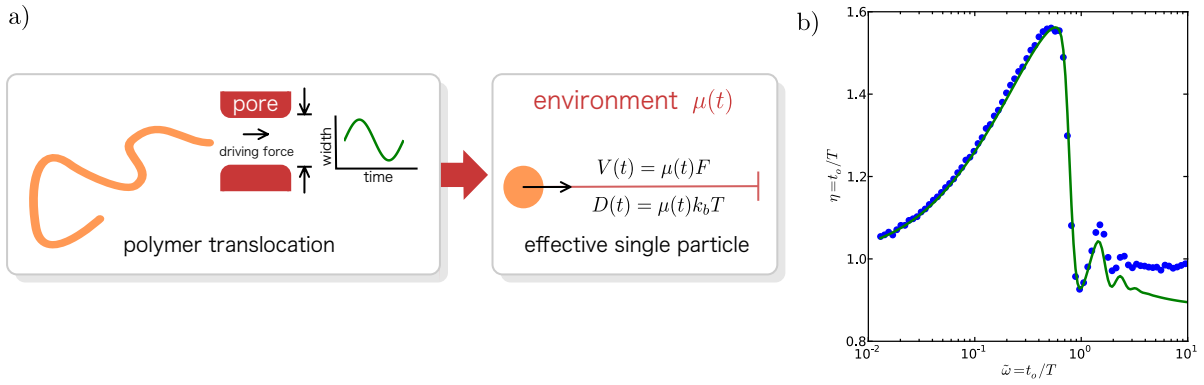

FIGURE 8.1: a) The time taken for a polymer to move through a pore with a width that is changing harmonically in time is dependent on the frequency of the oscillation. In order to better understand this process we present an effective description of the translocation dynamics using a Fokker-Plank description with a time dependent mobility. We develop the idea of single particle time dependent mobilities in a general setting to allow for greater applicability to other soft matter systems. b) The scaled frequency response for the gain in polymer translocation time from simulations (dots) is reproduced well at low frequencies by the effective single particle description (solid line) . However, at higher frequencies the response is only matched qualitatively. This is shown for simulation parameters $N = 128$, $\epsilon = 1$ and $F = 1$ with a width that varies between 2.0σ and 2.5σ sinusoidally where σ is the particle diameter. The reference time t_o is chosen to to be the translocation time at $W = 2.25\sigma$.

or first passage distribution, in the presence of time dependent confinement and look at the frequency response of the gain in translocation time. This will later be compared to simulation results. The system under consideration and its projection to one-coordinate is illustrated in Figure 8.1 a) and the comparison of the final expression for the frequency of the gain constructed in this chapter to the simulation is shown in Figure 8.1 b). The rest of this chapter will describe the analysis leading to this result.

The single particle probability distribution in the presence of time dependent confinement will follow the Smoluchowski equation

$$\frac{\partial p(x,t)}{\partial t} = -\frac{\partial}{\partial x}\left[-D\frac{\partial p(x,t)}{\partial x} - \zeta^{-1}\frac{\partial \Phi(x,t)}{\partial x}p(x,t)\right] \tag{8.1}$$

where $\Phi(x,t) = U(x,t) - Fx$ is a space and time dependent potential with a constant driving force F. We consider the form $U(x,t) = u(x)s(t)$ where $u(x) = u(x+\sigma)$ is periodic in the base length and $s(t) = [1 + f(t)]$ modulates the amplitude of the potential in time.

Such a description is known as a fluctuating potential [114] and follows naturally from the consideration of the hard rod interaction potential in the previous section. The function $f(t)$ represents changes in the confinement, such as a time dependent pore size, affecting polymer-surface interactions and we consider $f(t) \ll 1$ such that $s(t)$ is always non-zero.

This equation is difficult to solve due to the time dependence of $\Phi(x,t)$ making the Smoluchowski operator $\mathcal{L}(t) = \partial_x(D\partial_x - \zeta^{-1}\partial_x\Phi(x,t))$ time dependent. Instead, we simplify the picture by considering effective diffusion and drift velocities due to the time dependent potential. If we assume their ratio is independent of time we can instead assign a time dependent mobility, $\mu(t)$, such that $V = \mu(t)F$ and $D = \mu(t)k_BT$, which will greatly simplify the solution. We assume that a time dependent change in interaction potential can be represented as an effective time dependent friction, or mobility, for polymer translocation. We will now outline a justification for this.

For the limit of energetic barriers larger than the thermal energy we can consider the transport process as a thermally activated barrier crossing with forward hopping rate k_+, and backwards hopping rate k_-. The effective diffusion coefficient will be given by $D = \sigma^2(k_+ + k_-)/2$ and the effective drift velocity $V = \sigma(k_+ - k_-)$, where $k_+ > k_-$ due to the driving force. The hopping rates will be proportional to the barrier size $k_\pm \propto \exp(-\beta[s_A(t) \mp F\sigma/2])$. The ratio between diffusion and advection, $\kappa = D(t)/V(t)L$, becomes independent of time, due to cancellation of the time dependent exponential terms. Since the Kramer's escape rate used above depends upon a quasi-static probability distribution, the period of oscillation must be much longer than the time taken for translocation. This limits the validity of this analysis to low oscillation frequencies. However, there may be many other situations where a time dependent mobility can be used to describe the dynamics of a system, such as frictional changes in response to external fields, and so we proceed assuming we can describe the diffusion and drift velocity with a time dependent mobility.

We will begin in Section 8.2.1 by constructing the frequency response of the gain for the elementary cases of two-state (open or closed) confinement and general periodic confinement without diffusion, applying the general prescription to two further cases of sawtooth and sinusoidal variations. These will serve as simple references cases for investigating the frequency response of the gain with respect to oscillating confinements. We will include the effect of diffusion in Section 8.2.2 and find an analytical expression for the frequency response of the gain for two-state confinement and derive a general expression for the translocation time distribution for any time dependent mobility. We will conclude the diffusive section by a comparison of the translocation time distribution between a simple numerical solution and the analytical expression for sinusoidal variations.

8.2.1 Non-diffusive

8.2.1.1 Two-state

We first consider a situation where a particle under the influence of a constant driving force in one dimension experiences a two state confinement: a state where it is able to move with constant velocity (V_{on}) and the other where it is stuck with zero velocity ($V_{\text{off}} = 0$). Therefore, the mobility switches between a constant value (μ_{on}) and zero. This could occur, for example, if a charged colloid moves due to an external electric field through a long channel that becomes strongly oppositely charged, or the channel is mechanically compressed in a transverse direction, such that the colloid is temporarily fixed to the surface without the possibility of slipping. Since the durations of the on (t_{on}) and off (t_{off}) states of confinement need not be symmetric, we define the asymmetry parameter $a = t_{\text{off}}/t_{\text{on}}$ over the period $T = t_{\text{on}} + t_{\text{off}}$. To analyse the dynamics, we look at the efficiency of the translocation process by comparing the time taken for the particle to traverse a distance L in the presence of this oscillatory two-state confinement, $t_{\text{osc}}(\tilde{\omega})$, to

one where the particle moves unhindered with a velocity equal to the average over an oscillation period with symmetric off and on durations, $t_0 = \langle t \rangle_{T,a=1}$. This efficiency is defined as the gain in translocation rate

$$\eta(\tilde{\omega}) \quad = \quad \frac{t_0}{t_{\rm osc}(\tilde{\omega})} \tag{8.2}$$

where T is the time period of oscillation and $\tilde{\omega} = t_0/T$ is a dimensionless frequency. The average velocity of the particle in peroid T with $a = 1$ is $\langle V \rangle_{T,a=1} = V_{\rm on}/2$, and so $t_0 = 2L/V_{\rm on}$.

The time taken by the particle to translocate a distance L is

$$t_{\rm osc} \quad = \quad N_{\rm off} t_{\rm off} + N_{\rm on} t_{\rm on} \tag{8.3}$$

where $N_{\rm off}$ and $N_{\rm on}$ are the number of off and on cycles respectively. Note that since the particle only moves in the on state, $N_{\rm on}$ can be fractional while $N_{\rm off}$ is an integer. Also, $L = V_{\rm on} N_{\rm on} t_{\rm on}$ which implies, $t_0 = 2N_{\rm on} t_{\rm on}$. Using these relationships we can express the gain as a function of the number of 'off' to 'on' cycles as,

$$\eta \quad = \quad 2\left[1 + a\frac{N_{\rm off}}{N_{\rm on}}\right]^{-1} \tag{8.4}$$

We can rewrite η in a continuum form by expressing the off cycles as $N_{\rm off} = \mathcal{S}(N_{\rm on})$, where $\mathcal{S}(x)$ is the unit staircase function and returns the integer value of x. The staircase

function has the following relationships

$$\begin{aligned}
\mathcal{S}(x) &= \lfloor x \rfloor && (8.5)\\
&= \sum_{n=1}^{\infty} \Theta(x-n) && (8.6)\\
\int_0^y \mathcal{S}(x)dx &= \frac{\mathcal{S}^2(y-1)}{2} + \frac{\mathcal{S}(y-1)}{2} + y\mathcal{S}(y) && (8.7)\\
&- \mathcal{S}^2(y)\\
\frac{d\mathcal{S}(x)}{dx} &= \sum_{n=1}^{\infty} \delta(x-n) && (8.8)\\
\lim_{a\to\infty} \mathcal{S}(ax) &= ax && (8.9)
\end{aligned}$$

Since $N_{\text{on}} = \tilde{\omega}$, we have

$$\eta(\tilde{\omega}) = 2\left[1 + \frac{2a}{1+a}\frac{\mathcal{S}((1+a)\tilde{\omega}/2)}{\tilde{\omega}}\right]^{-1} \quad (8.10)$$

For any value of a the gain is at a maximum when $N_{\text{off}} = N_{\text{on}} - 1$ and at a minimum when $N_{\text{off}} = N_{\text{on}}$, as shown in see Figure 8.2a). For symmetric cycles the gain takes the simple form $\eta(\tilde{\omega}) = 2\left[1 + \frac{\mathcal{S}(\tilde{\omega})}{\tilde{\omega}}\right]^{-1}$ with maximum $\eta_{\max}(\tilde{\omega}) = 2\tilde{\omega}/(2\tilde{\omega}-1)$ and minimum $\eta_{\min} = 1$. We also note that $\eta(\tilde{\omega} \to \infty) \to 2/(1+a)$.

8.2.1.2 General periodic

It is possible to generalise the process of obtaining the frequency response of the gain for any periodic time dependent mobility, $\mu(t)$, in the presence of the constant driving force, F. In this section we will describe the process and then we will apply it to two examples in the following sections. We begin by splitting the total oscillating translocation time into two parts

$$t_{\text{osc}} = t'_{\text{osc}} + \Delta t_{\text{osc}} \quad (8.11)$$

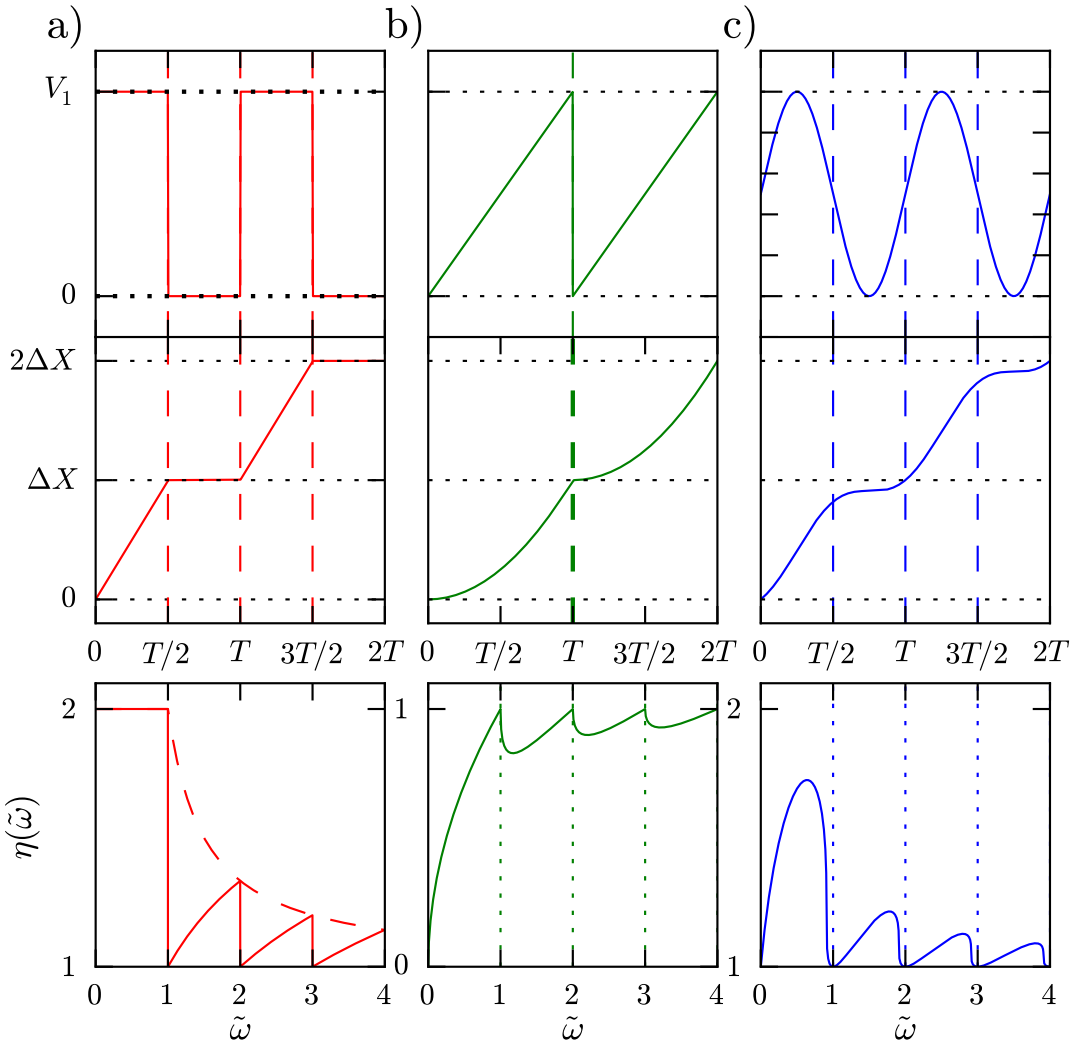

FIGURE 8.2: Time dependent velocity (top) and position (vertical middle) as a function of the time period of oscillation for (a) two state (b) sawtooth and (c) sinusoidal mobilities. (Bottom) Frequency response of the gain. The gain is shown for four dimensionless frequencies.

where $t_{\text{osc}'}$ is the translocation time of the particle for N_c complete cycles and Δt_{osc} is the translocation time in the remaining partial cycle required to complete the translocation event for length L. Therefore, $t'_{\text{osc}} = N_c T$ where $N_c = \mathcal{S}\left(L/\Delta X\right)$ and $\Delta X = F\int_0^T \mu(t)dt$ is the distance traveled per cycle. The average velocity per cycle is $\langle V\rangle_T = \Delta X/T$ and so $\langle t\rangle_T = L/\langle V\rangle_T = LT/\Delta X$ and $\tilde{\omega} = \langle t\rangle_T/T = L/\Delta X$. Assimilating these relationships we

have

$$t'_{\rm osc} = \frac{\mathcal{S}\left(\tilde{\omega}\right)}{\tilde{\omega}}\langle t\rangle_T \tag{8.12}$$

After traversing over N_c complete cycles of time periodic confinement, the remaining distance required to translocate will be $\Delta L = L - N_c\Delta X$. In dimensionless units we have

$$\Delta\tilde{L} = \frac{\Delta L}{L} = 1 - \frac{\mathcal{S}(\tilde{\omega})}{\tilde{\omega}} \tag{8.13}$$

The distance travelled in time $t < T$ is $X(t) = F\int_0^t \mu(t)dt$ and the partial translocation time is obtained when the condition $X(\Delta t_{\rm osc}) = \Delta L$ is satisfied. Therefore, we need to solve the inverse problem to obtain $\Delta t_{\rm osc}(X = \Delta L)$. In dimensionless units, $\Delta t_{\rm osc} = \Delta t_{\rm osc}(\Delta\tilde{L}) = \Delta\tilde{t}_{\rm osc}(\Delta\tilde{L})\langle t\rangle_T$. The general formula for gain can now be expressed as

$$\eta(\tilde{\omega}) = \left[\frac{\mathcal{S}\left(\tilde{\omega}\right)}{\tilde{\omega}} + \Delta\tilde{t}_{\rm osc}\left(1 - \frac{\mathcal{S}(\tilde{\omega})}{\tilde{\omega}}\right)\right]^{-1} \tag{8.14}$$

where $\Delta\tilde{t}_{\rm osc}(\Delta L)$ is the time needed to translate the remaining distance, ΔL, occurring after the complete cycles.

8.2.1.3 Sawtooth

For the case of a simple sawtooth mobility $\mu(t) = \mu_0 t/T$, the average velocity being $\langle V\rangle_T = \mu_0 F/2$, where μ_0 is a constant amplitude. Therefore, $\tilde{X}(\tilde{t}) = \tilde{\omega}\tilde{t}^2$ and $\Delta\tilde{t}_{\rm osc}(\tilde{X}) = (\tilde{X}/\tilde{\omega})^{1/2}$ with gain

$$\eta(\tilde{\omega}) = \frac{\tilde{\omega}}{\mathcal{S}\left(\tilde{\omega}\right) + \sqrt{\tilde{\omega} - \mathcal{S}(\tilde{\omega})}} \tag{8.15}$$

The minimums occur at $\tilde{\omega} = 2(n + n^2 - \sqrt{n^3 + n^4})$ for period $n > 0 \in \mathbb{Z}$ and maximums $\eta_{\max} = 1$ for $\tilde{\omega} = n$ as shown in Figure 8.2b).

8.2.1.4 Sinusoidal

For an oscillating confinement giving rise to a sinusoidal mobility as $\mu(t) = \mu_0(1 + \sin(2\pi t/T))/2$, the average velocity over a period is $\langle V \rangle_T = \mu_0 F/2$. In this case, $\tilde{X}(\tilde{t}) = \tilde{t} + (1 - \cos(2\pi\tilde{\omega}\tilde{t}))/(2\pi\omega)$ with $\tilde{X}(0) = 0$. Thus to solve for $\Delta\tilde{t}_{\text{osc}}$, we need to solve a transcendental equation, which we do numerically. The gain plots are shown in Figure 8.2c).

8.2.2 Diffusive

8.2.2.1 General

We now incorporate the effect of diffusion in the translocation dynamics of a particle experiencing time dependent confinement. We consider a particle in 1D initially located at distance L from an absorbing barrier at the origin. An external force drives the particle towards the barrier with a drift velocity $V = \mu(t)F$. The particle traverses the distance L before absorption and during this process we assume it experiences a time dependent confinement that manifests in the diffusion coefficient instantly as $D = \mu(t)k_bT$.

We first study the case of a general confinement and determine the first passage time distribution, from which we can obtain the translocation time as first mean passage time. Then we study specific cases and look at the frequency response of the gain $\eta(\tilde{\omega})$ in the translocation process and finally compare with our previous study to investigate the effect of diffusion.

To do so, we write down the Fokker-Planck equation for this process as

$$\frac{\partial p}{\partial t} = \mu(t)\left(k_b T\frac{\partial^2 p}{\partial x^2} + F\frac{\partial p}{\partial x}\right) \tag{8.16}$$

Choosing L, L/V and μ_0 for the units of length, time and mobility we can rewrite this equation in dimensionless parameter form

$$\frac{\partial p}{\partial \tilde{t}} = \tilde{\mu}(t)\left(\tilde{f}^{-1}\frac{\partial^2 p}{\partial \tilde{x}^2} + \frac{\partial p}{\partial \tilde{x}}\right). \tag{8.17}$$

$\tilde{f} = \kappa^{-1} = LV/D = FL/k_bT$ is a dimensionless force measuring the work done against thermal energy, with the effect of diffusion reducing with increasing $\tilde{f}$, and $\mu_0 = \mu_{\tilde{\omega}=0}$ is some reference mobility chosen to be the mobility when the confinement is static. The positivity of the drift term is a result of the force being directed towards the origin from an initial position L. This equation can be transformed to the time independent mobility form by a change of variable $p(\tilde{x}, \tau(\tilde{t}))$ [115] where

$$\tau(\tilde{t}) = \int_0^{\tilde{t}} \tilde{\mu}(\tilde{t}')d\tilde{t}' \tag{8.18}$$

The transformation yields

$$\frac{\partial p}{\partial \tau} = \tilde{f}^{-1}\frac{\partial^2 p}{\partial \tilde{x}^2} + \frac{\partial p}{\partial \tilde{x}} \tag{8.19}$$

This equation can be once more transformed into a drift free equation by the substitution $p(\tilde{x}, \tau) = q(\tilde{x}, \tau)w(\tilde{x})s(\tau)$ where $w = \exp\left(-\tilde{f}\,\tilde{x}/2\right)$ and $s = \exp\left(-\tilde{f}\,\tau/4\right)$ [116] giving

$$\frac{\partial q}{\partial \tau} = \tilde{f}^{-1}\frac{\partial^2 q}{\partial \tilde{w}^2} \tag{8.20}$$

The initial condition satisfying the absorbing boundary condition at the origin is now $q(x, 0) = \exp(\tilde{f}\,L/2)(\delta(x - L) - \delta(x + L))$. Solving for q, transforming to p, making the

change of variable, $\tau(\tilde{t})$, and a little rearrangement leads to

$$\tilde{p}(\tilde{x},\tilde{t}|1) = \frac{e^{-\frac{(\tilde{x}-1+\tau(\tilde{t}))^2}{4\tilde{f}^{-1}\tau(\tilde{t})}} - e^{\tilde{f}}e^{-\frac{(\tilde{x}+1+\tau(\tilde{t}))^2}{4\tilde{f}^{-1}\tau(\tilde{t})}}}{\sqrt{4\pi\tilde{f}^{-1}\tau(\tilde{t})}} \tag{8.21}$$

Defining the survival probability, $\tilde{P}(\tilde{t}) = \int_0^\infty p(\tilde{x},\tilde{t})d\tilde{x}$, we find

$$\tilde{P}(\tilde{t}) = \frac{1}{2}\left[\text{erfc}\left(\frac{\tau(\tilde{t})-1}{\sqrt{4\tilde{f}^{-1}\tau(\tilde{t})}}\right) - e^{\tilde{f}}\text{erfc}\left(\frac{\tau(\tilde{t})+1}{\sqrt{4\tilde{f}^{-1}\tau(\tilde{t})}}\right)\right]$$

with the first passage time distribution $\tilde{\rho} = -\partial_{\tilde{t}}\tilde{P}(\tilde{t})$, as

$$\tilde{\rho}(\tilde{t}) = \frac{\tilde{\mu}(\tilde{t})}{\sqrt{4\pi\tilde{f}^{-1}\tilde{\tau}(\tilde{t})^3}}\exp\left(-\frac{(1-\tau(\tilde{t}))^2}{4\tilde{f}^{-1}\tau(\tilde{t})}\right) \tag{8.22}$$

The translocation time is obtained as the mean first passage time, $\langle\tilde{t}\rangle = \int_0^\infty \tilde{t}\tilde{\rho}(\tilde{t})d\tilde{t}$. For the special case of time independent mobility we have $\tilde{\mu} = 1$ and $\tilde{\tau}(\tilde{t}) = \tilde{t}$ and in rescaled units the mean first passage time takes the convenient form $\langle\tilde{t}\rangle = 1$.

8.2.2.2 Two-state

For the two state confinement case the mobility either take values $\mu_{\text{off}} = 0$ or $\mu_{\text{on}} \neq 0$. During periods of zero mobility the particle will be stationary without diffusion and there will be exclusion regions of zero probability in the first passage distribution. In terms of (8.22) the mobility will take on the form of a periodic square wave, as in Figure 8.2a). Integration of the square wave mobility gives the effective time τ, which experiences plateaus corresponding to 'freezing', or effective time passing with zero rate during the off cycle. In this specific case we can map the non-oscillating first passage distribution onto the oscillating distribution by insertion of these exclusion regions with the appropriate

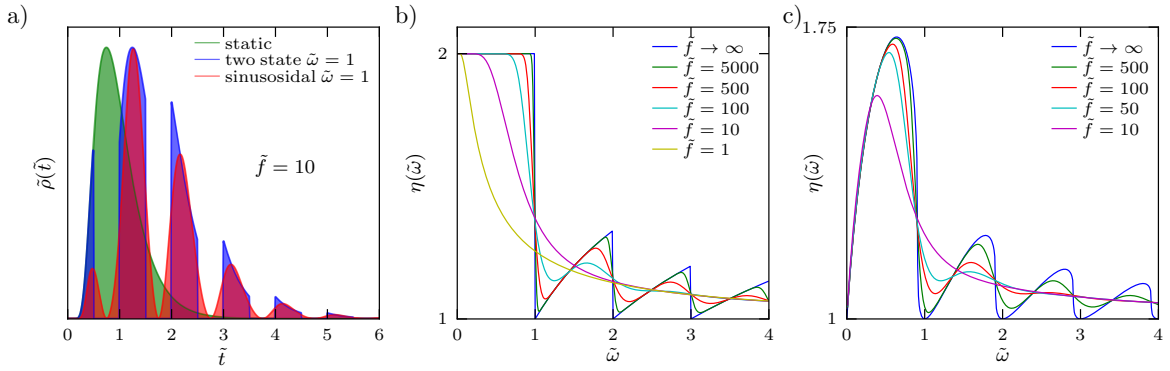

FIGURE 8.3: a) Comparison of first passage time distributions for static non oscillating confinement, two state confinement and sinusoidal confinement with dimensionless frequency $\tilde{\omega} = 1$ at $\tilde{f} = 10$ using (8.22) with the corresponding time dependent mobilities. b) Frequency response of the gain for two state confinement as given by (8.29). As $\tilde{f} \to \infty$ the frequency response matches that of the deterministic case as expected. At low $\tilde{f}$ the peaks become smoothed and are eventually washed out in the highly diffusive limit. c) The frequency response of the gain for sinusoidal confinement behaves similarly to the two state confinement. Both cases show an enhancement in translocation over the average velocity of each cycle.

shift in time.

$$\langle t \rangle_{\text{osc}} = \sum_{n=0}^{\infty} \int_{nt_{\text{on}}}^{(n+1)t_{\text{on}}} (t + nt_{\text{off}}) \rho(t) dt \tag{8.23}$$

$$= \langle t \rangle_{\text{static}} + t_{\text{off}} \sum_{n=0}^{\infty} \int_{nt_{\text{on}}}^{(n+1)t_{\text{on}}} n\rho(t) dt \tag{8.24}$$

where $\langle t \rangle_{\text{static}} = L/V_{\text{on}} = \langle t \rangle_T / 2$. The last integral may be written as a convolution with a staircase function $\mathcal{S}(x)$

$$\langle t_{\text{osc}} \rangle = \frac{\langle t \rangle_T}{2} + t_{\text{off}} \int_0^{\infty} \mathcal{S}\left(\frac{t}{t_{\text{on}}}\right) \rho(t) dt \tag{8.25}$$

Comparison to (8.3), suggests that the integral can be interpreted as the *average* number of off cycles before translocation

$$\langle N_{\text{off}} \rangle = \int_0^{\infty} \mathcal{S}\left(\frac{t}{t_{\text{on}}}\right) \rho(t) dt \tag{8.26}$$

Using integration by parts, noting that $\mathcal{S}(0) = 0$, $\mathcal{S}'(x) = \sum_{n=1}^{\infty} \delta(x-n)$ and the survival probability $P(t) \to 0$ as $t \to \infty$, we find

$$\langle N_{\rm off} \rangle = \sum_{n=1}^{\infty} P\left(n t_{\rm on}\right) \tag{8.27}$$

Now, as before we can let $a = t_{\rm off}/t_{\rm on}$ and $t_{\rm on} = \langle t \rangle_T / 2N_{\rm on}$ and rewrite (8.25) in terms of the gain

$$\eta = 2\left[1 + a\frac{\langle N_0 \rangle}{N_1}\right]^{-1} \tag{8.28}$$

Using the dimensionless form of the survival probability, $\tilde{P}(n\tilde{t}_{\rm on})$, we can express the gain as a function of $\tilde{\omega}$,

$$\eta(\tilde{\omega}) = 2\left[1 + \frac{2a}{(1+a)\tilde{\omega}} \sum_{n=1}^{\infty} \tilde{P}\left(\frac{2n}{(1+a)\tilde{\omega}}\right)\right]^{-1} \tag{8.29}$$

showing that the gain is a function of a, $\tilde{\omega}$ and $\tilde{f}$. Figure 8.3 shows clearly that there is substantial gain in the translocation process for finite oscillation frequencies when compared to static confinement with a mobility that is an average over a period of oscillation. The gain oscillates with the oscillation of the confinement decaying to 1 as $\omega \to \infty$. Thus, translocation in a time dependent confinement in the presence of a constant driving force, can enhance the translocation process at low frequencies, as compared to the cycle average, despite stationary periods. With higher $\tilde{f}$, the plot moves to the non-diffusive regime as expected. Note that for smaller $\tilde{f}$ the oscillations smoothen out. Diffusion cannot occur in the off periods due to zero mobility, however the diffusive behaviour in the on periods can cause translocations to complete at times around the deterministic time, smoothing the sharp drop that occurred at integer $\tilde{\omega}$. As the diffusion becomes dominant the first passage time distribution becomes broader, increasing the mean first passage time, which in turn decreases the gain. For a sinusoidal confinement, the situation is similar with

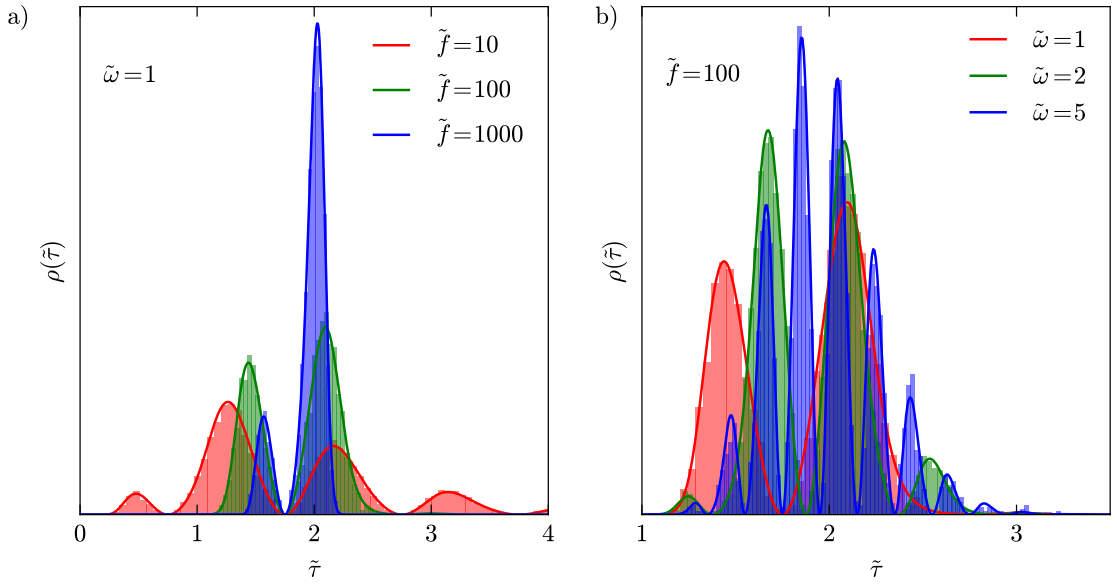

FIGURE 8.4: Comparison between the analytical result for first passage time with time dependent mobility (8.22) with the results from numerical integration of the corresponding differential equation (8.31). The analytical form is plotted by the bold solid line while the histogram of numerically obtained first passage times are shown by the filled areas. The mobility varies sinusoidally between zero and its maximum. The effect of varying the dimensionless force with constant number of oscillations per non-oscillating translocation time, $\tilde{\omega} = 1$, is shown in the top panel and the effect of increasing $\tilde{\omega}$ at constant $\tilde{f} = 100$ is shown in the bottom panel.

smoother oscillations than the two state confinement.

8.2.2.3 Numerical solution

We now compare the analytical result for the first passage time distribution (8.22), with numerical simulations. To do this, we numerically integrate the following stochastic equation of motion for a single particle,

$$\begin{aligned} dX &= V(t)dt + \sqrt{2D(t)dt}R(t) \\ &= \mu(t)Fdt + \sqrt{2\mu(t)k_bTdt}R(t) \end{aligned} \tag{8.30}$$

where $R(t)$ is a delta correlated white noise random number with unit variance. In dimensionless units, this becomes

$$d\tilde{X} = \tilde{\mu}(\tilde{t})d\tilde{t} + \sqrt{2\tilde{\mu}(\tilde{t})\tilde{f}^{-1}d\tilde{t}}R(t) \tag{8.31}$$

For sinusoidal confinement, we choose $\tilde{\mu}(\tilde{t}) = (1+\sin(2\pi\tilde{\omega}\tilde{t}))/2$ as in our analytics. Using this scheme, we evaluate the time taken by a particle to traverse a distance L with the given mobility. Using a number of simulation runs, we construct the translocation time distribution, which we compare with the first passage time distribution given by (8.22). The comparisons are made for a set of values of $\tilde{f}$ and $\tilde{\omega}$. In Figure 8.4 we show the effect of varying $\tilde{f}$ at constant $\tilde{\omega}$ and vice-versa. The results are in excellent agreement confirming the analytical result. Increasing the dimensionless force results in narrowing the distribution while keeping the number of minimums fixed. This is because at higher dimensionless force diffusion is limited. Increasing $\tilde{\omega}$ at constant $\tilde{f}$ splits the distribution into an increasing number of peaks.

8.3 Polymer translocation

Having looked at a single coordinate representation we now move to the case of polymer translocation through an oscillating nanopore.

8.3.1 Model

We model the polymer and the pore as in Section 6.4 but allow for the pore width to oscillate in time with an amplitude W_A about an average value W_0 as $W(t) = W_0 + W_A\sin(\omega t+\phi)$, where ϕ is the initial phase at arrival of the polymer to the pore and $\omega = 2\pi/T$ is the oscillation frequency with period T. The minimum and maximum

pore widths, $W_{\min} = W_0 - W_A$ and $W_{\min} = W_0 + W_A$, are selected to enforce single file translocation at all times, $W_{\max} \leq 3\sigma$, and so the smallest separation doesn't break the bonds between neighbouring monomers, $W_{\min} \geq 2$. We choose $W_0 = 2.25\sigma$ and $W_A = 0.25\sigma$ in accordance with these restrictions.

We prepare the polymer in an equilibrium conformation with its head monomer at the entrance of the pore, begin the simulation starting the oscillation from the initial phase ϕ and record the translocation time. We repeat this 2000 times for each parameter set in order to obtain sufficient statistics to investigate the translocation time distribution.

8.3.2 Results

We compare the oscillating mean translocation time, τ_{osc}, to the static translocation time, τ_{stat}, recorded at width $W = W_0$ using the gain $\eta(\tilde{\omega}) = \tau_{\text{stat}}/\tau_{\text{osc}}(\tilde{\omega})$ and the dimensionless frequency $\tilde{\omega} = \tau_{\text{stat}}/T$, which gives the number of oscillations required for a static translocation. We vary the affinity ϵ_{pm} and driving force F, see Figure 8.5.

It is seen that translocation is enhanced by oscillation as compared to the static pore with width $W = W_0$. Focusing first on cases where $\phi = 0$, two clear peaks can be seen at $\tilde{\omega} \sim 0.5$ and $\tilde{\omega} \sim 1.5$, with further peaks identifiable for the longer length $N = 128$ polymer, see Figure 8.5 a). The steady rise up to the peak at $\tilde{\omega} \sim 0.5$ corresponds to the pore width becoming increasingly wider with $\tilde{\omega}$ during translocation and acts to decrease the polymer-pore interaction and enhance translocation. This abruptly changes as $\tilde{\omega} \to 1$ and the oscillation frequency becomes fast enough to experience the first 'close' cycle between $T/2$ and T. Subsequent peaks ensue at half integer $\tilde{\omega}$ corresponding to the occurrence of open cycles but are damped by noise as seen from the single coordinate analysis, for example see Figure 8.3, causing the gain to plateau.

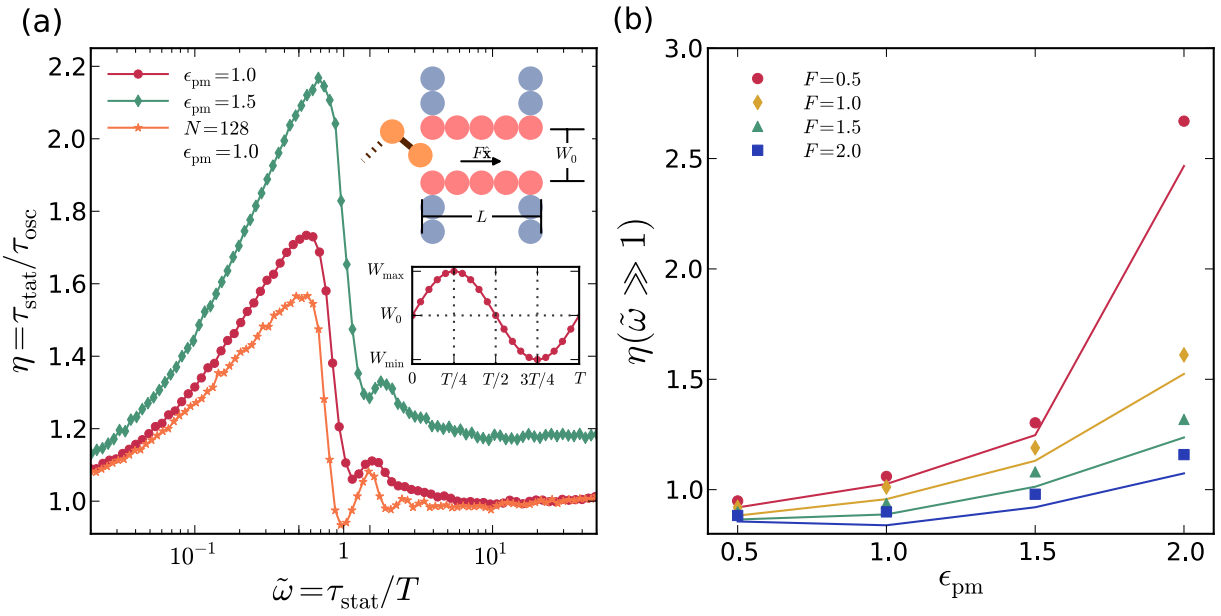

FIGURE 8.5: (a) Gain as a function of the scaled frequency, for $F = 1.0$, $N = 32$ (red and green) and $N = 128$ (orange). Top inset is a schematic of the simulation geometry. Bottom inset shows an oscillation cycle of the pore. (b) High frequency limit of the gain, η where $\omega \gg 1$, for different values of ϵ_{pm} and F. The points are simulation data for oscillating widths and the lines are extracted from an instantaneous static width approximation. Top inset shows the translocation velocity as a function of the static width. Bottom inset shows the velocity as a function of time during the oscillation cycle.

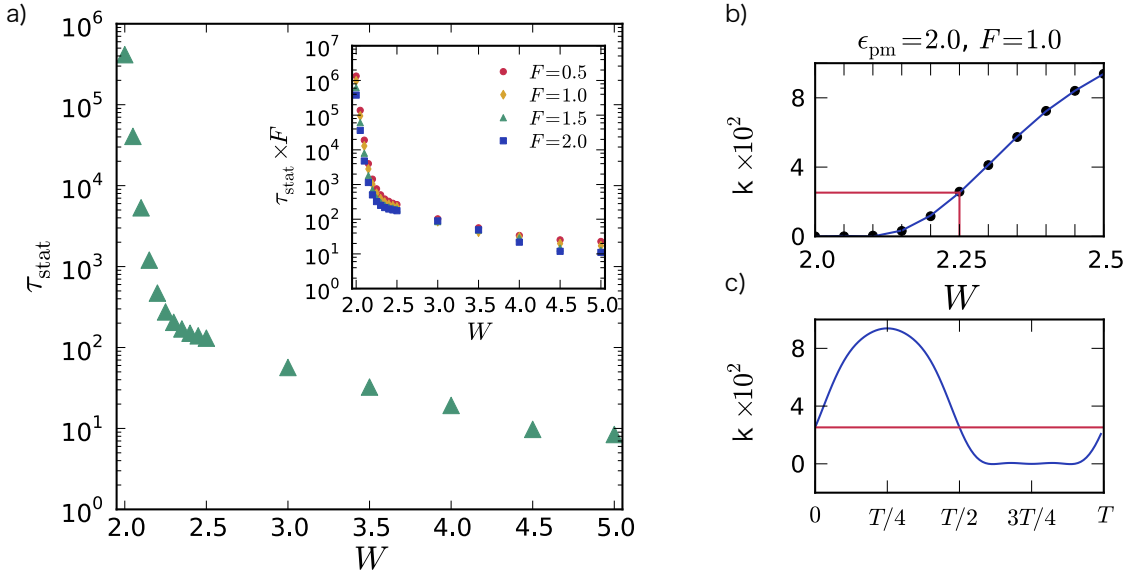

FIGURE 8.6: a) Static translocation time as a function of width. b) Translocation rate as a function of width. c) Translocation rate as a function of time, shown for one period.

Interestingly the value of the gain at the high frequency plateau $\eta_{\tilde{\omega}\gg 1}$ can be different from 1. One would expect $\eta_{\tilde{\omega}\gg 1} \to 1$ if the benefit of an open cycle is balanced by the penalty of the close cycle. However, it is found that at high ϵ and low f the benefit of an open cycle can far outweigh the close cycle, see Figure 8.5. This is due to sampling translocation times across a transition to high confinement, as can be seen from the response of static translocation time to width, see Figure 8.6 a). The average translocation rate $k = N/\tau_{\text{stat}}$ for the widths used in the simulation is shown in Figure 8.6 b). Knowing the time dependence of the width we can approximate time dependent translocation velocity from the static translocation times and see that, indeed, the benefit of the open cycle far exceeds the close cycle under these conditions, see Figure 8.6 c). In summary, the interesting effect of the high frequency limit of the gain is due to the oscillating width sampling the non-linear region of the static translocation time as a function of width, Figure 8.6. If a range of widths that sampled the linear region was used this effect would not be present.

The initial phase, ϕ, is important at low frequencies, however, the gain becomes independent of the phase at high frequency, see Figure 8.7. The low frequency features of the gain can be explained by considering the position of the initial open and close cycles, as was done for the $\phi = 0$ case above. The translocation time distributions show an interesting series of peaks, see Figure 8.8. The standard translocation time distribution becomes modulated with a period matching that of the pore oscillation. Translocation can only complete when the pore is not closed. The number of translocated monomers, N_{trans}, show a series of plateaus in the close periods of oscillation.

8.3.3 Time dependent mobility comparison

We now compare the results of the polymer simulation to the time dependent mobility approximation described in Section 8.2. As expected, this approximation works well for

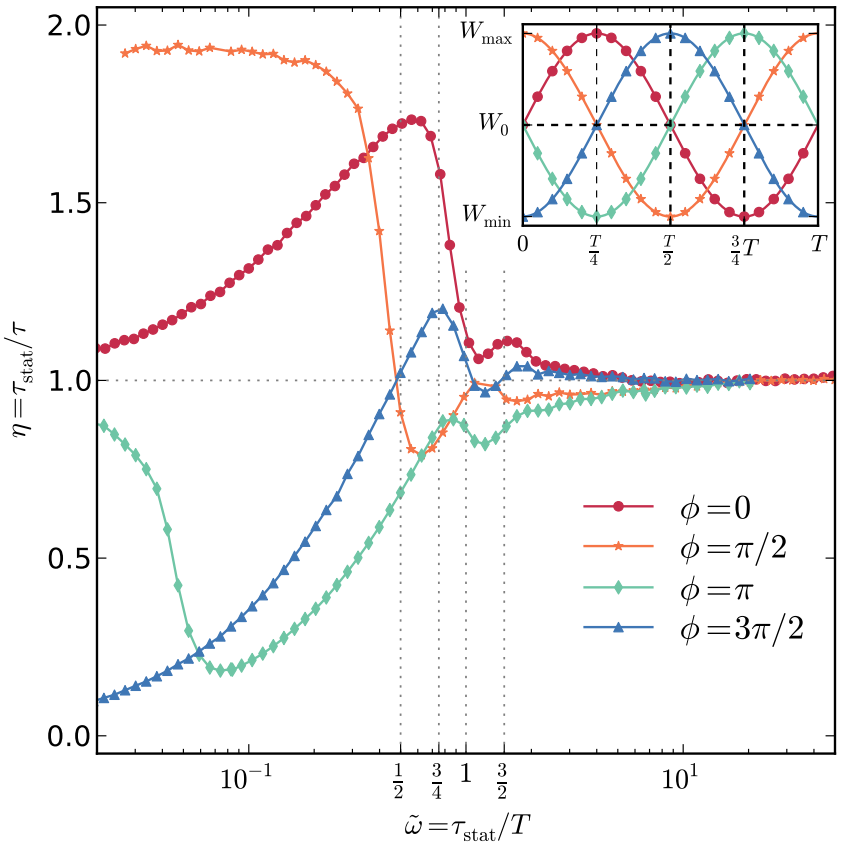

FIGURE 8.7: Frequency response of the gain for differential initial phase, ϕ, shown with the trajectory of the pore width (top right), for $N = 32$, $\epsilon_{\rm pm} = 1.0$ and $F = 1.0$.

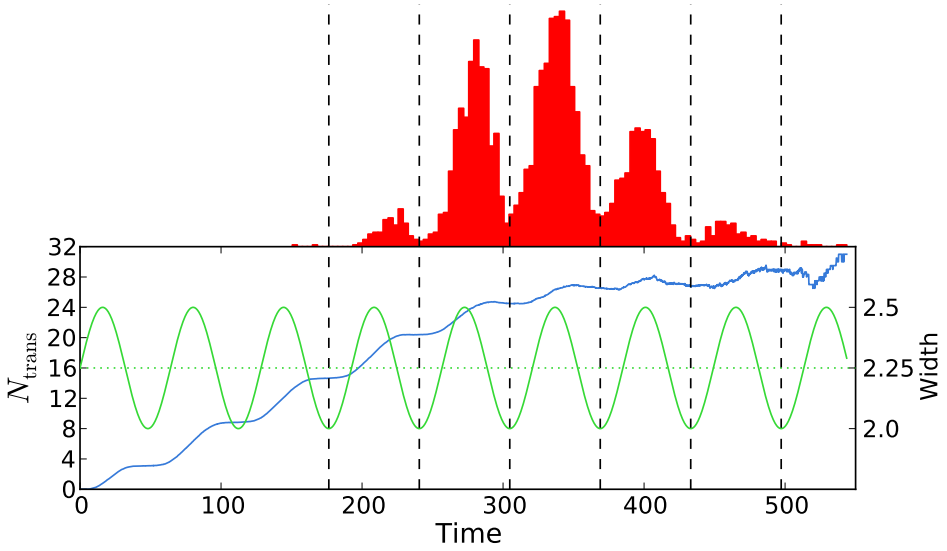

FIGURE 8.8: Translocation time distribution for an oscillating nanopore (top) shown with the average number of translocated monomers (bottom, left axis) and the width of the pore (bottom, right axis).

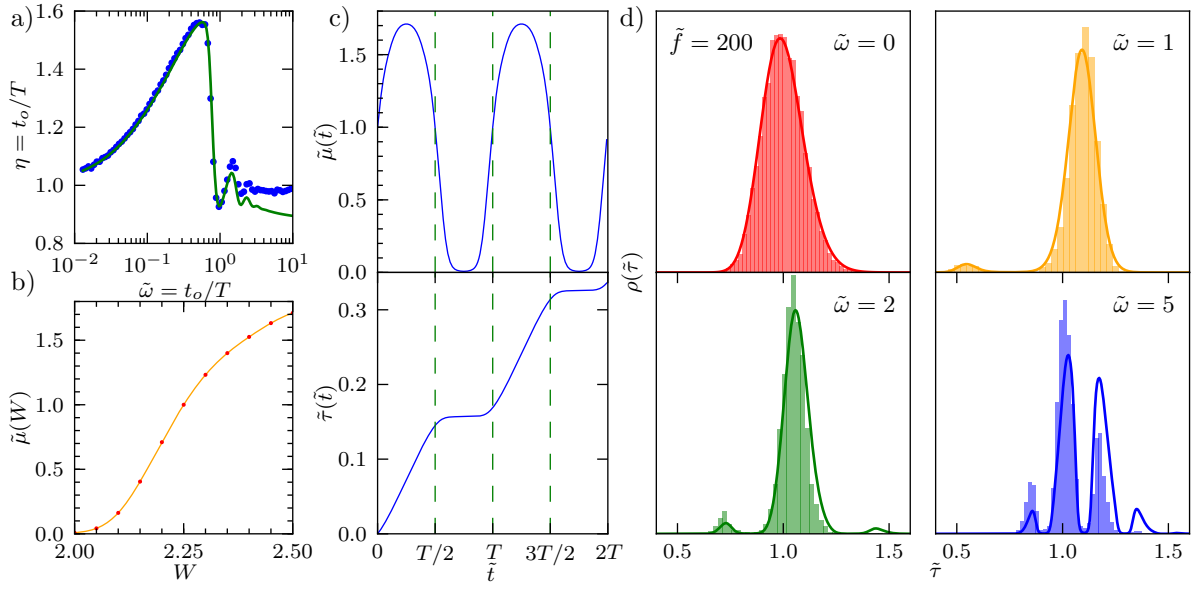

FIGURE 8.9: a) The scaled frequency response for the gain in polymer translocation time from simulations (dots) is reproduced well at low frequencies by the effective single particle description (solid line). However, at higher frequencies the response is only matched qualitatively. This is shown for simulation parameters $N = 128$, $\epsilon = 1$ and $F = 1$. b) The mobility as a function of width for simulation parameters $\epsilon = 1$, $F = 1$ and $N = 128$. c) The mobility and its integral, $\tilde{\tau}$, as a function of time for sinusoidal variation of the width. d) First passage time distributions for different values of the scaled frequency, $\tilde{\omega}$. As the scaled frequency increases the quasi-static approximation breaks down. The polymer has a higher probability of translocating faster as compared to the distribution obtained from the single particle picture.

low frequencies, but fails to quantitatively capture the gain profile at high frequency, see Figure 8.9 a).

We measure the translocation mobility, $\mu = k/F$, using the average translocation rate $k = N/\tau_{\text{stat}}$, obtained from the static translocation time at a fixed width. Using this we construct the function $\mu(W)$ through cubic interpolation. Knowing the time dependent width $W(t) = W_0 + W_A \sin(\omega t)$ we construct the time dependent mobility $\mu(t) = \mu(W(t))$ and its integral $\tau(t)$, see Figure 8.9 b) and c). We then apply (8.22) in order to find the translocation time distribution $\rho(t)$. As we have no estimate for $\tilde{f}$ we measure this by fitting the distribution at $\omega = 0$. The comparison between the time dependent mobility approximation and the simulation results are shown in Figure 8.9 d). The distributions fit well for low frequency, but as the frequency becomes higher the approximation tends

to overestimate the translocation time.

8.4 Conclusions and future outlook

In this chapter we investigated the effect of time dependent mobility on single particle translocation and compared these results to those obtained from polymer translocation simulations through attractive pores.

For deterministic translocation of a single particle we constructed the frequency response of the gain for the two state system. This exhibited clear features as a result of the 'off' period, with a 'ringing' gain ultimately decaying to unity as the dimensionless frequency tends to infinity. Developing this, we formulated the frequency response for any time periodic changes in the mobility. We applied this formalism to a sawtooth ramping mobility and sinusoidal oscillations. We included diffusion in the translocation process and found an exact expression for the gain in the two state problem and numerical solutions to the sinusoidally oscillating mobilities. These results were compared against the deterministic case by taking the limit $\tilde{f} \to \infty$.

We moved on to investigate the more involved problem of polymer translocation through an oscillating pore. The ringing features of the gain could be easily explained with the single particle picture in mind. The gain was found to be dependent on the initial phase at low frequencies, but tended to a single value independent of phase as the frequency was increased. We found that oscillating high affinity pores under weak driving force at moderate to high frequencies could enhance the translocation process. This is an interesting result, as it suggests that selective pores with a high affinity for a particular polymer could speed up their passage time by size fluctuations.

The translocation time distributions were no longer smooth but became partitioned into peaks with the same period as the pore oscillation. In order to capture the form of

these distributions we used the diffusive time dependent mobility approximation developed in the first section. We constructed the average mobility as a function of width from measurement of the static translocation time and found its variation in time from the imposed time dependent width. For a polymer of length $N = 128$, the single particle description overestimates the translocation time from $\tilde{\omega} \sim 5$, suggesting that the time dependent mobility approximation breaks down.

In order to capture the high frequency features it seems necessary to consider the full problem of a tilted periodic fluctuating potential. This would be a challenging problem, but the rewards may lead to novel frequency specific separation techniques.

Bibliography

[1] M. C. Marchetti *et al.*, Soft active matter, *arXiv*, 1207.2929, 2012. (pp. 2, 3)

[2] H. H. Wensink *et al.*, Meso-scale turbulence in living fluids, *Proc. Natl. Acad. Sci. USA*, **109**, 36, 14308–14313, 2012. (p. 2)

[3] V. Narayan, S. Ramaswamy and N. Menon, Long-Lived Giant Number Fluctuations in a Swarming Granular Nematic, *Science*, **317**, 5834, 105–108, 2007. (p. 2)

[4] T. Vicsek and A. Zadeiris, Collective motion, *Phys. Rep.*, **517**, 71–140, 2012. (p. 3)

[5] S. Ramaswamy, The Mechanics and Statistics of Active Matter, *Annu. Rev. Condens. Matt. Phys.*, **1**, 33–345, 2010. (p. 3)

[6] J. Toner and Y. Tu, Long-Range Order in a Two-Dimensional Dynamical XY Model: How Birds Fly Together, *Phys. Rev. Lett.*, **75**, 4326–4329, 1995. (p. 3)

[7] A. Attanasi *et al.*, Superfluid transport of information in turning flocks of starlings, *arXiv*, 1303.7097, 2013. (p. 3)

[8] E. M. Purcell, Life at Low Reynolds Number, *Am. J. Phys.*, **45**, 3–11, 1977. (p. 4)

[9] H. C. Berg, *E. coli in motion*, Springer, 2004. (pp. 4, 41)

[10] R. F. Ismagilov, A. Schwartz, N. Bowden and G. M. Whitesides, Autonomous Movement and Self-Assembly, *Angew. Chem.*, **1137**, 4, 2002. (p. 5)

[11] W. F. Paxton *et al.*, Catalytic Nanomotors: Autonomous Movement of Striped Nanorods, *J. Am. Chem. Soc.*, **126**, 13424–13431, 2004. (p. 5)

[12] J. L. Moran, P. M. Wheat and J. D. Posner, Locomotion of electrocatalytic nanomotors due to reaction induced charge autoelectrophoresis, *Phys. Rev. E*, **8**, 065302(R), 2010. (p. 5)

[13] E. Yariv, Electrokinetic self-propulsion by inhomogenous surface kinetics, *Proc. Roc. Soc. A*, **467**, 1645–1664, 2010. (p. 5)

[14] R. Golestanian, T. B. Liverpool and A. Ajdari, Propulsion of a Molecular Machine by Asymmetric Distribution of Reaction Products, *Phys. Rev. Lett.*, **94**, 220801, 2005. (p. 5)

[15] R. Golestanian, T. B. Liverpool and A. Ajdari, Designing phoretic micro- and nano-swimmers, *New J. Phys.*, **9**, 126, 2007. (pp. 5, 12)

[16] J. R. Howse *et al.*, Self-Motile Colloidal Particles: From Directed Propulsion to Random Walk, *Phys. Rev. Lett.*, **99**, 048102, 2007. (p. 6)

[17] S. Ebbens, R. A. L. Jones, A. J. Ryan and R. Golestanian, Self-assembled autonomous runners and tumblers, *Phys. Rev. E*, **82**, 015304(R), 2010. (p. 6)

[18] H.-R. Jiang, N. Yoshinaga and M. Sano, Active Motion of a Janus Particle by Self-Thermophoresis in a Defocused Laser Beam, *Phys. Rev. Lett.*, **105**, 268302, 2010. (pp. 6, 23)

[19] B. Qian, D. Montiel, A. Bregulla, F. Chichos and H. Yang, Harnessing thermal fluctuations for purposeful activities: the manipulation of single micro-swimmers by adaptive photon nudging, *Chem. Sci.*, **4**, 1420–1429, 2013. (pp. 6, 21)

[20] M. Ibele, T. E. Mallouk and A. Sen, Schooling Behaviour of Light-Powered Autonomous Micromoters in Water, *Angew. Chem. Int. Ed.*, **48**, 3308–3312, 2009. (p. 7)

[21] M. Ibele, P. E. Lammert, V. H. Crespi and A. Sen, Emergent, Collective Oscillations of Self-Mobile Particles and Patterned Surfaces under Redox conditions, *ACS Nano*, **4**, 8, 4845–4851, 2010. (p. 7)

[22] J. Palacci, B. Abecassis, C. C. Bizonne, C. Ybert and L. Bocquet, Colloidal Motility and Pattern Formation under Rectified Diffusiophoresis, *Phys. Rev. Lett.*, **104**, 138302, 2010. (p. 8)

[23] J. Palacci, C. C. Bizonne, C. Ybert and L. Bocquet, Sedimentation and Effective Temperature of Active Colloid Suspensions, *Phys. Rev. Lett.*, **105**, 088304, 2010. (p. 8)

[24] J. Palacci, S. Sacanna, A. O. Steinberg, D. J. Pine and P. M. Chaikin, Living Crystals of Light-Activated Colloidal Surfers, *Science*, **339**, 6122, 936–940, 2013. (p. 8)

[25] J. L. Anderson, Colloid transport by interfacial forces, *Ann. Rev. Fluid Mech.*, **21**, 61–99, 1989. (pp. 11, 12)

[26] R. Piazza and A. Parola, Thermophoresis in colloidal suspensions, *J. Phys.: Condens. Matter*, **20**, 153102, 2008. (pp. 12, 22, 23)

[27] A. Wurger, Thermal non-equilibrium transport in colloids, *Rep. Prog. Phys*, **73**, 126601, 2010. (pp. 12, 24)

[28] J. L. Anderson and D. C. Prieve, Diffusiophoesis Caused by Gradients of Strongly Adsorbing Solutes, *Langmuir*, **7**, 403–406, 1991. (p. 13)

[29] F. Julicher and J. Prost, Generic theory of colloidal transport, *Euro. Phys. J. E*, **29**, 1, 27–36, 2009. (pp. 14, 24)

[30] B. Sabass and U. Seifert, Dynamics and efficiency of a self-propelled, diffusiophoretic swimmer, *J. Chem. Phys.*, **136**, 6, 064508, 2012. (p. 14)

[31] M. N. Popescu, S. Dietrich and G. Oshanin, Confinement effects on diffusiophoretic self-propellers, *J. Chem. Phys.*, **130**, 19, 194702, 2009. (p. 14)

[32] B. Sabass and U. Seifert, Nonlinear, electrocatalytic swimming in the presence of salt, *J. Chem. Phys.*, **136**, 21, 214507, 2012. (p. 14)

[33] S. N. Rasuli and R. Golestanian, Soret Motion of a Charged Spherical Colloid, *Phys. Rev. Lett.*, **101**, 108301, 2008. (pp. 14, 24)

[34] J. D. Jackson, *Classical Electrodynamics, third edition*, John Wiley and Sons, New York, USA, 1998. (pp. 14, 27)

[35] M. Doi and S. Edwards, *Polymer Dynamics*, Clarendon Press, Oxford, 1986. (pp. 19, 83)

[36] M. Raible and A. Engel, Langevin equation for the rotation of a magnetic particle, *Appl. Organometal. Chem.*, **18**, 536–541, 2004. (p. 21)

[37] C. F. Bohren and D. R. Huffman, *Absorption and Scattering of Light by Small Particles*, John Wiley & Sons, New york, USA, 1983. (p. 25)

[38] R. A. L. Jones, *Soft Condensed Matter*, Oxford University Press, Oxford, 2002. (p. 35)

[39] J. Tailleur and M. E. Cates, Statistical Mechanics of Interacting Run-and-Tumble Bacteria, *Phys. Rev. Lett.*, **100**, 218103, 2008. (p. 36)

[40] M. E. Cates and J. Tailleur, When are active Brownian particles and run-and-tumble particles equivalent? Consequences for motility-induced phase separation, *Europhys. Lett.*, **101**, 20010, 2013. (pp. 36, 39)

[41] G. Lakatos, J. O'Brien and T. Chou, Hydrodynamic mean-field solutions of 1D exclusion processes with spatially varying hopping rates, *J. Phys. A: Math. Gen.*, **39**, 2253–2264, 2006. (p. 37)

[42] R. Golestanian, Collective Behavior of Thermally Active Colloids, *Phys. Rev. Let..*, **108**, 038303, 2012. (pp. 39, 41)

[43] E. F. Keller and L. A. Segal, Model for chemotaxis, *J. Theor. Biol.*, **26**, 399–415, 1970. (p. 41)

[44] P.-H. Chavanis and C. Sire, Estimate of blow-up and relaxation time for self-gravitating Brownian particles and bacterial populations, *Phys. Rev. E.*, **70**, 026115, 2004. (p. 41)

[45] A. Turing, The Chemical Basis of Morphogensis, *Phil. Trans.*, **237**, 641, 1952. (p. 42)

[46] M. P. Brenner, L. S. Levitov and E. O. Budrene, Physical Mechanisms for Chemotactic Pattern Formation by Bacteria, *Biophys. J.*, **74**, 1677–1693, 1998. (p. 42)

[47] M. E. Cates, D. Marenduzzo, I. Pagonabarraga and J. Tailleur, Arrested phase separation in reproducing bacteria creates a generic route to pattern formation, *Proc. Natl. Acad. Sci. USA*, **107**, 206, 11715–11720, 2010. (p. 42)

[48] Y. Fily and M. C. Marchetti, Athermal Phase Separation of Self-Propelled Particles with No Alignment, *Phys. Rev. Lett.*, **108**, 235702, 2012. (p. 42)

[49] B. H. Kim, J. Y. Kim and S. O. Kim, Directed self-assembly of block copolymers for universal nanopatterning, *Soft Matter*, **9**, 2780–2786, 2013. (p. 42)

[50] J. N. Wilking *et al.*, Liquid transport facilitated by channels in Bacillus subtilis biofilms, *Proc. Natl. Acad. Sci. USA*, **110**, 3, 848–852, 2013. (p. 42)

[51] M. P. Brenner, P. Constantin, L. P. Kadanoff, A. Schenkel and S. C. Venkataramani, Diffusion, attraction and collapse, *Nonlinearity*, **12**, 1071–1098, 1999. (p. 42)

[52] S. I. Dejak, D. Egli, P. M. Lushnikov and I. M. Sigal, On blowup dynamics in the Keller-Segal model of chemotaxis, *arXiv*, 1304.1583, 2013. (p. 42)

[53] S. V. Patankar, *Numerical Heat Transfer and Fluid Flow*, McGraw-Hill, New York, 1980. (p. 43)

[54] A. Kurganov and E. Tadmor, New High-Resolution Central Schemes for Nonlinear Conservation Laws and Convection-Diffusion Equations, *J. Comp. Phys.*, **160**, 2000. (p. 43)

[55] J. Y. Murthy and S. R. Mathur, *Numerical Methods in Heat, Mass, and Momentum Transfer*, 2012 (Accessed April 18, 2013), https://engineering.purdue.edu/ME608/webpage/main.pdf. (p. 43)

[56] R. J. LeVeque, *Finite Volume Methods for Hyperbolic Problems*, Cambridge University Press, Cambridge, 2002. (pp. 43, 44)

[57] W. H. Press, S. A. Teukolsky, W. T. Vetterling and B. P. Flannery, *Numerical recipes in C+: the art of scientific computing*, Cambridge University Press; Cambridge, 2009. (pp. 43, 49)

[58] J. N. Israelachvili, *Intermolecular and surface forces: revised third edition*, Academic press, Massachusetts, USA, 2011. (p. 47)

[59] D. Rings, R. Schachoff, M. Selmke, F. Cichosa and K. Kroy, Hot Brownian Motion, *Phys. Rev. Lett.*, **105**, 090604, 2010. (p. 60)

[60] V. Rokhlin and M. Tygert, Fast Algorithms for Spherical Harmonics Expansions, *SIAM J. Sci. Comput.*, **27**, 6, 1903–1928, 2006. (p. 63)

[61] M. J. Mohlenkamp, *A User's Guide to Spherical Harmonics*, 2011 (Accessed April 15, 2013), http://www.ohio.edu/people/mohlenka/research/uguide.pdf. (p. 63)

[62] J. J. Kasianowicz, E. Brandin, D. Branton and D. Deamer, Characterization of individual polynucleotide molecules using a membrane, *Proc. Natl. Acad. Sci. USA*, **93**, 15770, 1996. (pp. 78, 79, 81)

[63] D. Branton *et al.*, The potential and challenges of nanopore sequencing, *Nature Biotech.*, **26**, 1146, 2008. (p. 78)

[64] Oxford Nanopore Technologies, press release, 2012. (p. 78)

[65] W. H. Coulter, Means for counting particles suspended in a fluid, U.S. Patent, 112, 819, 1949. (p. 79)

[66] A. Hall *et al.*, Hybrid pore formation by directed insertion of alpha-hemolysin into solid-state nanopores, *Nature Nanotech.*, **5**, 874–877, 2010. (pp. 80, 82)

[67] S. E. Henrickson, M. Misakian, B. Robertson and J. J. Kasianowics, Driven DNA Transport into an Asymmetric Nanometer-Scale Pore, *Phys. Rev. Lett.*, **85**, 14, 3057–3060, 2000. (p. 80)

[68] A. Meler, L. Nivon and D. Branton, Voltage-Driven DNA Translocation through a Nanopore, *Phys. Rev. Lett.*, **86**, 15, 2001. (p. 80)

[69] A. Meler and D. Branton, Single molecule measurements of DNA transport through a nanopore, *Electrophoresis*, **23**, 2583–2591, 2002. (p. 81)

[70] D. Deamer and D. Branton, Characterization of Nucleic Acids by Nanopore Analysis, *Acc. Chem. Res*, **35**, 817–825, 2002. (p. 81)

[71] D. Stoddart *et al.*, Nucleobase Recognition in ssDNA at the Central Constriction of the alpha-Hemolysin Pore, *Nano Lett.*, **10**, 3633, 2010. (p. 81)

[72] J. Clarke *et al.*, Continuous base identification for single-molecule nanopore DNA sequencing, *Nature Nanotech.*, **4**, 265–270, 2009. (p. 81)

[73] C. Dekker, Solid-state nanopores, *Nature Nanotech.*, **2**, 209–215, 2007. (p. 81)

[74] J. Li, Ion-beam sculpting at nanometre length scales, *Nature*, **412**, 166–169, 2001. (p. 81)

[75] A. J. Storm, J. H. Chen, X. S. Ling, H. W. Zandbergen and C. Dekker, Electron-beam-induced deformations of SiO2 nanostructures, *J. Appl. Phys.*, **98**, 014307, 2005. (pp. 82, 85)

[76] N. A. W. Bell *et al.*, DNA Oragmi Nanopores, *Nano Lett.*, **12**, 512–517, 2012. (p. 82)

[77] P. de Gennes, *Scaling concepts in polymer physics*, Cornell University Press, Ithaca; London, 1979. (pp. 83, 84)

[78] T. Sakaue, Sucking genes into pores: Insight into driven translocation, *Phys. Rev. E*, **81**, 041808, 2010. (pp. 84, 88, 89, 89)

[79] Y. Kantor and M. Kardar, Anomalous dynamics of forced translocation, *Phy. Rev. E*, **69**, 021806, 2004. (p. 85)

[80] W. Sung and P. J. Park, Polymer Translocation through a Pore in a Membrane, *Phys. Rev. Lett.*, **77**, 4, 1996. (p. 85)

[81] M. Muthukumar, *Polymer Translocation*, CRC Press, Florida, 2011. (p. 85)

[82] D. Lubensky and D. Nelson, Driven polymer translocation through a nanopore, *Biophys. J.*, **77**, 1824–1838, 1996. (p. 86)

[83] P. Reimann, A. Meyer and S. Getfert, On the Lubensky-Nelson Model of Polymer Translocation through Nanopores, *Biophys. J.*, **103**, 889–897, 2012. (p. 87)

[84] A. Y. Grosberg, S. Nechaev, M. Tamm and O. Vasilyev, How long does it take to pull an ideal polymer into a small hole?, *Phys. Rev. Lett.*, **98**, 228105, 2006. (p. 88)

[85] O. Hallatschek, E. Frey and K. Kroy, Propagation and relaxation of tension in stiff polymers, *Phy. Rev. Lett.*, **94**, 077804, 2005. (p. 88)

[86] T. Sakaue, Nonequilibrium dynamics of polymer translocation and straightening, *Phy. Rev. E*, **76**, 021803, 2007. (p. 88)

[87] T. Saito and T. Sakaue, Dynamical diagram and scaling in polymer driven translocation, *Eur. Phys. J. E*, **34**, 135, 2011.

[88] T. Saito and T. Sakaue, Process time distribution of driven polymer transport, *Phys. Rev. E*, **85**, 061803, 2012. (p. 88)

[89] S. Chern, A. E. Cardenas and R. D. Coalson, Three-dimensional dynamic Monte Carlo simulations of driven polymer transport through a hole in a wall, *J. Chem. Phys.*, **115**, 16, 2001. (p. 89)

[90] H. C. Loebl, R. Randel, S. P. Goodwin and C. C. Matthai, Simulations studies of polymer translocation through a channel, *Phys. Rev. E*, **67**, 041913, 2003. (p. 89)

[91] K. Luo, I. Huopaniemi, T. Ala-Nissila and S. Ying, Polymer translocation through a nanopore under an applied external field, *J. Chem. Phys.*, **124**, 114704, 2006. (p. 89)

[92] P. Tian and G. D. Smith, Translocation of a polymer chain across a nanopore: A Brownian dynamics simulation study, *Phys. Rev. E*, **67**, 041913, 2003. (p. 89)

[93] I. Huopaniemi, K. Luo, T. Ala-Nissila and S. Ying, Langevin dynamics simulations of polymer translocation through nanopores, *J. Chem. Phys.*, **125**, 124901, 2006.

[94] K. Luo, T. Ala-Nissila, S. C. Yeng and A. Bhattacharya, Influence of Polymer-Pore Interactions on Translocation, *Phys. Rev. Lett.*, **99**, 148102, 2007.

[95] K. Luo, T. Ala-Nissila, S. C. Ying and A. Bhattacharya, Influence of Polymer-Pore Interactions on Translocation, *Phys. Rev. E*, **78**, 061918, 2008. (p. 93)

[96] K. Luo, T. Ala-Nissila, S. C. Ying and R. Metzler, Driven polymer translocation through nanopores: Slow-vs.-fast dynamics, *Europhys. Lett.*, **88**, 68006, 2009. (p. 89, 89)

[97] M. Muthukumar and C. Y. Kong, Simulation of polymer trnaslocation through protein channels, *Proc. Natl. Acad. Sci. USA*, **103**, 14, 2006. (p. 89, 89)

[98] A. Aksimentiev and K. Schulten, Imaging alpha-Hemolysin with Molecular Dynamics: Ionic Conductance, Osmotic Permeability, and the Electrostatic Potential Map, *Biophys. J.*, **88**, 3745–3761, 2005. (p. 89, 89)

[99] R. Zwanzig, *Nonequilibrium statistical mechanics*, Oxford University Press, Oxford, 2001. (p. 92)

[100] M. P. Allen and D. J. Tildesley, *Computer Simulation of Liquids*, Oxford University Press, Oxford, 1989. (p. 92)

[101] A. F. Sauer-Budge, J. A. Nyamwanda, D. K. Lubensky and D. Branton, Unzipping kinetics of double-stranded DNA in a nanopore, *Phys. Rev. Lett.*, **90**, 2381011, 2003. (p. 93)

[102] C. Pozrikidis, *Boundary Integral and Singularity Methods for Linearized Viscous Flow*, Cambridge University Press, Cambridge, 1992. (p. 95)

[103] D. K. Ermak and J. A. McCammon, Brownian dynamics with hydrodynamic interactions, *J. Chem. Phys.*, **69**, 1352, 1978. (p. 95)

[104] A. T. Chwang and T. Y. Wu, Hydrodynamics of low-Reynolds-number flow. Part II. Singularity method for Stokes flows, *J. Fluid Mech.*, **67**, 4, 1975. (p. 95)

[105] R. M. Jendrejack, D. C. Schwartz, M. D. Graham and J. J. de Pablo, Effect of confinement on DNA dynamics in microfluidic devices, *J. Chem. Phys.*, **119**, 2, 1165–1173, 2003. (p. 95)

[106] J. P. Hernandez-Ortiz, J. J. de Pablo and M. D. Graham, N log N method for hydrodynamic interactions of confined polymer systems: Brownian dynamics, *J. Chem. Phys.*, **125**, 16, 164906, 2006.

[107] J. P. Hernandez-Ortiz, J. J. de Pablo and M. D. Graham, Fast Computation of Many-Particle Hydrodynamic and Electrostatic Interactions in a Confined Geometry, *Phys. Rev. Lett.*, **98**, 140602, 2007. (p. 95)

[108] A. Meler, L. Nivon, E. Brandin, J. Golovchenko and D. Branton, Rapid nanopore discrimination between single oligonucleotide molecules, *Proc. Natl. Acad. Sci. USA*, **97**, 1079, 2000. (p. 105)

[109] K. Luo, T. Ala-Nissila, S. C. Ying and A. Bhattacharya, Sequence dependence of DNA translocation through a nanopore, *Phys. Rev. Lett.*, **100**, 058101, 2008. (p. 105)

[110] Y. Roongthumskul, R. Shlomovitz, R. Bruinsma and D. Bozovic, Phase Slips in Oscillatory Hair Bundles, *Phys. Rev. Lett.*, **110**, 2013. (p. 114)

[111] J. A. Cohen, A. Chaudhuri and R. Golestanian, Active Polymer Translocation through Flickering Pores, *Phys. Rev. Lett.*, **107**, 238102, 2011. (p. 115)

[112] J. A. Cohen, A. Chaudhuri and R. Golestanian, Translocation through environments with time dependent mobility, *J. Chem. Phys*, **137**, 204911, 2012. (p. 115)

[113] P. Fanzio *et al.*, Modulating DNA Translocation by a Controlled Deformation of a PDMS Nanochannel Device, *Sci. Rep.*, **2**, 791, 2012. (p. 116)

[114] P. Reimann, Brownian motors: noisy transport far from equilibrium, *Phys. Rep.*, **361**, 2-4, 57–265, 2002. (p. 118)

[115] A. Molini, P. Talkner, G. Katul and A. Porporato, First passage time statistics of Brownian motion with purely time dependent drift and diffusion, *Physica A*, **390**, 11, 1841–1852, 2011. (p. 125)

[116] Z. Schuss, *Theory and Applications of Stochastic Processes*, Springer, New York; Dordrecht; Heidelberg; London, 2010. (p. 125)